AQUEOUS ELECTRODE PROCESSING FOR HIGH ENERGY

DENSITY LITHIUM-ION BATTERIES

A Thesis

by

KELSEY MARIE ROLLAG

Submitted to the Office of Graduate and Professional Studies of
Texas A&M University
in partial fulfillment of the requirements for the degree of

MASTER OF SCIENCE

Chair of Committee,	Partha P. Mukherjee
Committee Members,	Sarbajit Banerjee
	Hong Liang
Head of Department	Andreas A. Polycarpou

May 2017

Major Subject: Mechanical Engineering

ABSTRACT

Widespread use of electric vehicles is hinged on the advancement of energy storage technologies such as lithium-ion batteries. Current research and development endeavors in energy storage for electric vehicles are focused on increasing the energy density of a battery while simultaneously reducing manufacturing costs. Energy density can be improved by minimizing the number of inactive components in a cell with the implementation of thicker electrodes. Furthermore, cost can be significantly reduced with aqueous electrode processing. Unlike conventional electrode processing which uses the expensive and highly toxic organic solvent, N-methyl-2-pyrrolidone (NMP), aqueous processing employs deionized water. Aqueous processing of thick electrodes offers the opportunity to produce relatively inexpensive, high energy density lithium-ion batteries. However, thick aqueous processed cathodes have been found to crack as they dry.

In an effort to avoid cracking and enable aqueous processing for thick $LiNi_{1-y-z}Mn_yCo_zO_2$ (NMC) cathodes, the influence of two processing parameters on cracking were investigated in this work. They include solvent surface tension and electrode drying temperature. Small weight percentages of isopropanol (IPA) mixed in water were tested as novel composite solvents in aqueous processing. It was found that the addition of 20 wt.% IPA produced an aqueous solvent with a surface tension low enough to avoid any cracking in thick cathodes. When paired with a graphite anode in a single unit pouch cell, thick cathodes processed with 20 wt.% IPA as solvent performed comparably to an electrode processed with the conventional solvent, NMP. Separate experiments with electrode drying temperatures ranging from 20 °C to 70 °C revealed cracking worsens at elevated drying temperatures. Images of electrode surfaces were processed to quantify crack dimensions and crack intensity factor (CIF). Average crack length and width increased with drying temperature and electrode thickness. The CIF also increased with drying temperature and electrode thickness, the most dramatic increase being from 0.68% for thick electrodes dried at 20 °C to 15.8% when thick electrodes were dried at 70 °C.

ACKNOWLEDGEMENTS

CONTRIBUTORS AND FUNDING SOURCES

NOMENCLATURE

P_{cap}	Capillary pressure
γ	Liquid-vapor surface tension of solvent
θ	Liquid-solid contact angle
r_p	Pore radius
ϕ	Particle volume fraction
ρ_s	Density of solid material
S	Total surface area of particles
G_c	Elastic energy recovered by crack propagation
W	Reversible work required to create two new surfaces of a crack
σ_c	Critical stress for cracking
R	Particle radius
h	Film thickness
G	Shear modulus of particles
M	Coordination number
ϕ_{rcp}	Particle volume fraction at random close packing
h_{max}	Critical thickness/maximum crack-free thickness
ε_{max}	Maximum compressive strain
P_{max}	Maximum capillary pressure

σ_Y	Yield stress for plastic fracture
σ_o	Stress at maximum capillary pressure
γ_p	Surface energy of solid material
F_{max}	Maximum attractive interparticle force
U_p	Irreversible plastic fracture energy loss
x_1	Mole fraction of water
x_2	Mole fraction of isopropanol
γ_1	Liquid-vapor surface tension of water
γ_2	Liquid-vapor surface tension of isopropanol
E	Evaporation rate
U	Sedimentation velocity
Pe	Peclet number
D_o	Stokes-Einstein diffusion coefficient
μ	Fluid viscosity
T	Temperature
k	Boltzmann constant
y	Crack spacing
X	Hydrodynamic length scale
h_f	Final dry film thickness

m_w	Mass of water
t	Time
B	Slope of linear curve fitting
ρ_w	Density of water
A	Surface area of electrode coating
Δt_1	Duration of constant rate phase of drying
τ	Exponential time constant

TABLE OF CONTENTS

LIST OF FIGURES

LIST OF TABLES

CHAPTER I

INTRODUCTION

I.1. Introduction to Lithium-Ion Batteries

Energy storage has become an integral part of life with ubiquitous personal electronics such as laptops and cell phones. Batteries are the most promising form of energy storage as they can accommodate many applications ranging from personal electronic devices to grid connection. Growing concerns for the environmental consequences of fossil fuels has the global community turning to renewable energy sources such as wind and solar power. But without energy storage, objectives to fully integrate renewable energy sources into the global power market will never be realized, because renewable sources are unpredictable and intermittent. Energy storage provides the capability to regulate renewable energy supply. Furthermore, by including personal energy storage on private and commercial properties, batteries can alleviate stress on the grid during peak hours.

Of late, the primary focus of the energy storage industry is hybrid electric vehicles (HEV's) and full electric vehicles (EV's). Motivated by global efforts to curb the effects of global warming, the automotive industry is on the brink of a major shift towards cleaner transportation options. However, researchers must develop batteries capable of driving a vehicle without sacrificing the power and range provided by combustion engines. Electric vehicles require fast, high current charging batteries that can operate effectively in conjunction with regenerative braking. Batteries for electric vehicles must also have a high energy density capable of supplying enough power to rapidly accelerate and sustain vehicle motion for a practical number of miles.

In 2012 the United States' Department of Energy (DOE) Office of Vehicle Technology set goals for the battery industry to achieve by 2022 to ensure battery technology is well equipped to meet the automotive industry's demands. [1] In FY 2016, the DOE invested $103 million in research and development of advanced battery systems to assist

researchers in meeting these goals. As a result of the DOE's eager investments, the energy density of an EV battery has doubled, while cost has been reduced by 70%. [2] The ultimate objective is to increase the presence of electric vehicles on the roads by making them as practical and affordable for every day Americans as gasoline powered vehicles. [1] By transitioning to HEV's and EV's, the DOE claims US dependence on foreign oil would decrease 30-60%, and greenhouse gas emissions could be reduced by 30-45%. [3]

Table 1: Summary of battery systems R&D progress and goals set by the US DOE to enable wide-spread use of electric vehicle technologies. The table was reproduced from a 2016 DOE presentation summarizing their battery R&D program. [4]

Goals	2012	Current	2022
Electric Range (miles)		✓	200
Discharge Pulse Power, 10 sec (kW)		✓	120
Regenerative Pulse Power, 10 sec (kW)		✓	40
Recharge Rate (kW)		✓	1.2
Calendar Life (yrs)	tbd	tbd	15
Cycle Life (deep cycles)	200	500-600	1,000
System Weight (kg)	500	200-280	190
System Volume (L)	200	90-140	90
Production Cost at 100,000 units/year	$600/kWh	<$268/kWh	$125/kWh

Research and development in energy storage for electric vehicles is focused on lithium-ion batteries (LIBs). [5] Unlike other traditional battery systems such as Ni-MH and Pb-Acid, LIBs have the ability to meet the power and energy demands of a vehicle. The high energy density of a LIB makes them an attractive choice where weight and volume are an area of concern. Furthermore, LIBs have a long cycle life and a very low self-discharge

rate. The major drawback of LIBs is their cost, hence the DOE's earnest initiative to reduce the cost of LIBs to make electric vehicle technologies more affordable.

Lithium-ion batteries were not a showcase in the energy storage industry until 1991 when Sony introduced the first rechargeable LIB to the market. [6] Rather, Pb-acid and Ni-MH batteries were more common. In fact, Pb-acid still dominates 40-45% of the battery market. They are commonly used as starting, lighting, and ignition batteries in vehicles. A Pb-acid battery has excellent efficiency but relatively low energy density. In contrast, Ni-MH batteries have a high energy density and good capacity, but low efficiencies. Before LIBs, Ni-MH batteries were common in HEV's such as the Toyota Prius. Their good cycle life and rapid charge/discharge capabilities made them a satisfactory choice for HEV's. But Ni-MH batteries are expensive and quickly self-discharge. For all of these reasons and more, the introduction of LIBs was a welcomed alternative to other battery technologies that proved to be an unworthy investment for future development of an all-electric vehicle. [7] Table 2 presents a direct comparison of each battery system's most important features.

Table 2: Comparison of the three most common battery systems. The large energy density, high efficiencies, and long cycle life of an LIB make it the most promising battery system. Information was originally presented in a textbook written by Rahn and Wang. [7]

	Pb-Acid	Ni-MH	Li-ion
Theoretical Cell Voltage	1.93	1.35	4.1
Theoretical Specific Energy (Wh/kg)	166	240	410
Practical Specific Energy (Wh/kg)	35	75	150
Energy density (Wh/L)	70	240	400
Energy Efficiency	0.65-0.70	0.55-0.65	~0.8
Power Density (W/L)	450	>300	>800
Cycle Life (# of cycles, DOD)	200, 100%	500, 80%	3000, 100%

In general, a battery is a closed electrochemical system that converts chemical energy into electrical energy. The main components of any battery are a positive electrode (cathode), a negative electrode (anode), and electrolyte. Both the positive and negative electrodes are composed of an electrochemically active material. In a LIB the active material in the cathode is responsible for supplying the lithium ions. [5] Redox reactions occurring in each electrode produce lithium ions and electrons ($Li = Li^+ + e^-$). In the anode, these reactions take place at a lower potential than those in the cathode, hence the terms negative and positive electrodes. [8] Most electrochemically active materials are not electronic conductors, thus a conductive additive (carbon black) is added to each electrode to improve performance. [9] A polymeric binder holds all of the electrode materials together, and binds the electrode to an electronically conductive current collector. Aluminum and copper foil serve as the current collectors of the positive and negative electrode, respectively. [10] An image of the cross section of an LIB is shown in Figure 1.
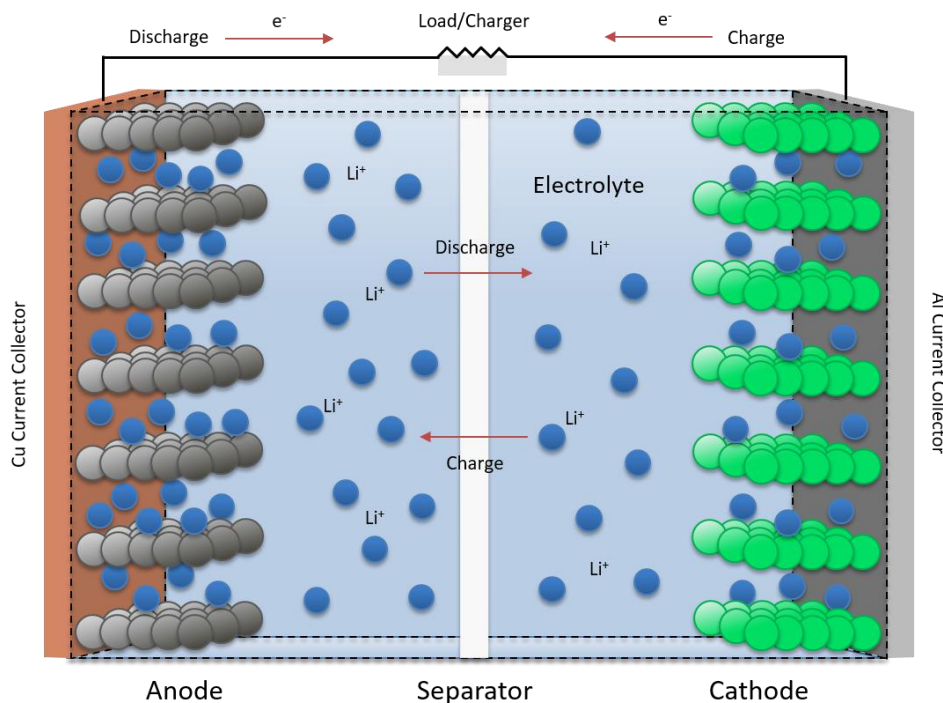
Figure 1: Cross sectional diagram of a Lithium-ion battery, courtesy of ETSL.

Current collectors provide a low resistance path for electrons produced by the electrochemical reaction. These electrons flow through the electrode to the current collector where they are directed through an external circuit to provide power to whatever load is connected to the battery. The lithium ions, on the other hand, diffuse and migrate through the ionically conductive, electronically insulating electrolyte to the opposite electrode. The electrolyte floods the entire cell. It consists of lithium salts dissolved in an organic solvent. [11] A microporous polymeric membrane is positioned between the electrodes to prevent an electrical short circuit. This separator is electronically insulating but ionically conductive so as not to prevent the diffusion of lithium ions between electrodes.

A battery's ability to convert chemical energy to electrical energy is made entirely possible by the fact that electrodes are both ionically and electronically conductive. Therefore, electrochemical reactions occur only at sites where active material, conductive additive, and electrolyte are all in contact. To expose more active material and conductive additive to the electrolyte, electrodes are complex, porous structures. Typical electrodes have ~30% porosity. [8] A larger surface area of electrode/electrolyte interface translates to more electrochemical reaction sites.

In rechargeable batteries, the electrochemical reactions that occur at each electrode are reversible, typically over thousands of cycles. Intercalation reactions occurring in a LIB ensure reversible operation of the battery. During charging/discharging intercalation reactions insert/extract lithium ions from the ordered structure of the active material without changing the host structure. Typically, the volume change between full insertion and extraction of lithium ions is less than 10%. [5] Minimum volume change is critical to maintaining the structural integrity of the electrode.

A lithium-ion battery is assembled in the discharged state, meaning the lithium ions initially occupy sites in the cathode. Upon charging, an oxidation reaction at the cathode extracts lithium ions from the host structure. [12] The lithium ions solvate into the electrolyte and diffuse/migrate to the anode. The potential difference between electrodes

drives lithium ion migration by organizing the anions present in the electrolyte. [7] Meanwhile, electrons move from the cathode to the anode through an external circuit. At the anode, lithium ions intercalate into the anode host structure via a reduction reaction. Electric energy is thus stored as chemical energy by the fact that the chemical potential of lithium is much higher in the anode than the cathode. [12] The entire process is reversed upon discharging when a load is included in the external circuit. An oxidation reaction in the anode releases the electrochemical energy in the form of electric energy as lithium ions are extracted from the anode host structure. [12] The rate at which electrons and lithium ions are forced to travel between electrodes strongly dictates the cell's capacity and cycle life. [13, 14] A slower charge/discharge rate gives lithium ions ample time to diffuse through the pores of the electrode, resulting in a capacity much closer to the theoretical capacity of the cell. [7]

Active materials in the cathode and anode are intercalation compounds capable of hosting the Li-ions during charge/discharge cycling. The active material in a LIB anode is typically graphite. [11] However, new anode materials such as lithium metal alloys including lithium titanate ($Li_4Ti_5O_{12}$) [15, 16], metal based alloys such as SnO_2 [17-22] and carbon composites like silicon/carbon [23-28] are the subject of much research and development. As the source of lithium ions in the battery, the active material in the positive electrode is the limiting factor in the energy capabilities of a battery. [12] Therefore, researchers are continually seeking next-generation cathode materials that push the boundaries of current LIB performance. Common cathode materials found in commercial LIBs include $LiCoO_2$ (LCO), $LiNiO_2$ (LNO), $LiMn_2O_4$ (LMO), and $LiFeO_4$ (LFP). [29]

LCO was the cathode material in the first LIB commercialized by Sony in 1991. [6] It has a high theoretical capacity (274 mAh/g), but its practical capacity is only 120-130 mAh/g as LCO's layered crystalline structure becomes unstable when more than half of the lithium is removed during charging. [12, 30, 31] Moreover, cobalt is a very expensive and environmentally toxic metal. [12] The cost of cobalt limits LCO cathodes to small scale cells such as those used in computers and cell phones. [31] Nonetheless, LCO remains the most common cathode active material in commercial LIBs. [10]

In an effort to achieve high capacities and avoid the cost of cobalt, LNO was proposed as a cathode active material. LNO has the best capacity (180-200 mAh/g) and power of all four common materials but the instability of its layered crystalline structure shortens the life of the cell. [29, 30] Furthermore, when fully delithiated (in charged state) LNO cathodes have poor thermal stability, making LNO as a replacement for LCO in commercial batteries impractical. [10] Alternatively, LMO was proposed as a much more safe, environmentally friendly, and low cost cathode material. [9, 10] The spinel crystal structure of LMO is very stable during cycling. In addition, LMO in the fully charged state (lithium depleted) has little to no excess lithium ions. As a result, there is little risk of excess lithium ions forming detrimental lithium metal dendrites on the anode material during overcharge. However, at temperatures above ambient, divalent manganese ions form and dissolve into the electrolyte. The manganese ions then diffuse to the anode where they reduce to manganese metal, using up valuable lithium in the process. [9, 29, 31]

LFP has an olivine crystal structure, and is also currently the cheapest, most environmentally benign cathode material. Its high thermal decomposition temperature and low energy release make it a safer option when compared to other cathode materials. [10, 29] LFP has a high theoretical capacity of ~170 mAh/g, and remains very stable during cycling, resulting in low capacity fade. [10, 31] Moreover, the low electrochemical potential of LFP relative to other cathode materials makes it more stable in the electrolyte. [29] However, LFP has low electronic conductivity at room temperature, meaning its theoretical capacity can only be obtained at high temperatures or very low current density. [32] Researchers have improved the electrochemical performance of LFP by applying a carbon coating to LFP particles to improve their electronic conductivity. [33] A thin carbon coating effectively provides a path for electrons without inhibiting the transport of lithium ions. [9]

Although LFP is a primary intercalation compound used as active material in cathodes of many commercial batteries, its low density results in a low volumetric energy density unsuitable for electric vehicle applications. [10] Accordingly, recent efforts in LIB research and development for electric vehicles is focused on $LiNi_{1-y-z}Mn_yCo_zO$ (NMC).

[29] Liu et al. were the first to introduce NMC as a potential cathode material for LIBs in 1999. [34] NMC is a combination of the other common cathode materials, eliciting each material's best properties such as the capacity of LCO, power of LNO, and safety and stability of LMO. [29] By including only a small portion of cobalt, NMC is also a less expensive cathode material, making it a viable option for large scale cells. [29] Furthermore, NMC experiences very little volume change during cycling ($< 2\%$) resulting in excellent cyclability. [35] Nickel and cobalt are the electrochemically active ions at low and high potential, respectively, giving NMC a high charge/discharge capacity. [35] Although exact capacity depends on the ratio of Ni:Co:Mn, Meng et al. [36] reported a capacity of ~150 mAh/g when cycled between 2.8 and 4.3 V. Similarly, Ohzuku et al. [37] demonstrated a capacity of ~150 mAh/g between 2.5 and 4.2 V. When they expanded the voltage window to 5 V the capacity increased to 220 mAh/g, but capacity faded to ~200 mAh/g as cycling continued. A drawback of NMC cathodes is the safety concerns caused by the inherent thermal instability of such a combination of layered metal oxides in the charged (fully delithiated) state. [29, 31] Nonetheless, the high capacity of NMC coupled with its excellent cyclability and electrochemical performance at high voltages makes it a promising choice for next generation LIBs, especially for electric vehicle applications. [38, 39]

I.2. Introduction to Aqueous Processing

The focus of current research and development efforts in modern lithium-ion batteries is twofold: meeting growing energy demands while reducing battery manufacturing costs. Electrode production alone amounts to about 47% of the total battery cost. [4] An electrode is first prepared by dispersing the necessary dry powders (active material and carbon black) in a solvent. A separate solution of binding material dissolved in the solvent is also added. The resultant mixture is a homogenous particulate dispersion, commonly referred to as a slurry. The slurry is then coated on to a current collector substrate and allowed to dry. The general procedure is the same for both anode and cathode, though materials vary. The cathode is by far the most expensive component of an LIB, with 70% of that cost

being materials and the associated processing. [40] A comprehensive cost review of LIBs for electric vehicles based on 80 published estimates from 2007 to 2014 determined that for major manufacturers, cost declined by 8% annually. [41] Recent R&D efforts have made major strides in reducing LIB cost from $400-600/kWh in 2015 to less than $300/kWh in 2016. [4, 11] In order to facilitate deep market penetration of electric vehicle technology, the Department of Energy's Vehicle Technology Office set a target price of LIBs at $125/kWh by the year 2022. [4] To meet this target, low cost materials and processing methods must be implemented. [11]

Solvent is a major cost factor in manufacturing lithium-ion batteries. Conventional electrode processing employs the organic solvent N-methyl-2-pyrrolidone (NMP), and is therefore referred to as organic processing. Not only is NMP an expensive solvent at more than $2.2/L, but it is classified as a volatile organic compound and must therefore be recollected as the electrode dries. The equipment required to recover NMP generates significant capital cost in industrial manufacturing plants. Capital cost is further increased by the need for explosion proof equipment since NMP is a combustible substance. Another major cost implication of organic processing is the high cost associated with removing NMP from the electrode. NMP has a high boiling point and low vapor pressure, thus more energy is required in the form of heated air flow as opposed to other solvents. [14]

In addition to high cost, the use of NMP in conventional electrode processing has serious environmental and safety concerns. [15, 42, 43] The OSHA Hazard Communication Standard classifies NMP as hazardous, listing reproductive toxicity, serious eye and skin irritation, and respiratory irritation as the primary hazards to personnel working with NMP. [44] The harmfulness of NMP to the reproductive system has been repeatedly confirmed in animal studies. [45-48] Other studies have found NMP is rapidly absorbed by the skin, inciting the urgent need to monitor occupational NMP exposure. [49-51]

In an effort to avoid the associated cost and deleterious effects of NMP, interest has turned towards a water based processing procedure, referred to as aqueous processing. Aqueous processing replaces the toxic, expensive organic solvent, NMP, with deionized water,

thereby significantly reducing electrode processing costs while avoiding highly toxic chemicals. With a lower boiling point than NMP, the use of deionized water requires less energy to dry the electrode, and it need not be recovered from the drying electrode. Deionized water itself also costs only $0.015/L, a small fraction of the cost of NMP. [14] Based on an internal processing evaluation completed at the DOE's Battery Manufacturing Facility at Oak Ridge National Laboratory, aqueous processing of electrodes has the potential to reduce processing costs by up to 70%, which translates to a total overall LIB cost reduction of 12%. [52]

The benefits of aqueous processing extend beyond cost as deionized water itself is entirely environmentally benign and nontoxic to humans. Also, with less energy required to dry electrodes, a transition to water based processing alleviates the environmental impact of LIB manufacturing. A life cycle analysis of LIBs for plug-in hybrid electric vehicles revealed over 50% of the global warming impact of LIBs comes from energy consumed during manufacturing. In fact, the same life cycle assessment concluded a switch to aqueous processing will reduce CO_2 emissions of a 10 kWh battery from 4400 kg when processed with NMP to 3400 kg when processed with water. The emissions reduction is due entirely to differences in the production phase. [53]

Aqueous processing of negative electrodes for LIBs has already been evaluated and implemented into industrial manufacturing with much success. [14, 42] However, aqueous processing of positive electrodes for LIBs has a unique set of challenges that must be overcome before it can be reasonably incorporated in industrial-scale battery manufacturing procedures. These issues include development of an effective water soluble binder to ensure good adhesion, particle agglomeration, and poor wettability of the aqueous cathode dispersion on the current collector. [11]

I.2.1. Water Soluble Binders
The binder in an electrode is typically a polymeric additive capable of ensuring good cohesion of electrode components and adhesion of the electrode to a current collector,

without sacrificing electrochemical performance. The binder also functions to properly disperse powders in the solvent, and provide necessary rheological properties of the dispersion for the purpose of coating. Furthermore, a binder must be electrochemically stable in the voltage range of the battery, and chemically inert to other materials in the cell. A quality binder also accommodates volume expansion of the electrode during operation. Perhaps one of the greatest challenges associated with finding a proper binder for aqueous processing is not that it must meet all of the aforementioned requirements, but that they must be achieved with the least amount of binder possible in the interest of energy density. [54]

The standard binder in commercial lithium-ion batteries is polyvinylidene fluoride (PVDF), due to its electrochemical stability and high adhesion. [55] Despite being an excellent binder in both anode and cathode, PVDF must be dissolved in the volatile organic solvent, NMP. [56] In addition, PVDF is a rather costly polymer. [57] Many researchers have experimented with various water soluble binders as replacements for PVDF in the cathode such as gums [52, 58-60], elastomers [61], polysaccharides, [62, 63], and polyacrylic acids [64-66] but no single binder has been established for aqueous processing. The problem is due in part to the fact that no aqueous binder thus far works for all cathode active materials because of their different chemical and physical properties. [55] Finding a universal water soluble binder that meets all of the standards of a quality binder is considered one of the major hurdles in implementing industrial aqueous processing of cathodes. [67]

The polysaccharide carboxymethyl cellulose (CMC) has been a popular binder choice in aqueous processing. CMC is inexpensive, and its molecular structure provides ideal rheological behavior of the cathode dispersion. [56] CMC is also thermally stable up to 200 °C and electrochemically stable between 0.02 and 5.00 V. [57] Moreover, literature has reported that CMC cathodes achieve at least equivalent electrochemical performance to that of PVDF cathodes, and in many cases exceeds the performance of PVDF cathodes. [57, 62, 68, 69]

The effectiveness of CMC as an aqueous binder, however, is limited to certain active materials. [64] In general, the inflexible cellulosic backbone of CMC makes it more suitable as a thickener in aqueous cathode dispersions. [54] Recently, researchers have turned their attention to polymeric binder systems that employ CMC in combination with a hydrophillic polymeric binder. This composite binder exploits the excellent rheological properties of CMC as a thickener in the slurry, as well as the highly desirable properties of a polymer (ie. flexibility and adhesiveness). By significantly improving adhesion, even when compared to PVDF, polymeric binder systems with CMC are facilitating superior electrochemical performance of the cathode when compared to PVDF cathodes. [54, 61, 70] A composition of CMC and styrene-butadiene copolymer latex is now widely used as the binder in aqueous processed graphite, Si, and TiO_2 anodes for LIBs. [43, 55, 71-73]

I.2.2. Particle Agglomeration

In addition to adhesion, an ideal water soluble binder would enable the formation of a homogenous cathode by properly dispersing particles in the solvent. Successfully dispersing the powder forms of active material and conductive additive in water remains an intrinsic challenge in aqueous processing. [14] A homogenous distribution of particles in the solvent is critical to forming an effective electronically conductive network in the dry cathode. The electronically conductive network formed among the active material, conductive additive, and current collector defines the electrochemical performance of a cell. Improper dispersion of particles in the solvent results in a non-uniform cathode morphology, causing charge/discharge reactions to be unevenly distributed. Consequently, "hot spots" subject to overcharge/discharge form and the full capacity of the cathode is underutilized. [74] Aqueous processing is uniquely challenging in that strong particle interaction caused by electrostatic forces and hydrogen bonding forms detrimental particle agglomerates [14, 58] In particular, the conductive additive, carbon black, is hydrophobic and therefore tends to form agglomerates rather than dispersing homogenously in an aqueous solvent. [75]

Agglomerates are caused by the attractive and repulsive potentials between particles generated by interparticle forces. The net potential of attractive and repulsive potentials determines a particle's stability in a colloidal dispersion. When the attractive potential is greater than the repulsive potential, particles will cluster together. Therefore, to increase stability, thereby minimizing particle agglomeration, the repulsive potential (ie. Coulombic force) between adjacent particles must be maximized. Experimentally, the degree of repulsion between similarly charged particles in a liquid is determined by measuring the zeta potential as a function of the solution's pH level. A zeta potential near zero indicates poor stability (tendency to agglomerate) as attractive van der Waals forces exceed Coulombic repulsive forces. A dispersion is considered to have good stability for higher zeta potential values. Li et al. [59] measured the zeta potential of aqueous carbon black dispersions, and found carbon black has a zeta potential of ~ – 16 mV in the pH range of cathode dispersions, indicating poor stability. The stability of carbon black in water can be improved by reducing the zeta potential further, or increasing it to a high positive value.

A major reason CMC became a popular binder in aqueous processing of electrodes, is its ability to adsorb to the surface of carbon black. [71] CMC is a highly negative polymer, thus its adsorption on carbon black results in a significantly more negative zeta potential value. [54] This means the inclusion of CMC in an aqueous cathode dispersion reduces agglomeration, ensuring a more homogenous distribution of carbon black particles in the electrode. [43]

Actually, CMC has a dual purpose: dispersion of hydrophobic carbon black particles, and forming necessary rheological properties for coating. [43] Carbon black is a small particle, so when CMC adsorbs to its surface much of the molecule remains free to adsorb to another carbon black particle. [54] The result is a well-developed network of CMC-bridged carbon black particles. This bridge network spans the entire electrode bulk, surrounding and supporting active material particles, effectively preventing the large active material particles from settling while the electrode dries. [54] The outcome is an electrode with a homogenous distribution of carbon black and active material. [54, 62, 69]

Although CMC is an effective dispersant in many cathodes, the extent to which it enables homogeneity is unique to each cathode material. Zhong et al. [56] used a polyacrylic latex (PAA) as the water soluble binder in NMC cathodes and compared the morphology and electrochemical performance of such cathodes with that of CMC and PVDF cathodes. They found CMC has difficulty dispersing NMC uniformly throughout the electrode, but SEM images showed electrodes with PAA had excellent surface uniformity and a homogenous distribution of particles comparable to that of PVDF cathodes. Consequently, the PAA NMC cathode had better cycling performance and rate capability with an initial specific capacity of 146 mAh/g and capacity retention of 96.4% after 100 cycles. In contrast, CMC and PVDF NMC cathodes had an initial specific capacity and capacity retention of 122 mAh/g and 88%, and 121 mAh/g and 75%, respectively.

Rather than relying solely on a binder material to disperse powders in the aqueous solvent, many researchers have experimented with surfactants to avoid the formation of agglomerates. The molecular structure of a surfactant includes both a hydrophobic and hydrophilic group. The short, carbonaceous hydrophobic chain of the surfactant adsorbs to the particle, reducing the interfacial energy between water and the particle, allowing it to disperse in water. [75] A surfactant is considered anionic or cationic based on the ionic property of the hydrophilic group.

Porcher et al. [75] studied the effects of three surfactants on the dispersion of carbon black in aqueous LFP cathode dispersions: an anionic surfactant, a cationic surfactant, and a non-ionic surfactant (TritonX-100). They found ionic surfactants corroded the aluminum foil current collector, and determined a 1 wt.% of the non-ionic surfactant, TritonX-100, was sufficient to properly disperse carbon black. C.C. Li et al. [43] experimented with anionic surfactants in LFP cathode dispersions and found poly(acrylic acid-co-maleic acid) (PAMA) produced the best results in terms of improved morphology and electrochemical performance.

J. Li et al. [59] added the cationic surfactant poly(ethyleneimine) (PEI) to aqueous LFP cathode dispersions and investigated its effects on electrode processing, particle

morphology, and electrochemical performance. Based on agglomerate size, dispersion viscosity, and particle distribution in dry cathodes, they found 1.5 wt. % PEI properly dispersed LFP cathode components. By reducing the size of agglomerates, cathodes with PEI had a more uniform surface compared to those without PEI. Electrochemical performance was optimized when 2 wt. % PEI was added. Li et al. concluded PEI is an effective dispersant for aqueous processed LFP cathodes.

I.2.3. Wettability

Another challenge unique to aqueous processing is poor wetting of the cathode dispersion on the aluminum foil current collector. [14, 58] This is due in part to the fact that aluminum foil has a surface energy of 47.9 mJ/m^2, whereas the surface tension of water is 72.8 mN/m. The high surface tension of water inhibits proper wetting of the cathode dispersion on aluminum foil. Conversely, the surface tension of NMP is 41.0 mN/m, thus wettability is a nonissue in conventional electrode processing. [60] Proper wetting on the substrate is instrumental in establishing an effective electronically conductive network between the cathode and the current collector.

Li et al. [60] proposed a method to improve the wettability of aqueous cathode dispersions by increasing the surface energy of the aluminum foil with corona plasma treatment. Corona plasma treatment increases the surface energy by removing hydrocarbons that are known to reduce a solid's surface energy while also introducing polar groups onto the surface of the aluminum foil. Since water is a polar molecule, these newly introduced polar groups make the aluminum foil substrate more attractive to the aqueous cathode dispersion. With this pretreatment, Li et al. were able to accomplish complete wetting of the cathode dispersion. Naturally, the superior wetting translated to excellent electrochemical performance.

I.3. Conclusion

In summary, aqueous processing of electrodes for LIBs offers the potential to significantly reduce manufacturing costs, as well as the environmental impact of lithium-ion batteries by avoiding the use of the toxic and expensive organic solvent, NMP. Aqueous processing has already been implemented in large-scale manufacturing of anodes, but issues arise in doing so for the cathode. One reason for this is the lack of a universal water soluble binder for the cathode. Certain hydrophilic binders have been found to function as well, and often better, than the conventional organic binder, PVDF, but the effectiveness of these binders is dependent on the active material. In addition, aqueous cathode dispersions tend to form agglomerates and exhibit poor wetting on the aluminum current collector due in part to the high surface tension of water. However, significant progress has been made in overcoming these challenges. Surfactants and certain binder materials have been used to successfully minimize agglomerates, while corona plasma treatment of the aluminum substrate has been proven to enable complete wetting. Overall, significant research endeavors continue to make progress towards complete integration of aqueous processing in industrial manufacturing of LIB cathodes.

CHAPTER II

AQUEOUS PROCESSING FOR HIGH ENERGY DENSITY LIBS

II.1. High Energy Density Lithium-Ion Batteries

Extensive research and development has been invested in lithium-ion batteries (LIBs) in an effort to make electric vehicle technologies a competitive alternative to internal combustion engines. Though much progress has been made in advancing LIBs for transportation applications, achieving specific energy and power requirements for EV's remains a major challenge. [76] It is generally agreed upon that an energy density of at least 225 Wh/kg is necessary for long range EV's. [77] Factors such as electrode porosity, thickness, and chemical composition strongly determine the energy and power capabilities of a battery. The volumetric energy density has been improved by decreasing electrode porosity to ~30% through calendering. [78, 79] Energy density has also been improved through careful optimization of the electrode composition to minimize inactive electrode materials such as carbon black and binder, effectively maximizing the amount of active material in the electrode. [78, 80, 81] Inactive materials are those which do not contribute to the capacity of the cell. They include carbon black and binder, as well as current collectors and separators. The active materials are those which participate in the intercalation/de-intercalation of the lithium ions during cycling.

In addition to decreasing porosity and minimizing inactive components in the electrode, the energy density of a cell can be improved by reducing the amount of other inactive components in the cell, namely current collectors and separators. Increasing electrode thickness is a straightforward approach to improving energy density in this way. By increasing electrode thickness, less inactive materials such as current collectors and separators are necessary to achieve the same capacity in a stacked cell. Active materials in electrodes have a relatively high specific capacity, but inactive materials in the cell significantly lower the overall cell energy density. For example, a graphite/NMC cell has a specific capacity of 150 mAh/g of NMC. Wood et al. [14] found when inactive

components such as binder, conductive additive, current collectors, and separators are factored in, the energy density of the cell is only 60% of the active material specific capacity, dropping to just 60 mAh/g. If the cathode thickness is doubled in a graphite/NMC model, and the anode thickness is adjusted accordingly, the specific capacity of the cell increases to 70 mAh/g, an improvement of 17%. [14] Thus, by reducing the fraction of inactive components, a thick electrode effectively increases the energy density of a cell. [14, 76, 77]

Despite very promising improvements in energy density, challenges in electrochemical performance inhibit the integration of thick electrodes in commercial LIBs. A thick electrode introduces inherent mass transport issues that limit the electrochemical performance of the cell at high charge/discharge rates. Singh et al. [82] investigated the electrochemical performance of high energy density NMC/graphite Li-ion cells assembled with thick electrodes, and compared the results to those of a cell with electrodes of standard thickness. Electrodes in conventional LIBs have a thickness between 50 and 60 μm. Singh et al.'s standard electrode had a thickness of 70 μm, corresponding to a cathode material mass loading of 17 mg/cm^2.The thick electrode was 320 μm – a mass loading of 72 mg/cm^2. The volumetric energy density of the standard electrode cell was 337 Wh/L, increasing 19% to 412 Wh/L when thick electrodes were used. However, rate performance results of the thick electrode cell showed inferior discharge capacities at C-rates exceeding C/2. Compared to their C/10 discharge capacities, standard and thick electrodes retained 91% and 95% of their capacity at a rate of C/5, respectively. At a rate of C/2, the standard electrode retained 85% of its capacity while the thick electrode retained only 45% of its capacity. The authors credit the significant capacity loss in thick electrodes at relatively high C-rates to large transport limitations inherent in thick electrodes. Specifically, lithium ions in the electrolyte phase experience mass transport limitations through the considerable depth of the thick electrode. Similarly, thick electrodes introduce more impedance for electron flow through the solid phase of the electrode to the current collector. These limitations are exaggerated at higher C-rates, when little time is allowed for lithium ions and electrons to properly diffuse through the electrode

Other researchers have observed the same electrochemical performance of thick electrode cells. Zheng et al. [76] studied the implications of thick NMC and LFP organically processed cathodes, since these two active materials are promising options for EV applications. The electrodes varied in thickness from 25 to 108 μm. For NMC, the energy density increased from 830 Wh/L with a thin (25 μm) electrode to 1200 Wh/L with a thick (108 μm) electrode. In the case of LFP, the energy density increased from 550 Wh/L to 700 Wh/L with thin and thick electrodes, respectively. Independent of thickness, full cells with graphite anodes delivered the rated capacity at low C-rates. However, as C-rate increased, thick NMC and LFP electrodes exhibited a serious reduction in discharge capacity. Zheng et al. focused on the C-rate at which each cell was capable of delivering 70% of its rated capacity, also known as the maximum working C-rate. Thin LFP electrodes had a maximum working C-rate of 20C, but comparably thick electrodes had a maximum working C-rate of only 2C. The same behavior was seen in NMC cathodes, with a maximum working C-rate of 10C and 1C for thin and thick electrodes, respectively. In fact, Zheng et al. report a linear relationship between electrode thickness and maximum working C-rate for both NMC and LFP.

Ghallagher et al. [77] observed the similar rate performance for thick NMC cathodes between 40 and 154 μm thick. Cycling was stable for the thick NMC electrodes when performed at an appropriate range of C-rates. At high C-rates, thick NMC electrodes delivered a fraction of their rated capacity. Furthermore, Porcher et al. [54] studied thick LFP cathodes and saw the same serious decrease in capacity at higher C-rates. All three of these researchers attribute the capacity loss in thick electrodes at high C-rates to transport limitations of Li-ions and electrons within the electrode. In fact, Zheng et al. [76] measured the impedance of each electrode and confirmed the internal resistance increases with increasing electrode thickness.

Lu et al. [83] published similar results for organically processed $LiNi_{0.8}Co_{0.15}Al_{0.05}O_2$ (NCA) electrodes with thicknesses ranging from 7 to 110 μm. In contrast to other researchers, Lu et al. evaluated the electrochemical performance of NCA/graphite full

cells with hybrid pulse power characterization (HPCC). The method of pulse charging and discharging more accurately simulates real operation in a hybrid electric vehicle. Their results confirmed a thick electrode increases energy density, but inherent transport issues limit the rate capability of thick electrodes. All electrodes delivered their rated capacity at low C-rates, but discharge capacities of thick electrodes plummeted at higher C-rates.

By reducing the amount of inactive material in a stacked cell, thick electrodes do indeed offer the opportunity to increase the energy density of a lithium-ion battery. However, poor rate performance at relatively fast discharge rates indicates energy density is improved at the expense of power density. Battery packs for EV applications must have both large energy density for extended mileage per charge, as well as an equally important large power density to accelerate the vehicle and charge via regenerative braking. Consequently, the current challenge is to increase energy density while maintaining power densities achievable with electrodes of standard thickness. Nonetheless, thick electrodes have a practical future in applications with low charge/discharge rates such as commercial and residential renewable energy storage and supply. [82]

The concept of increasing electrode thickness, and subsequently minimizing the fraction of inactive material in the cell, not only improves energy density but it simultaneously reduces the cost of a cell. In addition to increasing energy density, cost remains a challenge in implementing LIBs for EV's. The United States Department of Energy has set a target price of $125/kWh by the year 2022. [1] As mentioned in the previous chapter, replacing the expensive and toxic organic solvent, NMP, with water in electrode processing offers the opportunity for substantial cost reduction. Wood et al. [52] estimated the cost of an LIB can be reduced 12% with the use of aqueous processing, as opposed to organic processing with NMP. In another paper, Wood et al. [14] identify doubling the electrode thickness as a second method for significantly reducing the cost of LIBs, especially when done in conjunction with aqueous processing. They developed a cost model to predict the total EV battery pack cost savings for thick, aqueous processed electrodes, compared to standard size organically processed electrodes. The predicted total savings is 21.5% for a

graphite/NMC battery pack. Therefore, to achieve high energy density LIBs at a low cost, it is critical to study aqueous processing for thick electrodes.

II.2. Challenge of Aqueous Processed Electrodes for High Energy Density LIBs

To meet high energy density demands, thick positive electrodes of 100-200 μm are required in LIBs. Accordingly, a thick anode must be implemented to pair with the thick positive electrode. It has been found that the flexibility of a thick negative electrode coating is dependent on the graphite material chosen. Du et al. [84] found that a thick negative electrode (areal mass loading of 13.9 mg/cm^2) composed of the graphite material SCMG-BH, carbon black, and SBR/CMC binder had excellent flexibility. The irregular shape and rough surface of SCMG-BH particles provide ample sites for binder to adsorb and strongly bridge the particles to each other and the copper current collector. As a result, thick SCMG-NH anodes were deemed to have the mechanical integrity necessary for industrial manufacturing, where cell flexibility is crucial to successful roll-to-roll manufacturing, electrode punching, stacking, and jelly roll winding. Other graphite materials investigated exhibited cracking when subject to flexibility testing.

In contrast to negative electrodes, aqueous processing of positive electrodes is subject to inherent obstacles to achieving greater energy density with thick electrodes. When a thick cathode is prepared via aqueous processing the electrode coating cracks as it dries. The severity of such crack formations progressively worsens for increasingly thick electrodes. Consequently, aqueous processed cathodes are restricted to conservative thicknesses to avoid cracking. A standard aqueous processed positive electrode with areal mass loading of ~12.5 mg/cm^2 is completely devoid of cracks. Cracks appear when electrode areal mass loadings exceed ~15 mg/cm^2.

Loeffler et al. [57] were the first to publish evidence of cracks in aqueous processed positive electrodes. Figure 2 (a) shows an image of the crack formations observed in their electrode comprised of NMC, CMC, and carbon black. By excluding a hydrophilic polymeric binder and using only CMC as binder, the electrode cracks at a much lower

areal mass loading. They simply attribute the crack formations to large shrinkage of the CMC binder molecules during drying, and shortcomings in their lab-scale mixing equipment. Nonetheless, Loeffler et al. noted the effects of calendering on cracks. Figure 2 (b), (c), and (d) show a cracked electrode calendered at 17, 47, and 70 kg/cm, respectively. As the calendering force increases, the cracks reduce in size. Under 70 kg/cm of calendering force, all cracks have been closed. Furthermore, Loeffler et al. report the superior electrochemical performance of the electrode calendered at 70 kg/cm when compared to the other three electrodes.
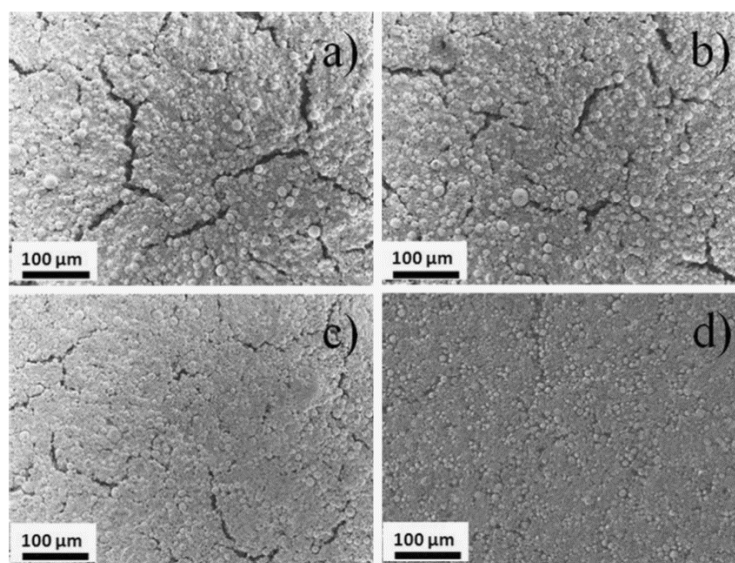
Figure 2: Electrode with areal mass loading of 7.5 mg/cm2 *(a)* uncalendared and calendered at *(b)* 17 kg/cm, *(c)* 47 kg/m and *(d)* 70 kg/cm, as presented in [57].

Du et al. [84] examined thick, aqueous processed cathodes for the purpose of high energy density LIBs. Figure 3 shows optical microscope images of NMC cathodes of various mass loadings. The electrode with 15 mg/cm^2 exhibits only subtle microcracks. However, the electrode with 17.5 mg/cm^2 loading has pronounced cracks with an average width and length of 50 μm and 300 μm, respectively. Cracks are seen to propagate further and increase in number as the mass loading continues to increase. In fact, the electrode with

25 mg/cm^2 loading had cracks which protruded all the way through to the aluminum foil current collector, resulting in weakened adhesion and delamination of the electrode from the current collector.
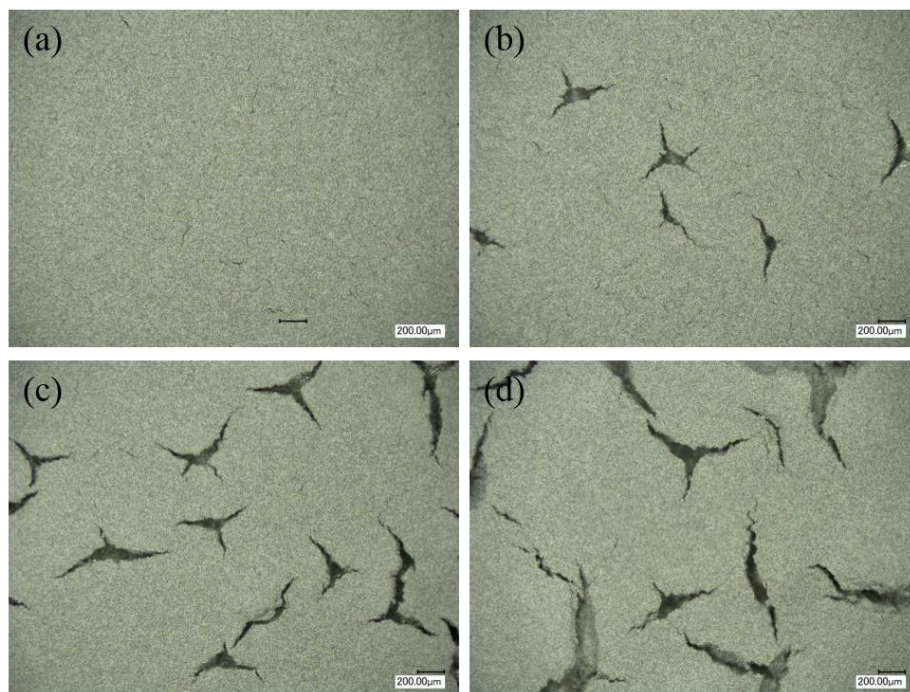
Figure 3: Optical microscope images of aqueous processed electrodes with areal mass loadings *(a)* 15 mg/cm^2, *(b)* 17.5 mg/cm^2, *(c)* 20 mg/cm^2, and *(d)* 25 mg/cm^2, as presented in [84]. The scale bar in all images is 200 µm.

To understand the effects such defects have on the electrochemical performance of a cell, Du et al. assembled pouch cells with the cracked electrodes of 25.1 mg/cm^2 loading. Figure 4 shows the rate performance results of a cell cycled between 2.5 and 4.2 V. For comparison, the voltage curves of an organically processed (solvent is NMP) electrode with 24.7 mg/cm^2 loading is also presented in Figure 4. Not surprisingly, delamination of electrode material due to deep cracks seriously impairs electrochemical performance.
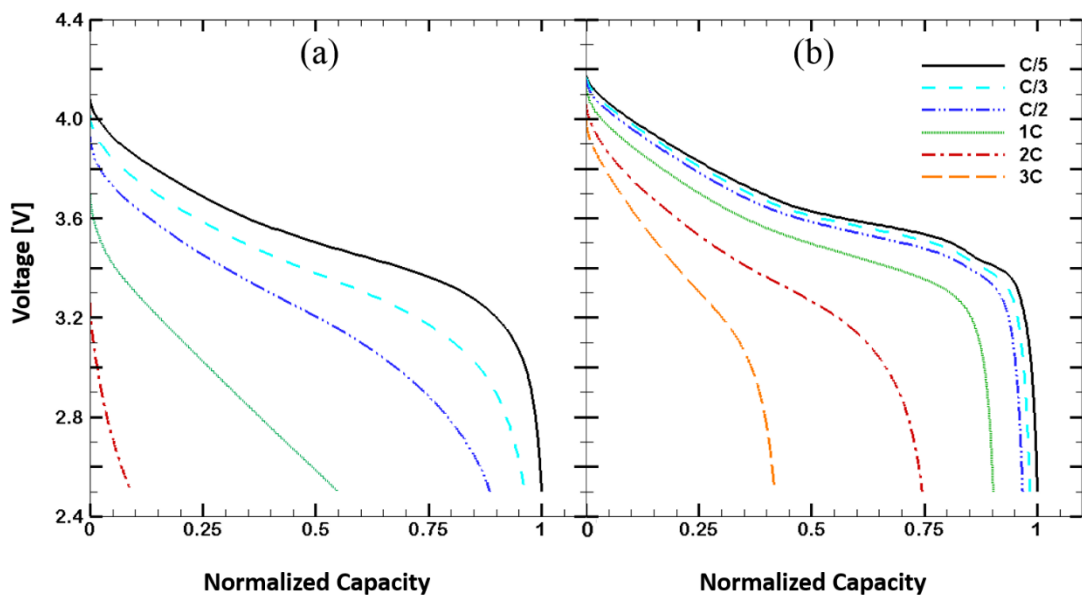
Figure 4: Discharge voltage profiles at different C-rates for pouch cells with NMC532 positive electrodes prepared with *(a)* 100% H_2O and *(b)* NMP as solvent.

When the thickest electrode (areal mass loading 25 mg/cm^2, Figure 3 (d)) was calendered, the large cracks could not be completely eliminated under the force of calendering. Du et al. also observed that an uneven distribution of material due to cracking caused the aluminum substrate to tear as it passed through the calendering machine. Figure 5 shows an optical microscope image of the calendered thick electrode, as well as the tears in the aluminum foil.
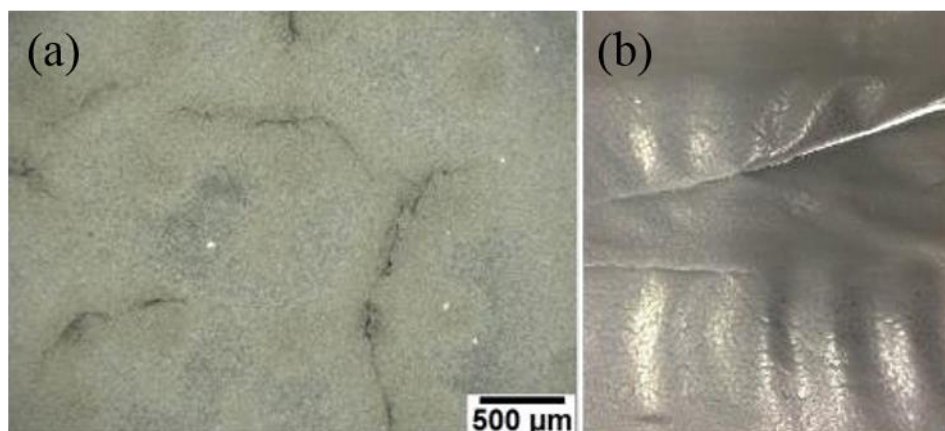
Figure 5: Optical microscope images of *(a)* cracked electrode (areal mass loading 25 mg/cm^2) after calendering and *(b)* tears in the aluminum foil substrate caused by calendering the cracked electrode as presented in [84].

In the same study, Du et al. [84] proposed an alternative manufacturing process with the hope of avoiding cracking. They employed what they refer to as a "two pass method" by coating one layer of standard mass loading (~12.5 mg/cm^2) upon another dry layer of the same standard mass loading, resulting in a thick electrode with ~25 mg/cm^2 loading. Although the coating appeared uniform and crack-free, interfacial resistance between the two layers resulted in very poor rate performance. The capacity retention was only 87% at C/5, 57% at C/2, and 17% at 1C. The cell failed to deliver any capacity at 2C. From this work, Du et al. concluded that additional methods must be investigated to eliminate cracking in thick, aqueous processed cathodes while maintaining low internal resistance.

II.3. Drying Induced Cracks in Thin Films

Drying induced cracks have been widely studied in concrete [85, 86], desiccated soils [87, 88], ceramic films [89, 90], colloidal dispersions [91, 92], and latex films [93, 94]. There is a general consensus that capillary pressure induced stresses are the cause of cracking in drying particulate dispersions. [94-97] Initially, particles suspended in a solvent are coated on a rigid substrate. Evaporation drives the air-liquid interface towards the substrate.

When the air-liquid interface encounters the now close-packed particle network, capillary action forms liquid menisci among surface particles, giving rise to a negative capillary pressure. In the case of spherical particles, the capillary pressure (P_{cap}) is given as:

$$P_{cap} = \frac{2\gamma\cos\theta}{r_p}$$

(1)

where γ is the liquid-vapor surface tension of the solvent, θ is the liquid-solid contact angle, and r_p is the pore radius. The equivalent pore radius of a film can be approximated as

$$r_p = \frac{2(1-\phi)}{\phi\rho_s S}$$

(2)

where ϕ is the particle volume fraction, ρ_s is the density of the solid phase, and S is the total surface area of the particles. [98]

Scaling inversely with pore radius, capillary pressure can be enormous. The pressure gradient across the air-liquid interface puts the entire film into compression, shrinking the film as it dries. Film shrinkage is constrained by the rigid substrate and stress is generated in the film. If this stress exceeds some critical value, the film will crack to alleviate stress.

II.3.1. Elastic Fracture Model of Cracking

From a macroscopic prospective, continuum models have commonly been employed to elucidate the stress-strain relationship in thin films on a rigid substrate. [99] For such models, cracking is analogous to cracking of thin, elastic films under residual tensile stresses. Griffith's energy balance criterion [100] for the brittle fracture of elastic solids is then applicable to describe equilibrium crack propagation. Griffith's energy criterion balances the elastic energy recovered by crack propagation (G_c) with the increased surface energy from creating the two new surfaces of a crack (W):

$$G_c = W \tag{3}$$

Routh and Russel [97] derived a well-known macroscopic stress-strain relationship for latex dispersions by developing a linear viscoelastic model for the deformation of two spheres compressed by an external force. Applying this stress-strain relationship to a network of identical spheres, along with Griffith's energy balance criterion, Tirumkudulu and Russel [94] derived an expression for the critical stress (σ_c) for initiation of a single crack:

$$\frac{\sigma_c R}{2\gamma} = 0.1877 \left(\frac{2R}{h} \right)^{2/3} \left(\frac{GM\phi_{rcp}R}{2\gamma} \right)^{1/3} \tag{4}$$

where R is the particle radius, γ is the liquid-vapor surface tension of the solvent, h the thickness of the film at crack initiation, G is the shear modulus of particles, M is the coordination number, and ϕ_{rcp} is the particle volume fraction at random close packing. Based on this equation, thinner films will have a higher critical stress for crack initiation, making them less prone to cracking. This expression for the critical stress of cracking has been found to be in good agreement with experimental results. [94, 101]

Tirumkudulu and Russel claim capillary pressure will form a void free, continuous film free from cracks if the capillary stress required to deform particles so all voids are closed is less than the critical stress for cracking. [94] Thus, a critical thickness can be obtained by equating capillary stress in the crack-free state at the maximum compressive strain (ε_{max}) to the critical stress for cracking:

$$h_{max} = \frac{37\gamma}{GM\phi_{rcp}(\varepsilon_{max})^3} \tag{5}$$

where $\varepsilon_{max} = 1 - \phi_{rcp}$. Surprisingly, Equation 5 suggests the critical thickness is independent of particle size. It also predicts the critical thickness to increase with decreasing shear modulus. Both predictions based on Equation 5 have been found to be inconsistent with experimental results. In their study of granular ceramic films, Chiu et al.

[89, 90] prepared aqueous alumina dispersions with different particle sizes. They found critical cracking thickness increased with increasing particle size, implying films of large particles are less likely to crack. However, latex and zirconia films had considerably lower critical thicknesses compared to films of alumina with similar sized particles, indicating solid phase properties strongly influence critical thickness as well. Chiu et al. also determined the critical tensile stress at cracking in granular ceramic films scaled with capillary stress, and cracking is independent of drying rate.

Similarly, from their experiments with aqueous dispersions containing particles of various sizes and shear moduli, Singh and Tirumkudulu [101] found the measured critical thickness to be over two orders of magnitude greater than that predicted by Equation 5. Moreover, scanning electron microscope (SEM) images of their films indicated negligible particle deformation, even for films containing particles with relatively low shear moduli. Thus, Singh and Tirumkudulu refer to Equation 5 as the critical thickness in a *strain-limited* regime, applicable only to very soft particles capable of completely deforming visco-elastically to fill all voids. For particles with higher shear moduli, they predicted an alternative *stress-limited* regime that agreed well with experimental results. In the stress-limited regime particles deform only partially, or not at all, under compressive capillary forces until the maximum capillary pressure is reached and the air-liquid interface recedes into the particle network. Setting the capillary stress at the maximum capillary pressure equal to the critical stress for cracking (Equation 4), they derived a more generally applicable expression for critical thickness:

$$h_{\max} = 0.64 \left(\frac{GM\phi_{rcp}R^3}{2\gamma} \right)^{1/2} \left(\frac{2\gamma}{P_{\max}R} \right)^{3/2} \tag{6}$$

where the dimensionless maximum capillary pressure for a collection of identical spheres is given by:

$$\frac{P_{\max}R}{2\gamma} = \frac{3\cos\theta}{2} \left(\frac{\phi_{rcp}}{1-\phi_{rcp}} \right) \tag{7}$$

In contrast to the strain-limited regime, the stress-limited regime predicts $h_{max} \sim (1/\gamma)^{1/2}$ and $h_{max} \sim G^{1/2}$, indicating the crack-free thickness of a film can be increased by reducing the surface tension of the solvent and/or using particles with higher shear modulus.

II.3.2. Elastic-Plastic Fracture Model of Cracking

The elastic model employed in the preceding section relies on linear elastic fracture mechanics, which describes reversible brittle fracture – implying cracks will close when residual drying stresses are removed. However, cracks are known to form in aqueous concrete [102] and soil [88] suspensions while the material is still saturated and therefore subject to plastic deformation. Consequently, an elastic model of brittle fracture in thin films fails to provide a complete explanation of the phenomenon in some films by disregarding the effect of plastic deformation.

Goehring et al. [103] developed a scaling relationship to predict the relative effect of plastic yielding in fracture by comparing the yield stress (σ_Y) to the stress at maximum capillary pressure (σ_0):

$$\frac{\sigma_0}{\sigma_Y} \sim \frac{\gamma}{\varphi M \gamma_p} \tag{8}$$

where φ is the solid volume fraction, M is the coordination number, γ_p is the surface energy of the solid material, and γ is the surface tension of the solvent. When $\sigma_0/\sigma_Y \ll 1$ plastic effects are negligible and the film can be assumed to be a perfectly brittle material. When $\sigma_0/\sigma_Y \gg 1$ plastic yielding is the dominating cracking mechanism. Because plastic deformation is by definition non-reversible, it is typically associated with a change in the film's microstructure. Goehring et al. derived the aforementioned scaling relationship by studying films of hard latex. They observed that when they repeatedly halted evaporation mid drying to eliminate capillary stress, crack openings narrowed only ~20%, rather than 100% closure predicted by traditional linear elastic models. Atomic force microscopy

revealed that as a crack propagated, particles within the immediate vicinity of the crack faces rearranged themselves. This alteration in the film's microstructure introduces irreversible strain, explaining why nearly 80% of the crack opening remains despite a sudden interruption of evaporation.

The plastic yield stress of an aggregated particle network is:

$$\sigma_Y = \frac{\varphi M F_{max}}{4\pi R^2} \tag{9}$$

where R is the particle radius and F_{max} is the maximum attractive interparticle force between two neighboring particles. [104] The addition of plastic yielding introduces an irreversible loss of energy in the thermodynamics of crack propagation. Goehring et al. [103] present a modified version of Griffith's energy balance criterion for elastic fracture to account for the irreversible plastic fracture energy loss (U_p):

$$G_c = W + U_p \tag{10}$$

An estimation of the recovered elastic energy (G_c) as a summation of reversible work (W) and plastic losses proved consistent with experimental observations. [103] Hallet et al. [88] likewise modified Griffith's energy balance criterion to more accurately describe cracking in desiccating soil samples and reached the same conclusion. Experimental results confirmed an elastic-plastic model better captured the fracture mechanics in wet soil samples.

Slowik et al. [105] accounted for plastic deformation in a numerical simulation of drying induced cracking in aqueous dispersions of cement-like materials. They developed a 2-dimensional particle-scale model to understand the effect of particle size and properties of the liquid phase on capillary pressure build-up and cracking risk. Their model accounted for three primary forces: gravitational force, capillary force, and interparticle forces. Adapting Equation 4 for a particle-scale model, the critical stress for cracking in a particular pore was determined by the strength of the attractive interparticle forces. The

interparticle forces considered were van der Waals and electrostatic forces, the sum of which gives a resultant force equal to the critical cracking stress. If the local in-plane capillary pressure force exceeded the resultant attractive interparticle force between adjacent particles a crack initiated.

The numerical solution is an iterative implicit solution which attempts to find a state of equilibrium among gravitational forces, capillary pressure, and interparticle forces. Water pressure is a control parameter increased incrementally to obtain a final solution. In each iteration a new water front is calculated in accordance with the water pressure, particles are shifted in ways that minimize the potential energy of the system, and interparticle interactions are updated. The remaining volume of water is also calculated in each iteration based on the new water front, assuming 2D particles have unit thickness. The maximum capillary pressure is reached and the simulation ends when a subsequent water pressure increment no longer provides physically sound results. Figure 6 shows simulation results as presented by Slowik et al. for particles ranging in size from 4 to 32 μm. The results show the nucleation of a crack at 24 kPa. As pressure increases, the crack widens and propagates further into the bulk of the material.
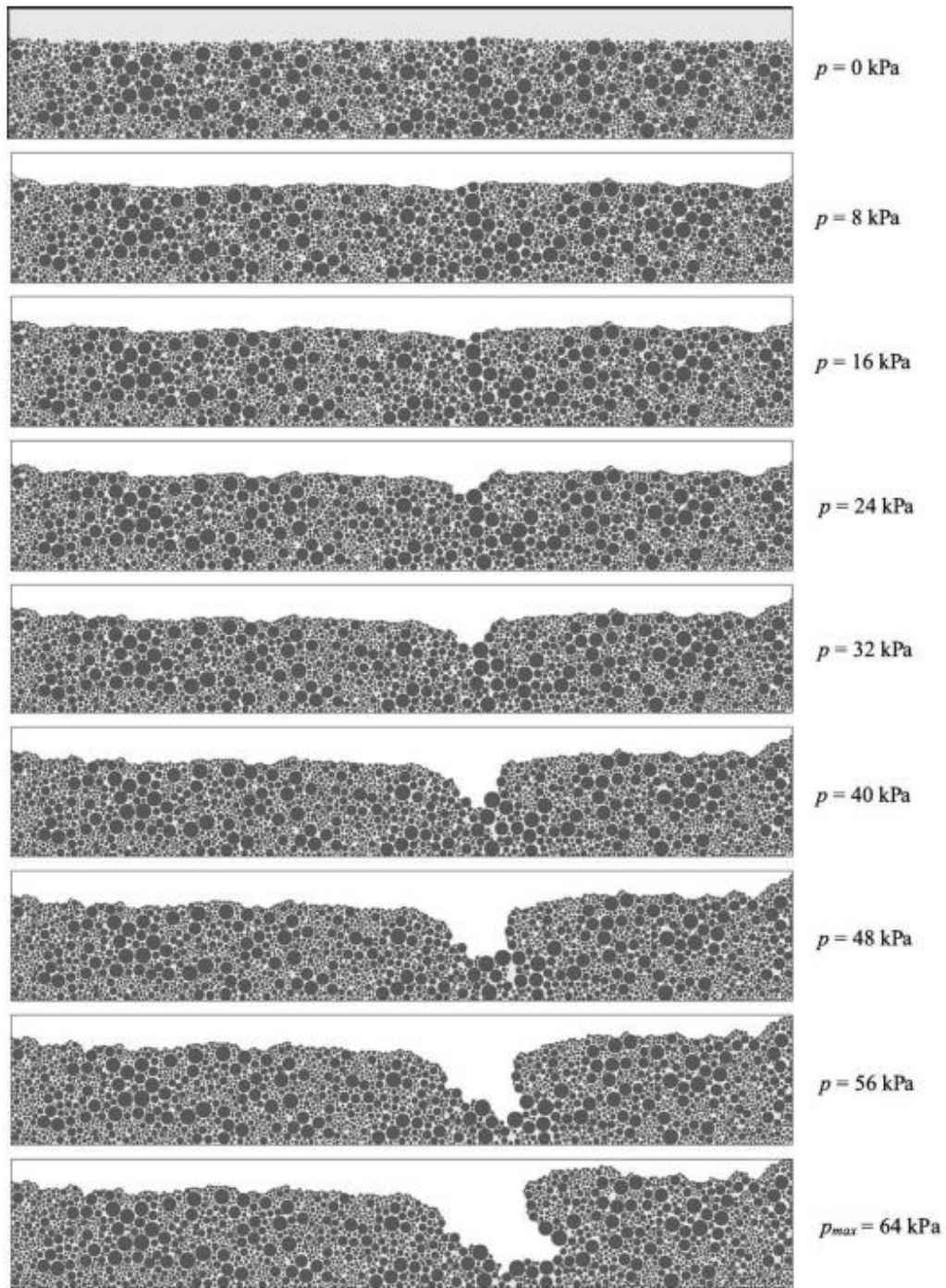
Figure 6: Results of the simulation developed presented in [105] for particle sizes 4 – 32 µm. Invasion of air into the particle network indicates a crack has initiated at a capillary pressure of 24 kPa.

The maximum capillary pressure forces determined numerically agreed with those measured experimentally. The 2D simulation also agreed with qualitative experimental observations of plastic shrinkage cracking. As seen in Figure 6, air entry into the particle network did not occur everywhere at once, nor at the same capillary pressure. Instead, air enters the local pore system. When the attractive interparticle forces become negligible, the material had cracked. As the crack formed and propagated, Figure 6 shows the particles nearest to the crack face rearranging themselves – indicative of plastic yielding.

A detailed particle-level explanation of plastic shrinkage cracking was developed by Shin et al. [106] based on experimental observations of desiccation cracks in 273 different aqueous dispersions of fine-grained soils. The films varied in thickness and pore fluid chemistry, and were exposed to different evaporation rates. A high resolution camera was used to simultaneously capture time-lapse images of the drying film while capillary pressure and water content were measured as each film dried. Surprisingly, the results were qualitatively the same for all 273 films. Figure 7 shows a typical example of the capillary pressure and water content as measured by Shin et al. As seen in Figure 7, capillary pressure is initially nonexistent. Only once the air-liquid interface reaches the soil sediment do liquid menisci form to generate a negative capillary pressure. The capillary pressure increases slowly as the water content continues to decline at a constant rate. A short time later, the capillary pressure dramatically increases. The inflection point occurs at the moment air first penetrates the pores of the saturated particle network.
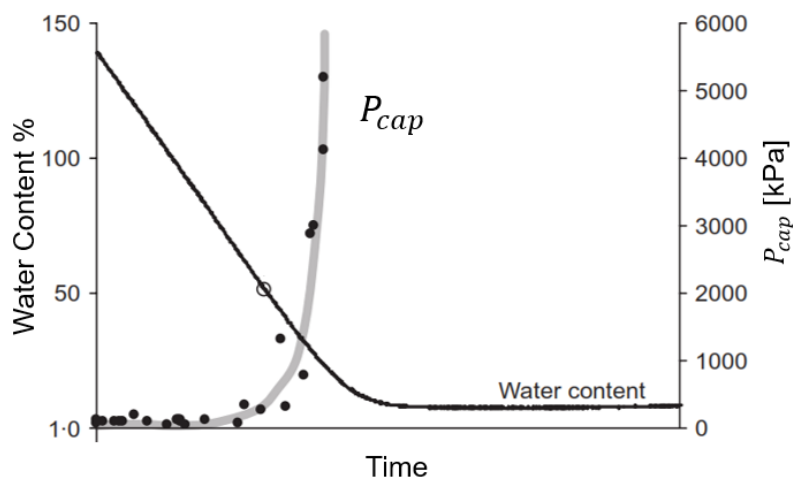
Figure 7: Time evolution of capillary pressure and water content in a drying thin film as presented in [106].

Comparing capillary pressure and water content measurements with the time-lapse images, Shin et al. observed that in all 273 films tested, desiccation cracks initiated at the exact instant air penetrated the pores of the particle network. According to Figure 7, that occurs during the period of constant evaporation. From these results, they concluded cracks initiate at the maximum capillary pressure, when air first invades the soil, and the saturated soil is still in its plastic stage. Shin et al. also found that cracks always nucleated at surface defects first – where pores are widest and are thus weak spots in the film for air to invade. Their novel explanation of cracking in fine-grained soils based on these experimental results can be applied to understand cracking in other thin films made of non-deformable, hard particles, including graphite anode slurries for LIBs. [86, 98, 102]

II.3.3. Particle-Scale Stages of Crack Formation

Initially, when any particulate dispersion is coated on to a substrate, particles are suspended in the solvent (see Figure 8 (a)). A particulate dispersion of hard particles will experience three distinct drying phases. [99] First, a period of constant evaporation rate causes the air-liquid interface to descend towards the substrate, while particles

34

simultaneously diffuse and sediment toward the substrate. In this phase of drying, the reduction in the film's volume is equivalent to the volume of solvent evaporated. Therefore, the duration of the first drying period is dependent on the initial volume fraction of solvent.
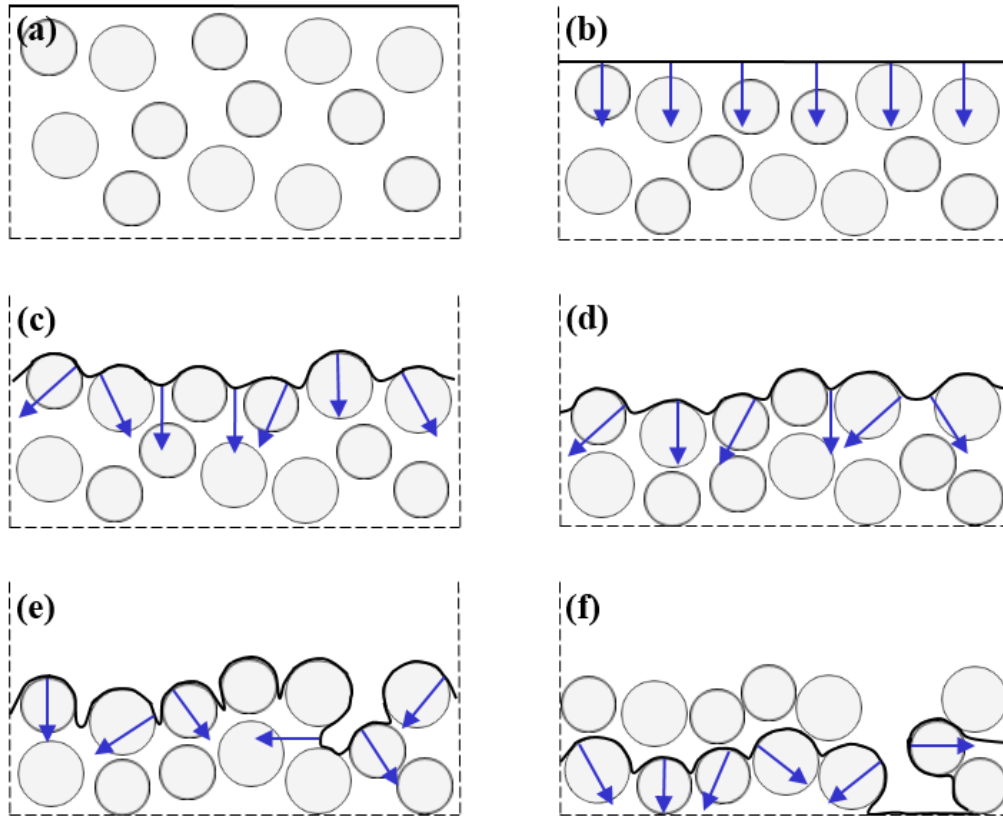
Figure 8: Stages of crack formation. *(a)* Particles are initially dispersed in solvent. Evaporation drives air-liquid interface towards the substrate. *(b)* Air-liquid interface reaches the surface of the particle network. *(c)* Liquid menisci form on surface particles, generating a negative capillary pressure that forces particles to consolidate further. *(d)* Resultant local pore size varies and eventually *(e)* air invades the largest pore. Horizontal capillary forces widen the pore and an in-plane tensile stress develops, initiating a crack. *(f)* Air invades further pores and the crack propagates.

The second phase of drying is also defined by a period of constant evaporation rate. However, the onset of the second phase is marked by the arrival of the air-liquid interface at the sediment surface (Figure 8 (b)). As evaporation continues, air would like to invade the pores of the particle network but strong particle wetting prevents this from happening as capillary action forms liquid menisci bridging adjacent particles on the surface (Figure 8 (c)). The menisci generate a negative capillary pressure within the pores of the sediment. The effect of this pressure gradient between the air-liquid interface and the bulk fluid in the particle network is twofold: it drives fluid flow from the bulk to the surface to maintain a constant evaporation rate and it generates a compressive force on the particle network perpendicular to the air-liquid interface. In response to the compressive capillary pressure force, the particle network begins to consolidate. The surface of the particle network and the air-liquid interface adhering to it recede at the same rate. Therefore, like phase one, the volume reduction of the particle network is equivalent to the volume of water evaporated. As the particle network consolidates, pore sizes continuously decrease, effectively increasing the negative capillary pressure while simultaneously improving the effective strength of the film.

Eventually, increased stiffness of the particle network halts any further consolidation. As evaporation continues, capillary pressure increases dramatically until the liquid-solid adhesion forces forming menisci are overcome and the air-liquid interface invades the particle network. (Figure 8 (d)). The capillary pressure at which air enters the particle network is known as the air entry value, or critical capillary pressure. The critical capillary pressure is determined by the size and shape of the local pores so air will not simultaneously invade the entire particle network. It is known that the magnitude of the critical capillary pressure decreases with increasing pore size. [102, 106] Thus, air will penetrate large pores first, where liquid menisci are forced to bridge over relatively large interparticle distances, meaning liquid-solid adhesion forces are weaker. Often the largest pores are associated with defects in the film such as agglomerates and air bubbles.

Invasion of air into a pore marks a transition from vertical displacement of the local particles to horizontal displacement as compressive forces normal to the air-liquid

36

interface now act in the plane of the film, forcing particles into the electrode bulk. The pore widens as neighboring particles are compacted. In-plane tensile stresses quickly develop as horizontal shrinkage is constrained by the film's attachment to a rigid substrate. Stress increases as local capillary pressure rapidly builds to force the air-liquid interface further into the bulk of the particle network to maintain a constant evaporation rate. If the mounting in-plane tensile stress exceeds the strength of the film, a crack is formed to relieve the local capillary pressure. (Figure 8 (d)). The process is repeated deeper in the particle network where the invading air front has widened pores at its tip. Local capillary pressure again increases to exceed adhesion forces forming menisci, the air-liquid interface invades further, and the crack propagates (Figure 8 (e)).

As the air-liquid interface invades further into the particle network, evaporation becomes limited by the transportation of water vapor out of the pores within the bulk of the film. Consequently, the evaporation rate decreases, marking the beginning of the third and final phase of drying. Eventually, portions of the particle network become unsaturated as the air-liquid interface passes through the particle network under the force of an equilibrium capillary pressure determined by the relative humidity.

II.4. Theory of Cracking Applied to LIB Electrodes

An electrode slurry is accurately represented as a particulate dispersion of particles with a relatively high shear modulus (i.e. non-deforming particles). Coated on a current collector, drying electrode slurries are subject to horizontal shrinkage constraints and subsequent risk of cracking. Particles in an electrode slurry do not deform under the forces of capillary pressure since eventual electrochemical cycling requires the electrode microstructure be porous. Therefore, the critical thickness derived from the assumption particles completely deform to fill voids (Equation 5) is not applicable to electrode slurries. Rather, the stress-limited regime proposed by Singh and Tirumkudulu [101] is expected to accurately predict the risk of cracking in drying electrode coatings. Then the critical thickness of an electrode is suspected to scale with the inverse square root of the surface tension of the solvent. The

surface tension of water (72.8 mN/m, 20 °C) is much higher than that of the conventional organic solvent, NMP (40.79 mN/m, 20 °C). In the context of a stress-limited regime (Equation 6), the large variance in solvent surface tension can be identified as the reason why thick, aqueous processed electrodes crack while organically processed electrodes of similar thickness are crack-free. The low surface tension of NMP increases the critical cracking thickness of the electrode to a value beyond that of interest for high energy density LIBs.

CHAPTER III

ENABLING AQUEOUS PROCESSING OF THICK, CRACK-FREE
POSITIVE ELECTRODES

III.1. Introduction

Crack formation in a thin films composed of hard particles, such as an LIB electrode slurry, is strongly dependent on the fluid phase of the dispersion. The critical crack-free film thickness is inversely proportional to the surface tension of the solvent. [101] The surface tension of water (72.8 mN/m, 20 °C) is much higher than the surface tension of the organic solvent NMP (40.79 mN/m, 20 °C). [107] As a result, in the range of electrode thicknesses of interest for high energy density LIBs (100-200 μm) aqueous processed electrodes show drying induced cracks, whereas organically processed electrodes of similar thickness do not. In an effort to capitalize on the environmental and economic advantages of aqueous processing while still enabling high energy density LIBs, a novel aqueous processing procedure was proposed. In this research, a composite solvent of H_2O+2-proponal (IPA) is investigated as a method to reduce surface tension of the solvent in aqueous slurries, thereby avoiding cracking in thick positive electrodes.

Ghahremani et al. reported that the surface tension of aqueous alcohol mixtures is significantly less than that of water alone when only a small mole fraction of alcohol is added (see Figure 9). [108]
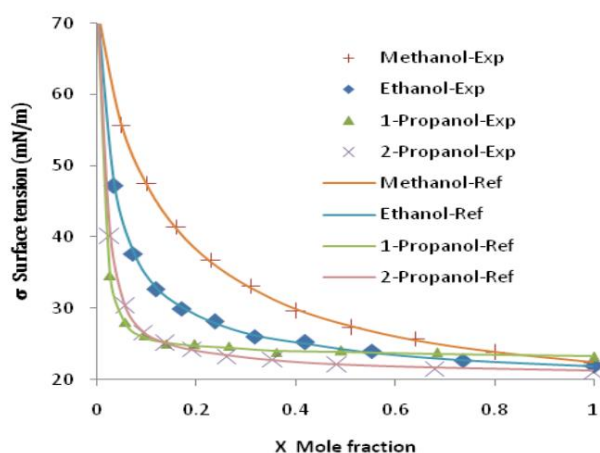
Figure 9: Mole fraction of alcohol vs. surface tension of dilute aqueous alcohol solution for various alcohols, as presented in [108].

2-propanol (IPA) was selected for this study as the alcohol additive in the solvent since it is miscible with water and the surface tension of IPA is very low (21.7 mN/m, 20 °C). [107] IPA is also inexpensive and readily available in typical battery manufacturing laboratories. The effect of multiple aqueous solvents containing up to 20 wt. % IPA was investigated.

To understand the effect of IPA on crack formation, the surface tension of the proposed novel aqueous solvents was experimentally investigated by contact angle measurements. Thick electrodes were fabricated with aq. IPA solutions as solvent, and any subsequent cracking was imaged and compared to the baseline electrode – a thick electrode fabricated with 100% H_2O as solvent. In addition, pouch cells were assembled to evaluate the electrochemical performance of thick aqueous processed electrodes fabricated with IPA.

III.2. Experimental Methods

Nine dilute aqueous IPA solutions with a range of 0 to 20 wt. % IPA were investigated. The contact angles of each solution on three substrates commonly used in aqueous processing, namely aluminum foil, carbon coated foil, and corona treated foil, were

measured by a goniometer (Model 260, Rame-hart Instrument Co., Figure 10). Each contact angle was averaged from five measurements. The corona treated foil was first treated by corona plasma discharge (Compak 2000, Enrocon) at an energy density of 4.4 J/cm^2.
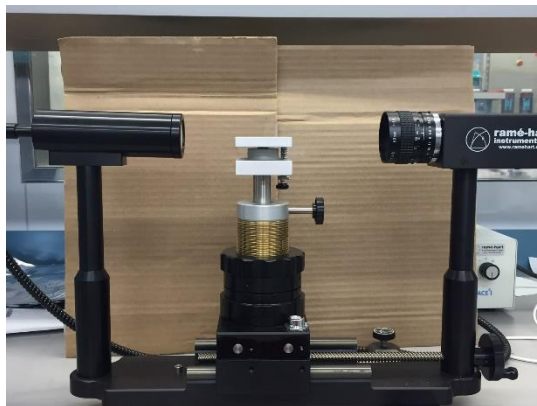
Figure 10: Goniometer used to measure the contact angle of each aq. IPA solution on three common substrates.

Cathode slurry was made with the active material $LiNi_{0.5}Mn_{0.3}Co_{0.2}O_2$ (NMC532, Toda America) and carbon black (Li-100, Denka) as conductive additive. A solution of 2 wt. % CMC (Ashland) dissolved in water via ball milling overnight served as a thickener, allowing the slurry to achieve the necessary shear thinning behavior. Acrylic polymer emulsion (Ashland) with a 45.8% solids content emulsified in water was added as a binder. The cathode slurry was prepared in a wt. % ratio of 90:5:1:4 NMC532:carbon black:CMC:arylic polymer emulsion, respectively. Aqueous IPA solutions ranging from 0 wt. % IPA to 20 wt. % IPA were used as solvent to achieve a slurry solids content of 50%. Active material and H_2O were first added to the CMC solution and mixed for five minutes. Carbon black was added in two portions, mixing in the first half for five minutes followed by the second half. Acrylic polymer emulsion was added last. The slurry was mixed for a total of one hour and fifteen minutes using a high shear mixer set at 4000 rpms

(NETZSCH Premier Technologies, Figure 11). For those slurries containing IPA, the appropriate wt. % of IPA was mixed in after the slurry had mixed for 45 minutes.

Figure 11: High shear mixer used to mix the electrode slurry *(left)*, and a close up image of the mixing mechanism *(right)*.

The slurry was coated on carbon coated aluminum foil using a doctor blade, and allowed to dry at room temperature (20 °C) in a dry room (RH 0.1-0.2%). An optical microscope (VHX-5000, Keyence, Figure 12) was used to collect time-lapse images of each drying electrode to capture any crack nucleation and subsequent propagation. A central point of the electrode was imaged every two minutes immediately following coating until the microstructure had stabilized (ie. five or more images were taken with no change in surface pattern).

Figure 12: Optical microscope used to collect time-lapse images of the drying electrode coatings.

Two cathode slurries with the same composition as mentioned previously were mixed in a planetary mixer (Ross, PDM ½, Figure 13) for the purpose of fabricating electrodes for pouch cells. The solvents were aq. IPA solutions containing 10 and 20 wt. % IPA, respectively. Each slurry was then coated by a custom slot die coater (Frontier Industrial Technology, Figure 13) onto an aluminum foil substrate, and immediately dried in an internal heating zone consisting of two IR lamps and seven convection ovens. The dried electrode coatings had areal mass loadings of ~ 25 mg/cm^2. Before manufacturing pouch cells, the electrodes underwent a secondary drying procedure in a vacuum oven at 90 °C for at least two hours. Single unit pouch cells (Figure 14) were assembled with a graphite anode. Celgard 2325 was used as a separator, and the electrolyte was 1.2 M LiPF$_6$ in ethylene carbonate/diethyl carbonate. In addition, three electrode pouch cells were assembled for which lithium metal served as the reference electrode. With a Maccor Series 4000 Automated Test System at 30 °C, the cells were cycled between 2.5 and 4.2 V from C/5 to 3C followed by 100 cycles at C/3 to investigate rate capability and capacity retention, respectively.

Figure 13: *(Left)* Planetary mixer used to mix large quantities of slurry for the slot die coater (*middle*). *(Right)* A side view of the slot die coater showing the space in which the heated drying zone is contained.
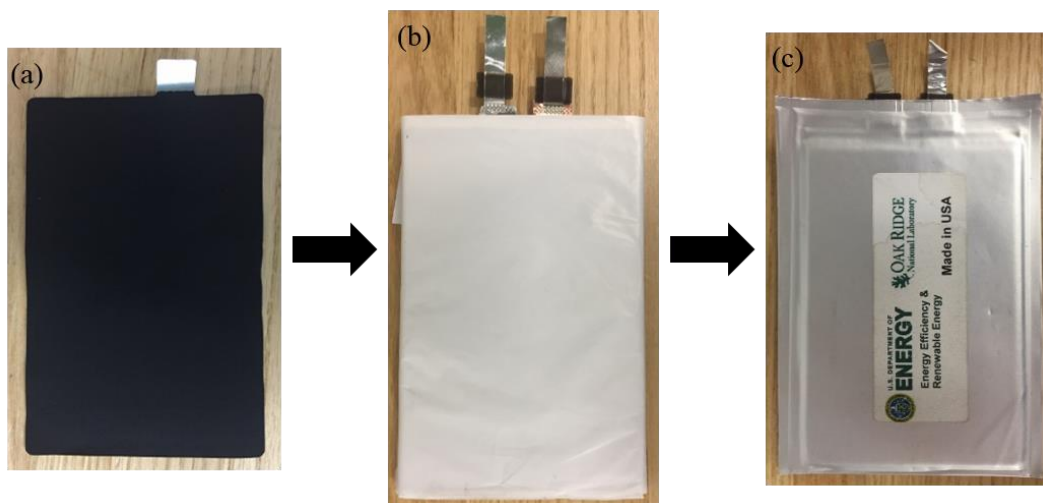
Figure 14: Pouch cell assembly. *(a)* Electrode for pouch cell, including current collector free of electrode material to attach tab. *(b)* Electrode stack consisting of anode, cathode, and separator. Tabs are welded to the electrodes for external circuit connection. *(c)* Electrode stack is placed in the pouch cell envelope which is then filled with electrolyte and sealed in vacuum.

III.3. Results and Discussion

III.3.1. Surface Tension of Aqueous IPA Solutions

The contact angle of each aqueous IPA solution is shown in Figure 15. The graph displays each solution's contact angle on three common substrates in aqueous processing. There is a clear trend of decreasing contact angle with increasing fraction of IPA in the solvent. Contact angle is directly related to surface tension, thus contact angle measurements of aqueous IPA solutions indicate surface tension decreases with increasing IPA content. The black dashed line in Figure 15 marks the contact angle of NMP on aluminum foil. The addition of 20% IPA reduces the contact angle between aluminum foil and the aqueous solvent to nearly that of NMP on aluminum foil. A lower contact angle improves wettability of the aqueous slurry as well, eliminating the need for corona plasma pretreatment of the aluminum foil substrate.
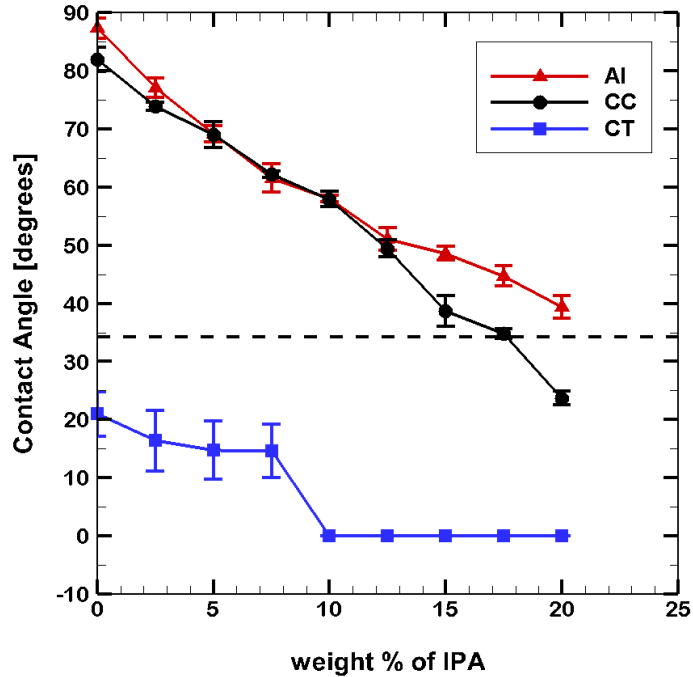
Figure 15: Contact angle of nine aqueous IPA solutions, ranging from 0% IPA to 20% IPA, on three common cathode substrates – aluminum (Al), carbon coated foil (CC), and corona treated foil (CT).

The smallest contact angle is achieved with at least 10% IPA on corona treated aluminum foil. Upon releasing the droplet from the pipette it spread across the foil, making the droplet impossible to image with the goniometer. Figure 16 is an example of a droplet with 10% IPA on corona treated aluminum foil. Figure 17 through Figure 19 display select images captured with the goniometer. For comparison, images of NMP droplets on each substrate can be seen in Figure 20.
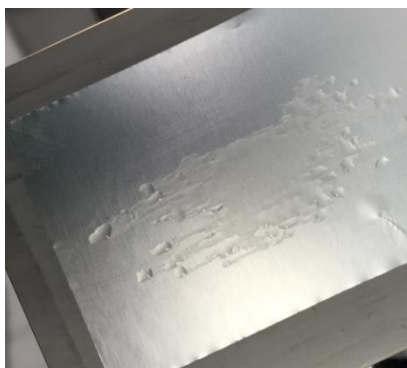
Figure 16: A droplet of solvent with 10% IPA on corona treated aluminum foil. All solvent compositions with 10% or more IPA displayed this same behavior with corona treated foil.
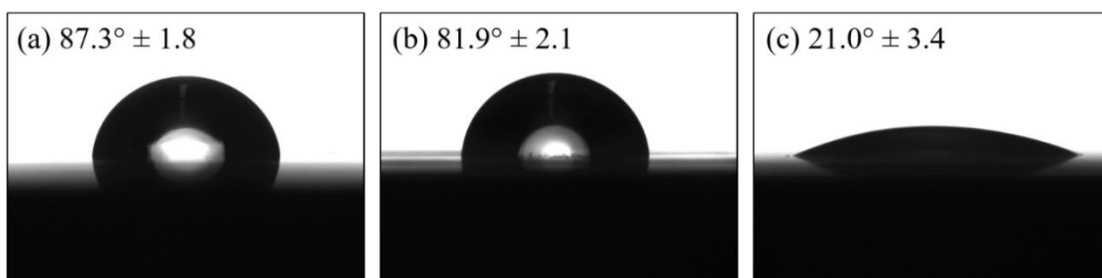
Figure 17: Images of solvent droplets containing 0% IPA on *(a)* aluminum foil, *(b)* carbon coated foil and *(c)* corona treated foil.
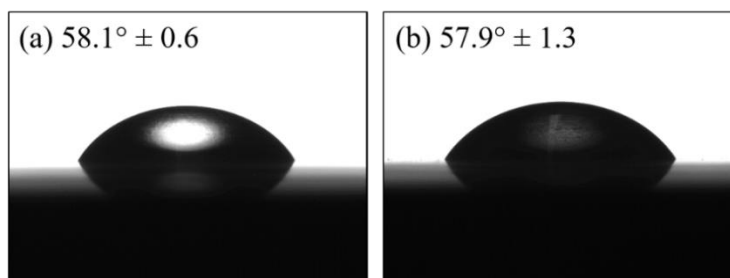
Figure 18: Images of solvent droplets containing 10% IPA on *(a)* aluminum foil and *(b)* carbon coated foil. Contact angle was 0° on corona treated foil.
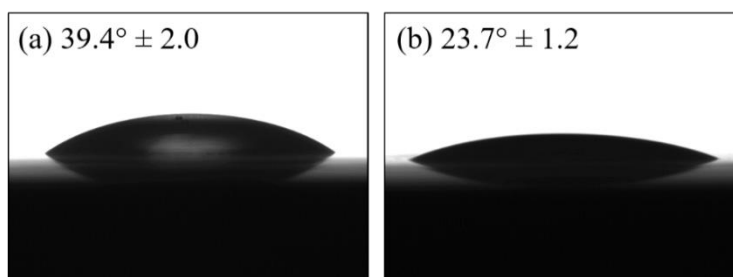
Figure 19: Images of solvent droplets containing 20% IPA on *(a)* aluminum foil and *(b)* carbon coated foil. Contact angle was 0° on corona treated foil.
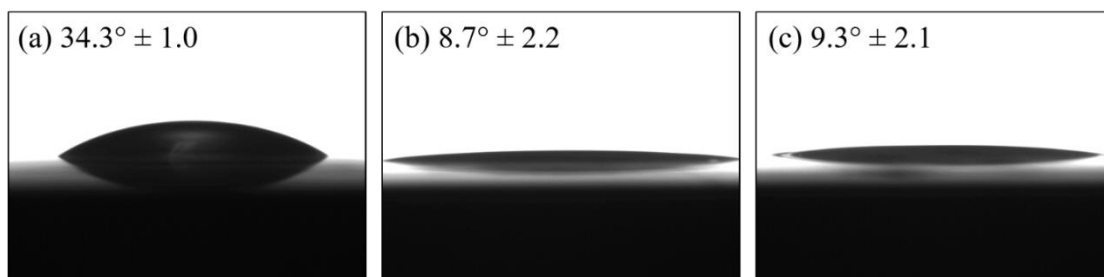
Figure 20: Images of NMP droplets on *(a)* aluminum foil, *(b)* carbon coated foil and *(c)* corona treated foil.

The surface tension of each aq. IPA solution was also calculated directly using an equation derived by Connors and Wright which relates surface tension to the composition of IPA + water solutions:

$$\gamma = \gamma_1 - \left[1 + \frac{0.970x_1}{1 - 0.984x_1}\right] x_2(\gamma_1 - \gamma_2) \tag{11}$$

where x_1 is the mole fraction of water, x_2 is the mole fraction of IPA, γ_1 is the surface tension of water, and γ_2 is the surface tension of IPA. [109] Figure 21 shows the rapid decrease in surface tension with increasing fraction of IPA. The results correlate well with contact angle measurements on an aluminum foil substrate. By adding 20% IPA the

contact angle is not only comparable to that of NMP on aluminum foil, but the surface tension is also dramatically reduced to 32.3 mN/m.
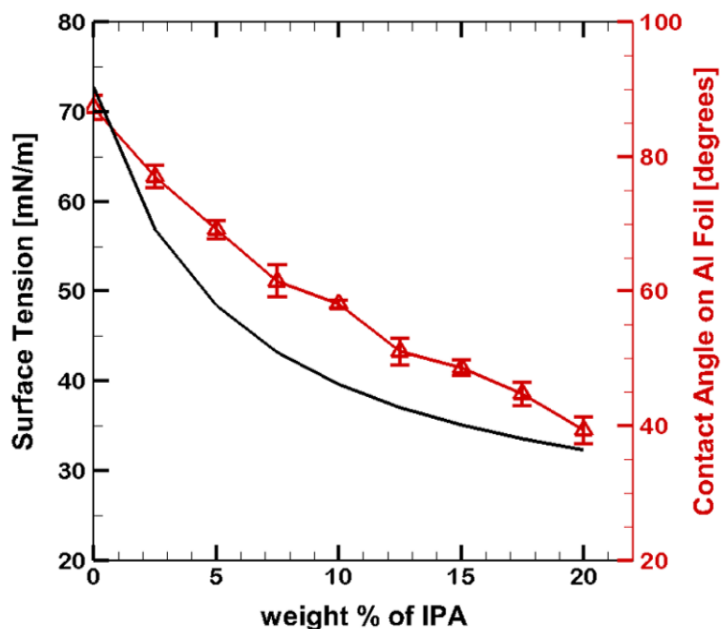
Figure 21: Calculated surface tension and measured contact angle between aluminum foil and aq. IPA solutions of varying composition.

III.3.2. Images of Crack Formation in Doctor Blade Coatings

The time evolution of cracking in a thick electrode coating using 100% H_2O as solvent is shown in Figure 22. Initially, the coating appears uniform, indicating the air-liquid interface has not yet descended to a network of particles (Figure 22 (a)). The more textured image in Figure 22 (b) suggests the air-liquid interface has reached the particle network, so surface particles are no longer completely surrounded by fluid. A defect appears in Figure 22 (b) – attributed to an air bubble trapped in the slurry. The renewed appearance of uniformity in Figure 22 (c) suggests particles have consolidated under capillary pressure forces imposed by the air-liquid interface. The first crack is seen to initiate from the defect in Figure 22 (c). This observation is in accordance with reports that defects in a film

promote cracking. [94, 110] Other cracks appear to spontaneously initiate in Figure 22 (d). As time elapses, the cracks widen and propagate across the coating. After just 36 minutes of drying, the crack formation is stabilized (Figure 22 (h)). This time scale is in agreement with reports that cracking occurs in the period of constant evaporation while the entire coating is still saturated. [106]

Figure 22: Optical microscope images of doctor blade coating (areal mass loading 27.4 mg/cm^2) prepared with 100% H$_2$O as solvent drying at 20 °C for *(a)* 0 minutes, *(b)* 12 minutes, *(c)* 24 minutes, *(d)* 26 minutes, *(e)* 28 minutes, *(f)* 30 minutes, *(g)* 32 minutes, *(h)* 36 minutes, and *(i)* 2 hours. The scale bar in all images is 200 µm.

Figure 23 shows the time evolution of drying for a thick electrode coating fabricated using an aq. IPA solution containing 10% IPA as solvent. Defects caused by air bubbles in the

slurry first appear in Figure 23 (b), almost all of which serve as nucleation sites for the first cracks in Figure 23 (c). Cracks then propagate a relatively short distance in Figure 23 (d) and (e). In contrast to Figure 22, the only significant cracks which appear in this coating are consequences of defects (i.e. air bubbles) in the slurry. However, other hairline cracks become apparent upon close inspection of Figure 23 (f).

Figure 23: Optical microscope images of doctor blade coating (areal mass loading 25.1 mg/cm^2) prepared with 10% IPA added to H$_2$O as solvent drying at 20 °C for *(a)* 0 minutes, *(b)* 14 minutes, *(c)* 18 minutes, *(d)* 22 minutes, *(e)* 26 minutes, and *(f)* 2 hours. The scale bar in all images is 200 µm.

Images of the drying process for a thick electrode coating with 12% IPA added to H$_2$O are presented in Figure 24. Again, defects are made apparent as the coating dries (Figure 24 (b)), and a crack initiates at one such defect in Figure 24 (c) then propagates (Figure 24 (d) – (f)). Figure 24 gives the impression that the coating with 12% IPA as solvent is crack-free, with the exception of cracks nucleating from rare defects. Further investigation of the dry coating under the optical microscope proved Figure 24 (h) was not a representative image of cracking in this coating. A more accurate representation is shown in Figure 25.

The narrow cracks seen in Figure 25 can be assumed to have not initiated at a defect, indicating cracking is not entirely eliminated in this coating.
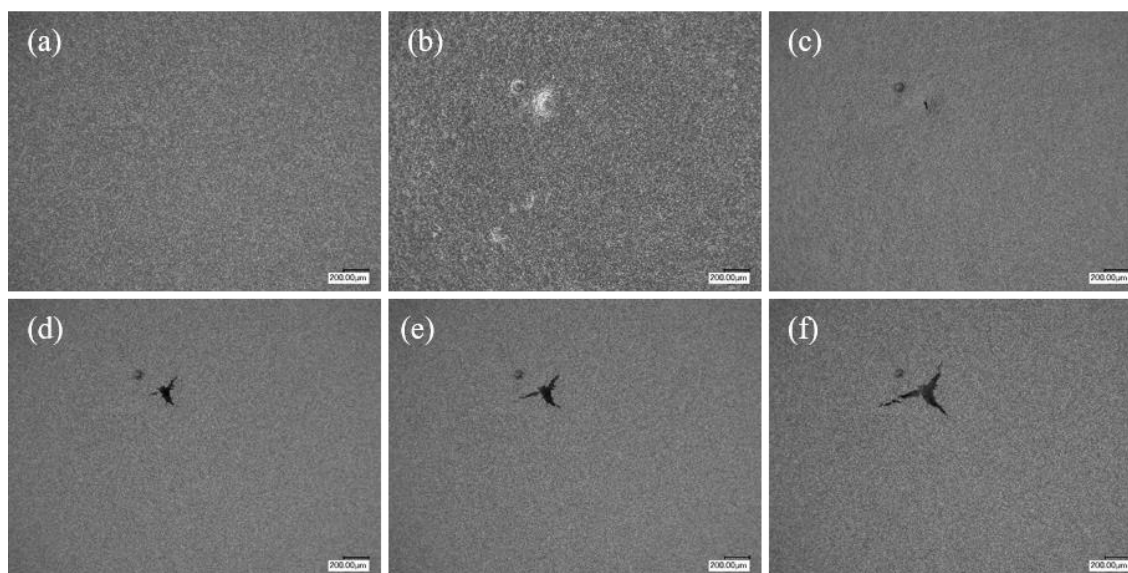
Figure 24: Optical microscope images of doctor blade coating (areal mass loading 25.4 mg/cm^2) prepared with 12% IPA added to H$_2$O as solvent drying at 20 °C for *(a)* 0 minutes, *(b)* 6 minutes, *(c)* 10 minutes, *(d)* 14 minutes, *(e)* 16 minutes, and *(f)* 2 hours. The scale bar in all images is 200 µm.
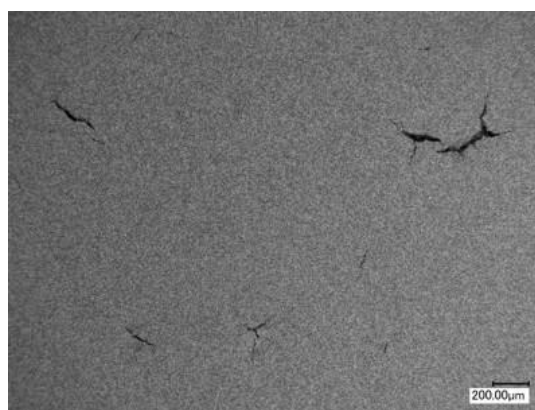
Figure 25: A more representative optical microscope image of cracks observed in the dry coating made with 12% IPA as solvent. The scale bar is 200 µm.

When a thick electrode with 15% IPA in H_2O was coated, optical microscope images of the time evolution of drying (Figure 26) showed a primarily uniform coating. Like previous coatings, a minor defect appears in Figure 26 (b), which leads to a crack forming in Figure 26 (c). In contrast to the other coatings however, this crack propagates only a few tens of microns (Figure 26 (d)). Similar to the 12% IPA coating, the time-lapse images of this coating did not capture an accurate representation of the coating's final crack formation. Figure 27 shows the sparse distribution of short hairline cracks found across the entirety of the coating made with 15% IPA as solvent.
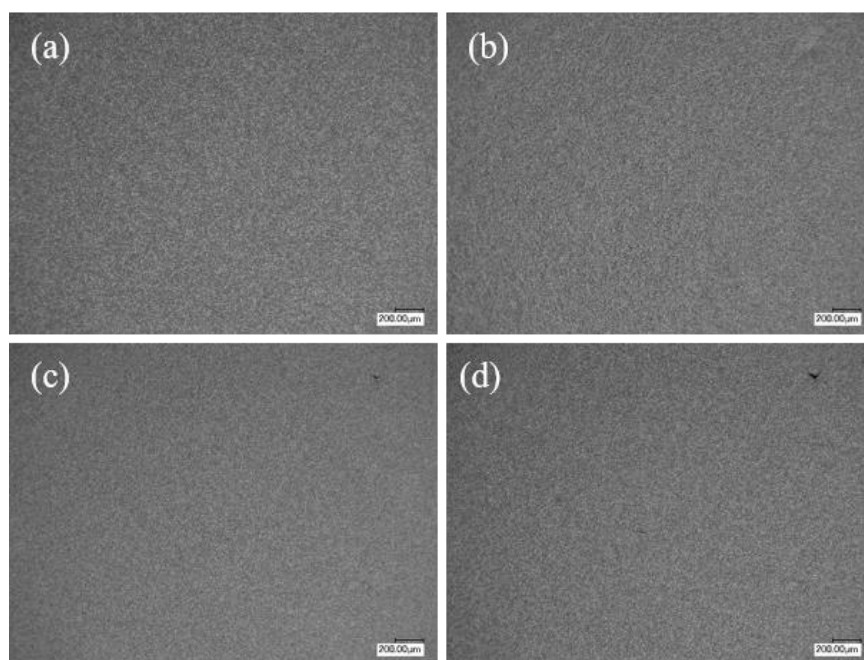
Figure 26: Optical microscope images of doctor blade coating (areal mass loading 24.8 mg/cm^2) prepared with 15% IPA added to H_2O as solvent drying at 20 °C for *(a)* 0 minutes, *(b)* 8 minutes, *(c)* 14 minutes, and *(d)* 2 hours. The scale bar in all images is 200 µm.
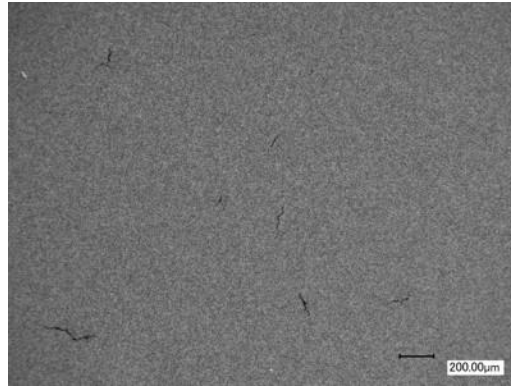
Figure 27: An optical microscope image representative of the final cracks observed in the coating prepared with 15% IPA as solvent. The scale bar is 200 μm.

The time evolution of a drying thick electrode coating fabricated with 20% IPA in H_2O as solvent is shown in Figure 28. In accordance with all other observations of cracking in doctor blade coatings, a crack initiates at a defect in the coating which first appears in Figure 28 (b). Once the crack initiates in Figure 28 (c), it propagates ~100 μm in Figure 28 (d) & (e). Figure 28 shows the only cracks to form in this coating with 20% IPA are those initiated by defects.
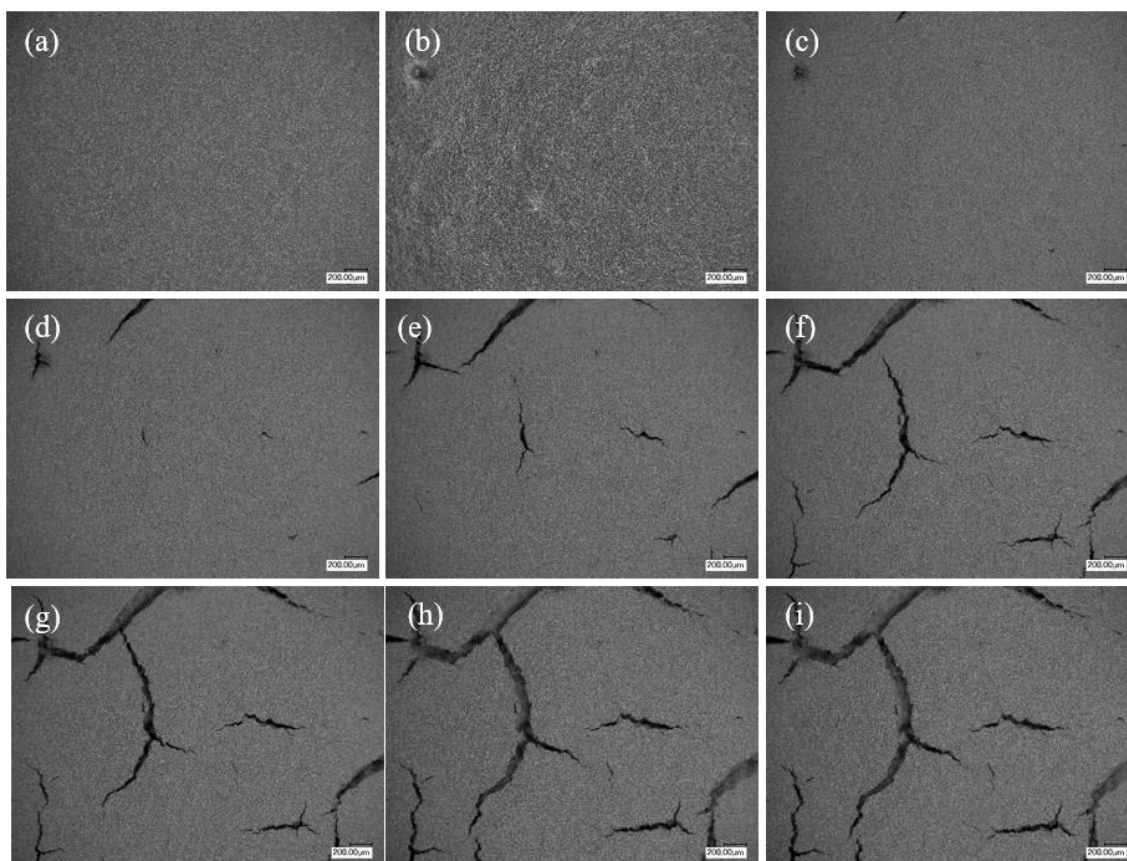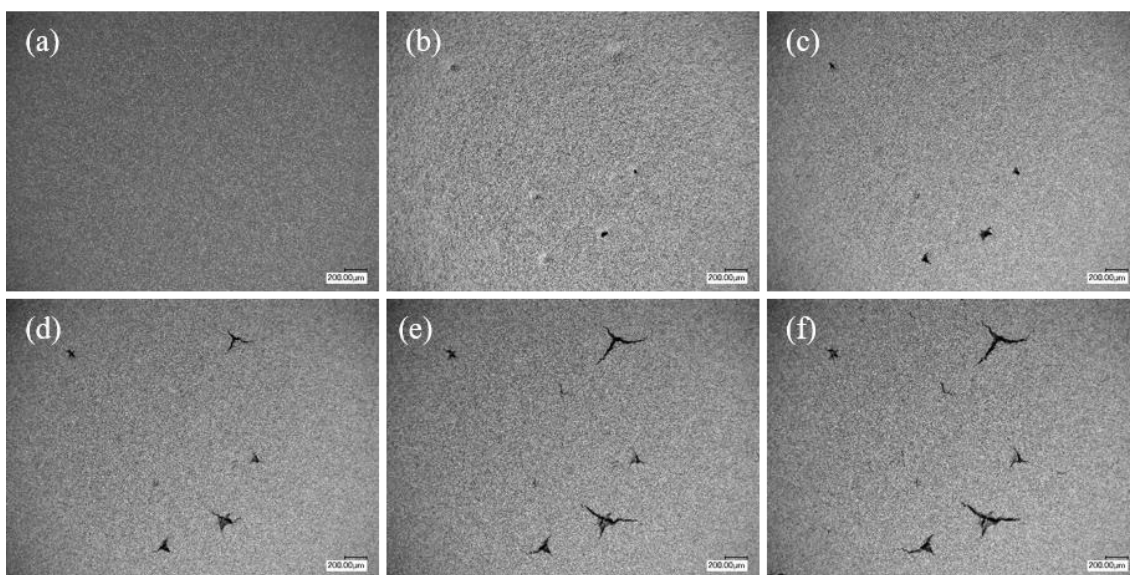
Figure 28: Optical microscope images of doctor blade coating (areal mass loading 24.2 mg/cm^2) prepared with 20% IPA added to H$_2$O as solvent drying at 20 °C for *(a)* 0 minutes, *(b)* 8 minutes, *(c)* 10 minutes, *(d)* 12 minutes, *(e)* 18 minutes, and *(f)* 2 hours. The scale bar in all images is 200 µm.

Figure 29 shows the final crack formation of each thick electrode coated with a composite solvent of IPA + H$_2$O in various weight ratios. For comparison, the thick electrode coated with 100% H$_2$O as solvent is also included in Figure 29. It is clear the addition of IPA to the aqueous solvent has considerable effects on the final morphology of thick, aqueous processed electrodes. Cracking is dramatically mitigated with the addition of just 10% IPA to the aqueous solvent (Figure 29 (b)). As more IPA is included in the aqueous solvent, cracking is further improved (Figure 29 (c) & (d)). Without taking into account the effect of defects inherent in small-scale electrode preparation procedures, the addition of 20% IPA appears to successfully avoid all cracking in thick electrodes (Figure 29 (e)).
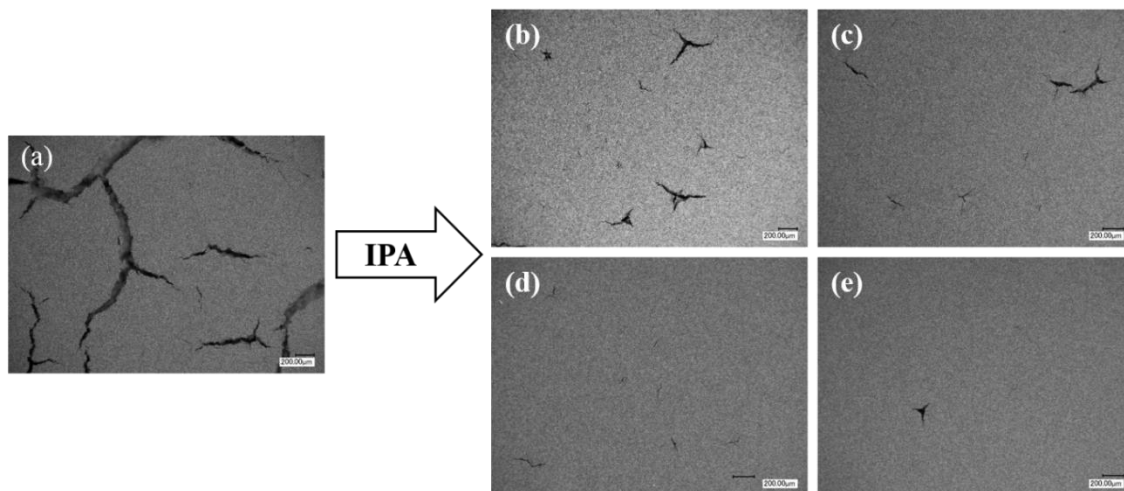
Figure 29: Optical microscope images of final crack formations observed in doctor blade coatings (areal loading ~25 mg/cm^2) dried at 20 °C and prepared with solvents composed of *(a)* 100% H_2O, *(b)* H_2O + 10% IPA, *(c)* H_2O + 12% IPA, *(d)* H_2O + 15% IPA, and *(e)* H_2O + 20% IPA. The scale bar in all images is 200 µm.

Several additional doctor blade coatings of varying thicknesses were prepared to determine the critical electrode thickness/loading for each solvent composition. The observed maximum crack-free mass loading associated with each solvent composition is presented in Figure 30. The critical mass loading increases with increasing fraction of IPA in the solvent. This trend is attributed to the reduction in surface tension with the addition of IPA (refer back to Figure 21) When the critical mass loading is plotted versus $\left(1/\gamma^{1/2}\right)$ where γ is the calculated surface tension of the solvent, a linear relationship is obtained with an R^2 value of 0.9346. A linear relationship is predicted in Equation 6 where critical thickness is a function of bulk properties of the solid phase and solvent surface tension. Since the same solids are used in every slurry, only the solvent surface tension is changing and thus a linear relationship is expected.
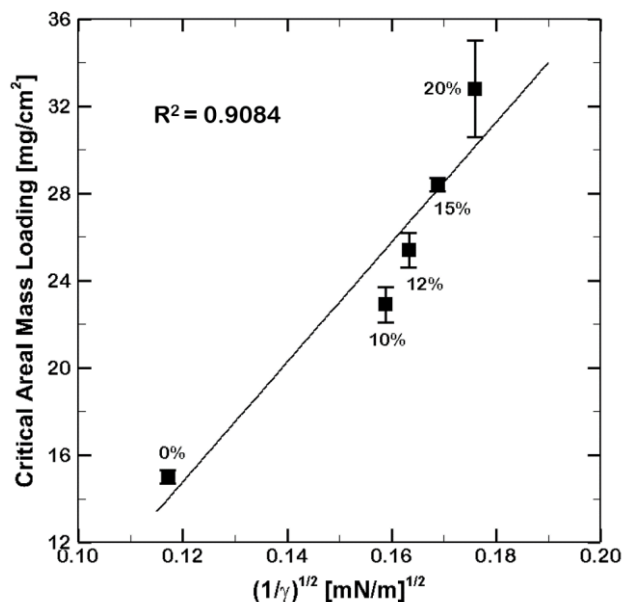
Figure 30: Critical cathode mass loading associated with each solvent composition (indicated in the figure) versus the inverse square root of the solvent's calculated surface tension.

III.3.3. Electrochemical Performance

Based on the results of the doctor blade coatings, a slurry using 10% IPA in H_2O as solvent, and another using 20% IPA in H_2O as solvent were prepared for pouch cell assembly. The slurries were coated via slot die coater (areal loading ~25 mg/cm^2), immediately dried, and then imaged using an optical microscope to observe any cracking. The electrode coatings were then calendered to ~40% porosity and imaged again to observe any changes in the morphology after calendering. Images of the 10% IPA coating before and after calendering are presented in Figure 31. Drying induced cracks were apparent across the entire coating before calendering (Figure 31 (a)). Figure 31 (b) shows a uniform coating after calendering. In fact, no cracks were observed in the 10% IPA coating after calendering. The narrow, shallow cracks in the 10% IPA coating were healed by calendering as cracked material was forced to merge under the force of calendering. This is in accordance with other observations of calendering curing cracks in electrodes. [57] As shown in Figure 32, the 20% IPA coating was crack-free before calendering,

meaning 20% IPA was sufficient to avoid all drying induced cracks in thick aqueous processed electrodes.
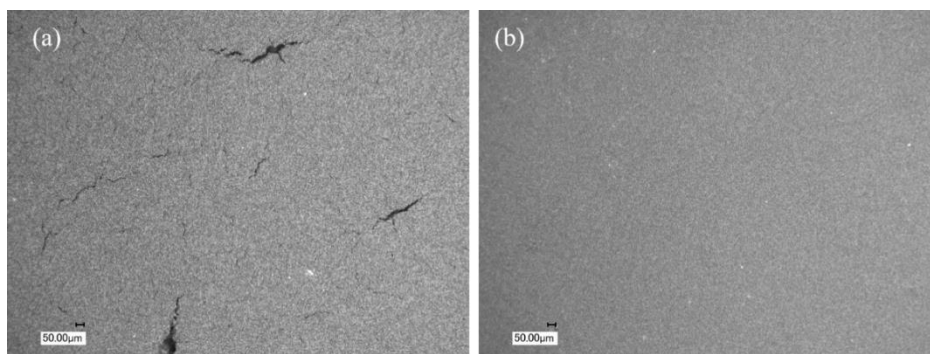
Figure 31: Optical microscope images of the slot die coating (areal mass loading 25.4 mg/cm^2) prepared with 10% IPA in H$_2$O as solvent *(a)* before calendering to ~40% porosity and *(b)* after calendering. The scale bar in all images is 50 µm.
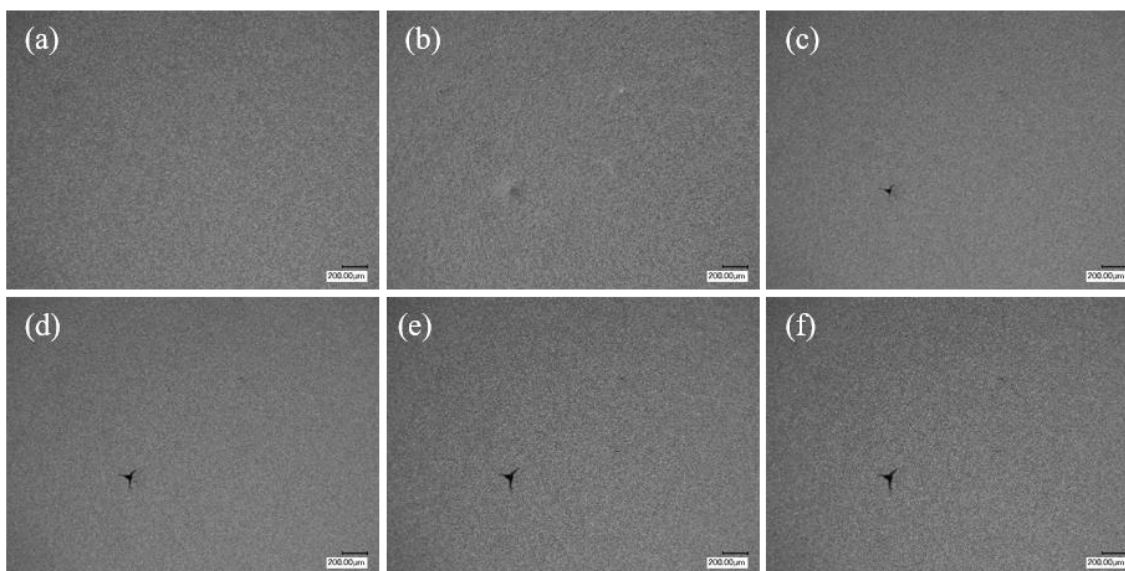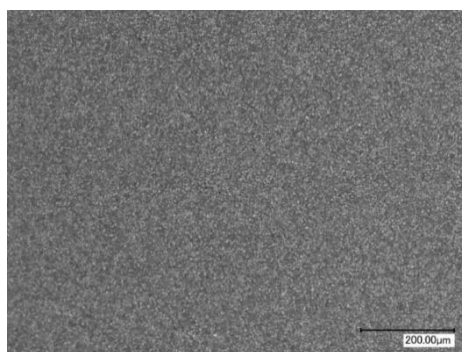

Figure 32: Optical microscope image of the slot die coating (areal mass loading 24.8 mg/cm^2) prepared with 20% IPA in H$_2$O as solvent before calendering.

Pouch cells assembled with electrodes from each coating were cycled at C-rates of C/5, C/3, C/2, 1C, 2C, and 3C. The thick NMC532 cathodes were paired with graphite anodes of a complementary thickness. Figure 33 shows the discharge voltage profiles of each pouch cell. The 10% IPA electrode performs satisfactorily for C-rates up to C/2. At C-rates above C/2 the deliverable capacity drops more than the 20% IPA electrode,

indicating higher internal resistance of the cell. The 20% IPA electrode performs very well over the range of C-rates tested. The large capacity loss of both electrodes for C-rates greater than 1C is a consequence of transport limitations within thick electrodes. [82] At relatively high C-rates, lithium ions in the electrolyte do not have the time to properly diffuse through the bulk of the electrode and concentration gradients develop, limiting the deliverable capacity to a fraction of the rated capacity.
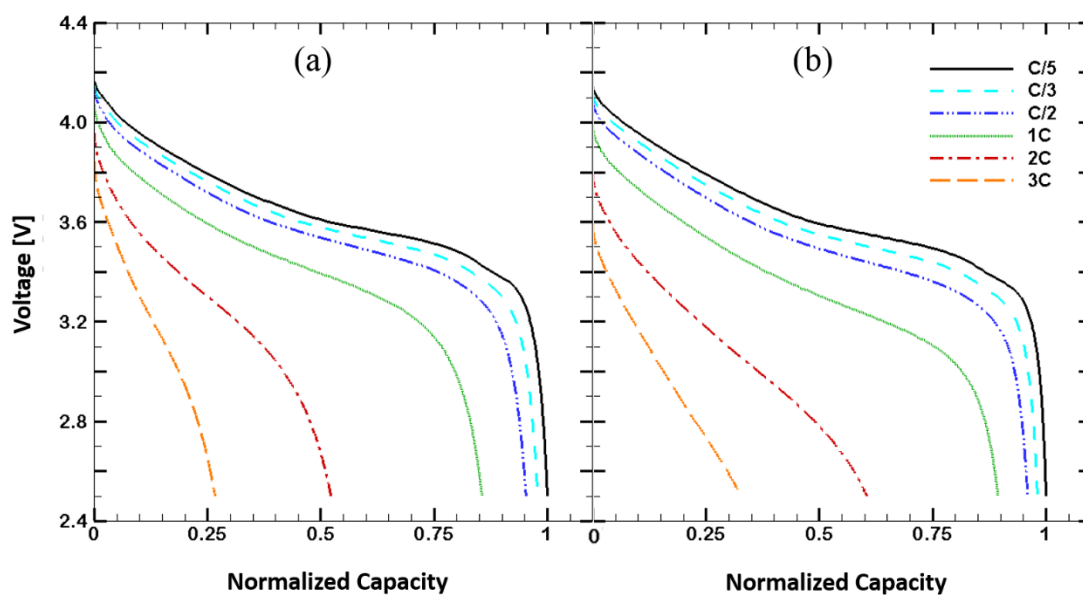
Figure 33: Discharge voltage profiles at different C-rates for pouch cells with NMC532 positive electrode prepared with *(a)* 10% IPA and *(b)* 20% IPA in H_2O as solvent.

The normalized capacity retention of each pouch cell versus discharge C-rate is presented in Figure 34. For comparison, the capacity retention of a cell with a thick positive electrode prepared with the conventional organic solvent, NMP, is included in Figure 34. The electrode of standard thickness (areal mass loading ~12 mg/cm^2) retains more than 70% of its deliverable capacity for C-rates up to 2C. As expected, capacity retention of all thick electrodes (areal loading ~25 mg/cm^2) drops sharply for high C-rates of 2C and 3C.

59

However, the capacity retention of the thick electrode prepared with 100% H_2O immediately begins to deteriorate at C-rates greater than C/3 – a consequence of the severe cracking in the electrode. The 10% IPA electrode shows markedly improved capacity retention from the cracked electrode. The 20% IPA electrode performs most comparably to the organically processed thick electrode, retaining more than 80% of its capacity at 1C.
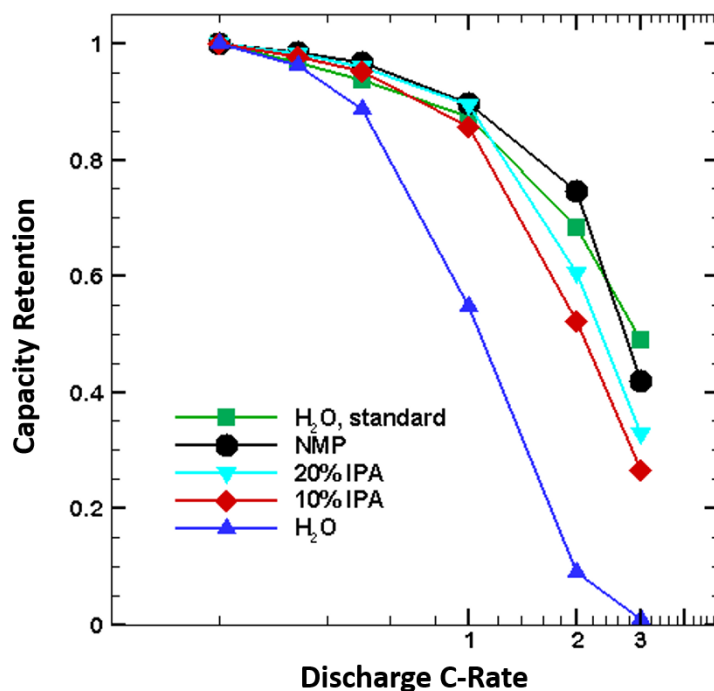
Figure 34: Capacity retention of each pouch cell at different C-rates, normalized to each cell's respective C/5 discharge capacity.

Figure 35 shows the cycling performance of each cell. The addition of IPA results in a striking improvement in cycling performance from that of the thick electrode prepared with only water as solvent. Comparing the 5th and 100th cycles, the 10% IPA electrode had a capacity retention of 96.4% and the 20% IPA electrode had a capacity retention of

97.3%. Both IPA electrodes achieve a cycling performance similar to the organically processed electrode which has a capacity retention of 97%.
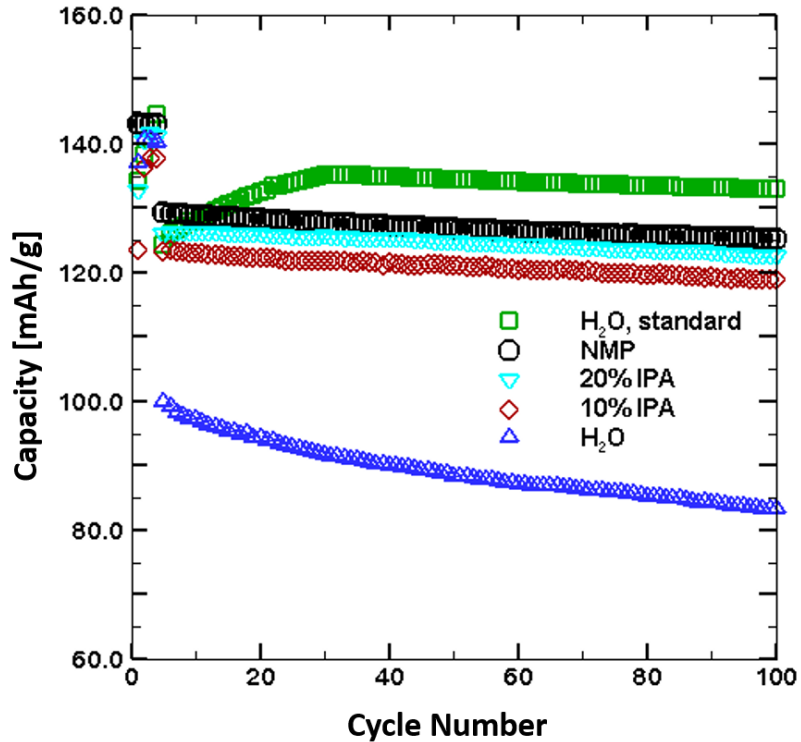
Figure 35: Cycling performance of pouch cells with various positive electrodes. The first four cycles were completed at C/20, followed by cycling at a rate of C/3.

III.4. Conclusion

From a theoretical analysis of cracking in thin films of hard particles, it is suggested that the critical crack-free film thickness scales inversely with the surface tension of the solvent. In an effort to enable aqueous processing of thick positive electrodes for high energy density LIBs, the solvent surface tension was reduced by adding IPA to water. The expected result was an increase in the critical thickness, allowing the fabrication of thick, crack-free aqueous processed electrodes.

An investigation of crack formations in NMC532 doctor blade coatings prepared with various compositions of IPA+ H_2O as solvent showed cracking improved as the wt. % of IPA in the solvent increased. Two industrial sized coatings, one prepared with 10 wt. % IPA and another with 20 wt. % IPA, were also investigated for cracks before their electrochemical performance was tested in full pouch cells with a graphite anode. Small cracks were evident in the coating with 10% IPA, but later cured by the force of calendering. Nonetheless, the increased internal resistance caused by interfacial resistance where cracked material had been reformed resulted in poor electrochemical performance, albeit still showing improvement from a thick electrode prepared with 100% H_2O. The coating prepared with a solvent containing 20% IPA was completely devoid of cracks, resulting in excellent electrochemical performance comparable to an organically processed positive electrode.

In conclusion, the addition of 20 wt. % IPA reduced the aqueous solvent surface tension from 72.8 mN/m to 32.3 mN/m, successfully increasing the critical thickness to enable aqueous processing of thick, crack-free positive electrodes for high energy density LIBs.

CHAPTER IV

INFLUENCE OF DRYING TEMPERATURE ON CRACKING IN LIB ELECTRODES

IV.1. Introduction

Electrode drying temperature is an important parameter in the fabrication of a high quality electrode, as evaporation rate strongly influences the final microstructure of an electrode. In turn, electrode microstructure dictates the eventual electrochemical performance of the electrode. The microstructure develops as a mixture of active material and conductive additive particles suspended in a solvent dry into a complex, porous microstructure held together by binder material. An LIB cathode performs best when these materials are uniformly distributed throughout the bulk. For this reason and more, the physics of drying particulate dispersions has been well studied in an effort to enable intelligent design of thin film microstructures for specialized applications, including LIB electrodes. [111-115]

The distribution of particles in a drying dispersion is influenced by evaporation, diffusion, and sedimentation. Initially, evaporation drives the free surface of the film towards the substrate at a constant velocity E. Depending on the rate of evaporation, particles may accumulate at the descending air-liquid interface and form a consolidation front. The resultant concentration gradient drives thermal Brownian diffusion of the particles that acts to redistribute particles uniformly. Moreover, the relative density of particles to surrounding solvent determines the rate of sedimentation, where particles sediment to the substrate under the force of gravity with velocity U. A diagram of each respective particle motion is presented in Figure 36.
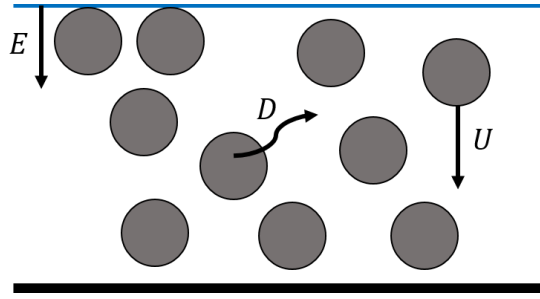
Figure 36: A schematic of particle motion, including evaporation (E), diffusion (D), and sedimentation (U), in a drying particulate dispersion.

The relative rates of evaporation, diffusion, and sedimentation determine the final microstructure of the film. For example, if the evaporation rate is much larger than the rate of diffusion, a significant consolidation front will form at the air-liquid interface. In a one particle system this phenomena is not necessarily disadvantageous, but may be so in a dispersion with multiple particles where concentration gradients are undesirable. A balance between evaporation, sedimentation, and diffusion will avoid the formation of concentration gradients.

The ratio of evaporation to diffusion is described by the dimensionless Peclet number:

$$P_e = \frac{Eh_o}{D_o} \tag{12}$$

Where h_o is the initial film thickness, E is the rate of evaporation, and D_o is the Stokes-Einstein diffusion coefficient for a spherical particle with radius R in a fluid with viscosity μ and temperature T. It is defined as:

$$D_o = \frac{kT}{6\pi\mu R} \tag{13}$$

where k is the Boltzmann constant. When evaporation is dominant $Pe >> 1$, and $Pe << 1$ for cases where diffusion is the dominant particle motion. For high Peclet numbers (i.e. high evaporation rate), the free surface descends faster than particles can diffuse and a

consolidation front forms at the air-liquid interface. The particle front continues to grow vertically until all particles are closely packed and liquid menisci form on surface particles. In contrast, for low Peclet numbers (ie. low evaporation rate), strong diffusion prevents the formation of concentration gradients.

Sedimentation is more common in films with a large initial height. A dimensionless sedimentation Peclet number describes the ratio of sedimentation to diffusion. Three distinct regions develop vertically in a drying film when sedimentation is the dominant particle motion. They include a particle free zone near the free surface, a region of sediment at the substrate, and a transition zone between these two regions where the particle volume fraction is equivalent to the initial particle volume. For high sedimentation Peclet number, sedimentation dominates and there is an abrupt boundary between sedimentation regions. For low sedimentation Peclet number, strong diffusion forms gradual transition zones between the three sedimentation regions. In the case of cathode dispersions, sedimentation is less prevalent as high particle concentration and binder material function to support large active materials and thus prevent sedimentation.

Based on the aforementioned dimensionless numbers, Cardinal et al. [114] developed drying regime maps to predict the dominant particle motion given a specific initial film thickness and evaporation rate. For high evaporation rates, the evaporation regime dominates and particles accumulate at the descending free surface. When the initial film thickness is high, the sedimentation regime dominates and particles accumulate at the substrate. The diffusion regime dominates for low evaporation rates. As such, drying at low evaporation rates is often interpreted as progressing through a series of equilibrium states. [115] The drying regime maps developed by Cardinal et al. also reveal that for dispersions with higher initial volume fractions hydrodynamic and particle interactions increase so lower evaporation rates are required to form a consolidation front of particles at the free surface. Furthermore, a consolidation front forms at lower evaporation rates for particles with larger radii because diffusion rate decreases for large particles.

Though much is known about the effect of evaporation rate on the formation of a film's microstructure, its influence on crack formation is less understood. Lee et al. [116] developed a scaling relationship for crack spacing relative to evaporation rate based on experimental observations of cracking in a number of dispersions ranging in particle volume fraction, evaporation rate, film height, and particle radius. In all cases, hard particles were used which do not form a coherent film, similar to an electrode slurry. The scaling relationship was derived from a proposed cracking mechanism described by Lee et al. in which negative capillary pressure drives the formation of cracks. Specifically, a reduction in available volume due to a crack eliminates the local capillary pressure. The resultant pressure gradient then causes solvent to flow towards regions of low pressure in the film bulk. Lee et al. propose the horizontal distance of this flow dictates crack spacing and derive an estimation for the relevant hydrodynamic length scale.

Plotting experimental data of crack spacing, normalized by the hydrodynamic length scale, versus a similarly non-dimensionalized capillary pressure revealed an interesting trend. Despite the range of parameters in their experimental dispersions, Lee et al. found the data collapsed to one curve, and from here concluded the following scaling relationship:

$$\frac{y}{X} \sim \frac{h_f^{0.8} R^{0.2}}{E^{0.35}} \tag{14}$$

where y is the crack spacing, X is the hydrodynamic length scale, h_f is the dried film height, R is the particle radius, and E is the evaporation rate. Then according to this relationship, areal crack density is expected to increase for increasing evaporation rate as spacing between cracks narrows.

It is hypothesized that cracking in thick, aqueous LIB cathode coatings will scale with evaporation rate in a similar manner as Equation 14. To investigate the relationship between evaporation rate and crack formation, an aqueous electrode processing procedure which utilizes a novel hydrophilic binder was first developed. Electrodes ranging from standard thickness to double thickness were fabricated and dried at temperatures of 20, 45, and 70 °C. Electrodes dried at room temperature (20 °C) provided a baseline to which

those dried at higher temperatures could be compared. Each electrode coating was analyzed via scanning electron microscopy (SEM). Image processing of SEM images was employed to quantify cracking in the form of crack severity, distribution of crack length, and distribution of average crack width.

IV.2. Experimental Methods

Aqueous cathode slurry composed of the active material $LiNi_{0.3}Mn_{0.3}Co_{0.3}O_2$ (NMC333, Targray), carbon black (Super C45, Timcal), and binder was prepared in the wt. % ratio 90:5:5, respectively. Binder was a combination of sodium carboxymethyl cellulose (CMC, Aldrich) and modified styrene-butadiene copolymer (PSBR100, Targray) in a 1:4 wt. % ratio. A solution of 2 wt. % CMC dissolved in water was prepared in advance via magnetic stirring for 24 hours. PSBR in the form of an aqueous emulsion with 15% solid content was added to the slurry as received. CMC in combination with a hydrophilic polymeric binder such as PSBR is known to produce a slurry with the rheological properties necessary for quality coating, while also achieving excellent cohesion of electrode powders and adhesion to the current collector. Styrene-butadiene rubber (SBR) is a ubiquitous binder in aqueous processing for anodes, [55, 71, 73, 84, 117] but its complex interaction with cathode particles has prevented its standardized use in aqueous processed cathodes. Specifically, researchers have reported cathode morphology and electrochemical properties are seriously dependent on the CMC:SBR ratio, and no one ideal ratio exits which minimizes disadvantages. [118] However, Targray [119] has claimed that by polymerizing SBR to form what they refer to as PSBR, they have created a polymeric binder applicable to both anode and cathode chemistries that still preserves the positive aspects of SBR as an aqueous binder. They report a LIB cathode made with PSBR is capable of providing its full capacity when compared to an organically processed cathode. Despite this, a literature review indicated PSBR has yet to be introduced as a hydrophilic binder in LIBs. Rather, its use in published studies has been limited to cathode ink for flexographically printed zinc battery cathodes [120], lithium-sulfur batteries [121], and electrodes for wearable technologies [122, 123].

To make the cathode slurry, water was first mixed with the premade CMC solution in a glass vial using a magnetic stirrer (brand, Figure 37). Dry mixing of NMC333 and carbon black was done with a mortar and pestle (Figure 38). The powders were then added to the glass vial and the slurry was mixed for 8 hours. PSBR was added to the slurry last, followed by 12 additional hours of mixing.
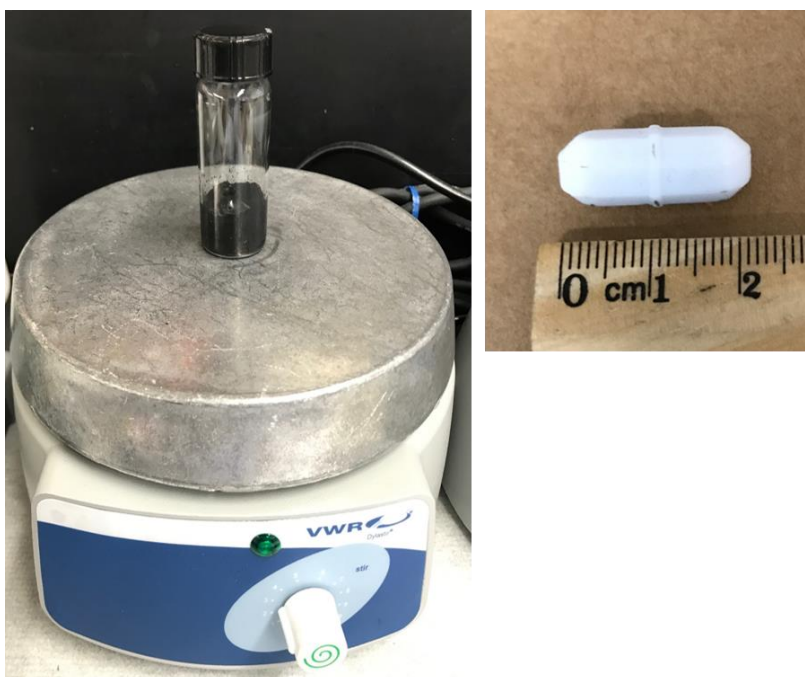
Figure 37: Glass vial with slurry atop the magnetic stirring platform *(left)* and magnetic stirring bar *(right)* used to mix the aqueous cathode slurry.
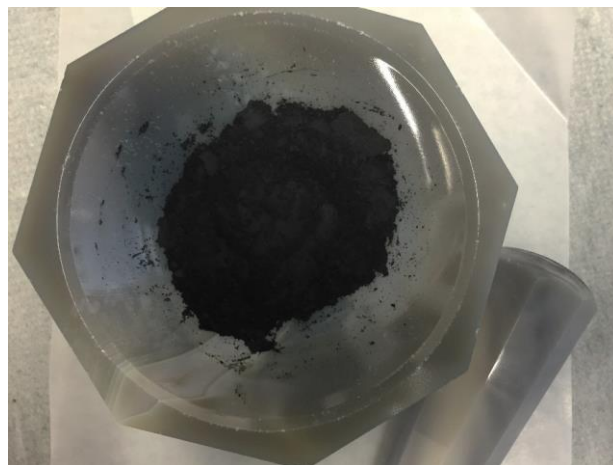
Figure 38: NMC333 and carbon blacked mixed with a mortar and pestle.

The aqueous cathode slurry was coated on an aluminum foil substrate using a doctor blade in combination with an automatic film applicator (Elcometer 4340, Figure 39). Before coating the slurry, the aluminum foil was cleaned with acetone and a scouring pad to (a) remove a thin layer of oil put in place by the manufacturer to prevent the roll of aluminum foil from sticking to itself and (b) roughen the surface. Pretreating the aluminum foil in this way promotes better adhesion between the substrate and the aqueous cathode dispersion.

Figure 39: Automatic film applicator and doctor blade for coating slurry on a substrate.

Electrodes of standard thickness (areal mass loading of ~11 mg/cm^2), intermediate thickness (~15 mg/cm^2), and double thickness (~23 mg/cm^2) were coated and allowed to dry at room temperature (~20 °C), 45 °C, and 70 °C. Drying at elevated temperatures was carried out in a vacuum oven (MTI, DZF-6020-FP, Figure 40). The mass of each electrode coating was measured every five minutes throughout the drying process. The resultant water content profile was then fit to a curve. All curve fitting was performed in Tecplot 360 and accomplished by the method of weighted least squares fitting. The constant evaporation rate characteristic of the first drying regime was found by fitting the acquired water mass versus time data to a first degree polynomial:

$$m_w(t) = -Bt + C \tag{15}$$

where m_w is the water mass in milligrams, t is time in minutes, B is the constant rate of evaporation, and C is a constant. In this case, the evaporation rate is reported in milligrams of water per minute. Since the volume of evaporated water is directly proportional to the reduction in film height during this first drying phase of constant evaporation, evaporation rate is more conveniently reported in units of length per minute. Equation 16 was used to convert the evaporation rate from milligrams of water per minute to microns per minute:

$$E = \frac{B}{\rho_w A} \tag{16}$$

where ρ_w is the density of water and A is the surface area of the electrode coating. The duration of the first drying phase (Δt_1) was then calculated from the known initial wet film height (h_o) and measured final dry film height (h_f):

$$\Delta t_1 = \frac{h_o - h_f}{E} \tag{17}$$

The remainder of the water content profiles corresponded to the second drying regime where evaporation rate is no longer constant, and was therefore fit to an exponential functional:

$$m_w(t) = De^{-t/\tau} \tag{18}$$

where τ is the exponential time constant and D is a constant. The time constant is an interesting parameter in that it provides insight into the time scale of the second drying phase where the air-liquid interface has receded into the particle network.
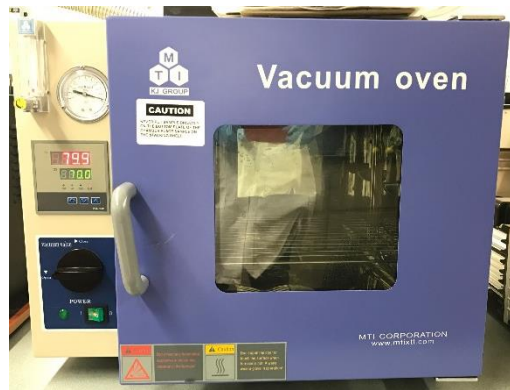
Figure 40: Vacuum oven used to dry electrode coatings at elevate temperatures.

After drying, a scanning electron microscope (SEM, Vega, info) was used to analyze crack formation in each electrode. Images were taken at a low magnification (25X-42X) and high magnification (75X). Each high magnification SEM image was digitally analyzed to determine the crack severity, crack length distribution, and crack width distribution for each electrode thickness at each drying temperature. Crack severity, better known as crack intensity factor (CIF), is a common parameter used to quantify cracking in desiccating soils [124-126]. SEM image processing was carried out in Matlab. The process began by first converting the original gray scale SEM image to binary by segmenting the image based on a predetermined threshold. A threshold function [127] which allows the user to

manually select the upper and lower threshold bounds, then preview the output binary image was employed to determine the proper threshold value for the SEM images. The lower and upper threshold bounds were set to 0 and 100, respectively, as this was found suitable for all images regardless of electrode thickness or drying temperature. Pixel values in the gray scale image ranged from 0 to 255. In converting the gray scale image to binary, pixels with a value greater than 100 were given a value of 0 (black) and pixels with a value less than 100 were given a value of 1 (white) in the output binary image.

Unmodified binary SEM images inherently included a lot of noise. In addition, conversion to a binary image resulted in void spaces in some cracks – narrow cracks with a width of only a few pixels were specifically vulnerable to this distortion. Consequently, one crack in the gray scale image would be incorrectly interpreted as two cracks in the binary image. To resolve these conversion issues, the binary image was subjected to a morphological filtering technique known as closing. The process of closing involves object dilation followed by erosion.

Closing first requires the definition of a structuring element. In this case, a 3x3 square structuring element was selected. By default, Matlab gives the nine pixels of the structuring element a value of 1. The structuring element is "laid over" the input image (ie. the unmodified binary image) with the center pixel coincident with the pixel of interest in the input image. As the structuring element is moved over the entire input image, each pixel of the input image will serve as the central pixel of the structuring element exactly once. The structuring element is said to "fit" the input image if *all* of the corresponding input pixels below the structuring element also have a value of 1. On the contrary, if at least one of the input image pixels below the structuring element have a value of one, the structuring element is said to "intersect" the input image. An example of the structuring element over an input image is shown if Figure 41. Once the structuring element is determined to fit or intersect the input image, the operations of erosion and dilation define the subsequent action on the central pixel and the result is output to a modified binary image.
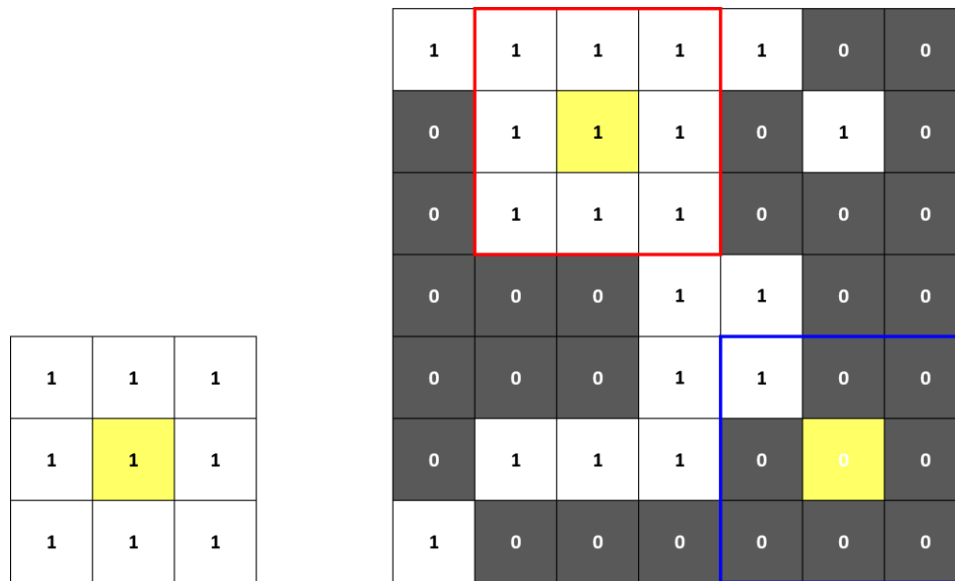
Figure 41: *The 3x3 structuring element (left) lays over the binary input image (right).* The red square outlines an instance when the structuring element fits the input image, whereas the blue square outlines the structuring element intersecting the input image. The pixel of interest is yellow.

As previously mentioned, closing involves first dilating the binary image. During dilation, if the structuring element intersects the input image (ie. one or more underlying input pixels has a value of 1) the input pixel corresponding to the central pixel of the structuring element is given a value of 1 in the output image, otherwise it will be zero. In effect, dilation by a 3x3 structuring element adds a layer of pixels to the boundary of each object in the binary image. The operation then closes gaps less than or equal to two pixels wide. Each pixel in the SEM images is equivalent to 3.61 μm. Therefore, a 3x3 structuring element was chosen so adjacent cracks with a gap width less than the average diameter of an NMC particle (~10 μm) would be filled.

Besides filling void spaces in cracks, dilation also amplifies noise in the binary image. To filter noise as well as restore cracks to their true dimensions, erosion is applied to the dilated binary image. During erosion, the same structuring element is passed over the

entire image. If the structuring element fits the dilated binary image (ie. all input pixels lying below the structuring element have a value of 1) the central pixel is given a value of 1 in the output image. As a result, erosion shrinks the dimension of all connected objects by removing one layer of pixels from the boundary. The advantage of erosion is that small connected objects corresponding to noise in the binary image will be completely omitted from the output image when the structuring element fails to fit in the object for any of its pixels.

The closed binary image is subjected to one last image processing technique to remove noise large enough to evade the process of erosion. This involves removing connected objects of 97 pixels or less from the closed binary image. Such objects are accredited to errors in electrode preparation due to laboratory equipment limitations. This effect was accounted for by first analyzing SEM images of electrodes of standard thickness dried at room temperature. After morphologically filtering these images via closing procedure, the average area (in pixels) of the remaining connected objects was determined and set as the threshold value of 97 pixels in the final filtration step for all subsequent SEM image analysis. The procedure successfully eliminated the influence of processing errors on crack analysis. The result was a clean binary image comprised of only the electrode crack formations caused by increased thickness and evaporation rate.

With image analysis complete on SEM images, the boundary of each crack was determined. The distance between boundary pixels was calculated to find the maximum distance. Once the two boundary pixels furthest from each other were identified, the boundary pixels connecting them were counted – providing the length of the crack. The area of each crack was determined by a built in Matlab function known as *regionprops*. The area was divided by the length to determine the average width of each crack. Furthermore, white pixels were summed and divided by the total number of pixels in the image to evaluate the CIF. The entire image analysis and crack quantification procedure was carried out for nine electrode samples (three thicknesses at three drying temperatures), with three SEM images taken from each of the nine samples. The probability density function of a normal distribution of crack length and crack width was plotted for each

electrode sample based on the image analysis results to determine the effect of drying temperature on crack formation in aqueous processed electrodes.

IV.3. Results and Discussion

IV.3.1. Quantification of Cracking by Image Processing

Electrodes of ~11, 15, and 23 mg/cm^2 were coated and dried at 20, 45, or 70 °C. For reference, Table 3 presents the precise wet and dry thicknesses, as well as the areal mass loading of each aqueous electrode coating considered in the following image analysis. The surface of each electrode (and subsequent crack formations) is presented in Figure 42 through Figure 44, which show SEM images taken at low magnification. The images provide clear qualitative evidence that the severity of cracking worsens with increasing mass loading, as well as increasing drying temperature. The observed correlation between increasing mass loading and crack severity is in agreement with previous reports, though no such experimentally observed correlation with drying temperature has been reported in literature. [84, 128] Interestingly, holes are evident in electrodes dried at higher temperatures regardless of thickness, and the areal density of holes increases with electrode thickness. On the contrary, electrodes dried at room temperature (Figure 42) are free from any holes, implying an increase in drying temperature effects the evolution of the electrode microstructure in a detrimental way.

Table 3: Dimensions of electrode coatings used in image processing for crack quantification.

T_{dry} [°C]	Wet Thickness [μm]	Dry Thickness [μm]	Areal Mass Loading [mg/cm^2]
20	200	78 ± 10.3	10.3 ± 0.5
	350	102 ± 3.6	15.6 ± 0.7
	400	138 ± 9.5	23.3 ± 2.0
45	200	81 ± 1.2	10.9 ± 0.1
	300	105 ± 1.0	16 ± 0.3
	400	138 ± 3.2	22 ± 1.3
70	200	86 ± 5.1	11.2 ± 2.0
	300	113 ± 13.6	15.8 ± 1.4
	400	167 ± 3.2	23.0 ± 2.2
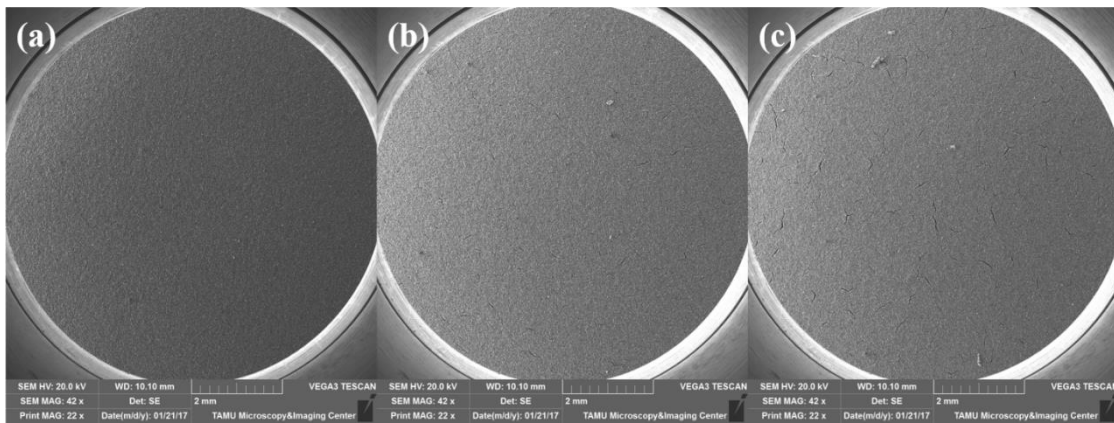
Figure 42: 25X SEM image of an electrode dried at 20 °C with areal mass loading *(a)* 11 mg/cm^2, *(b)* 15 mg/cm^2, and *(c)* 23 mg/cm^2. The scale bar in all images is 2 mm.
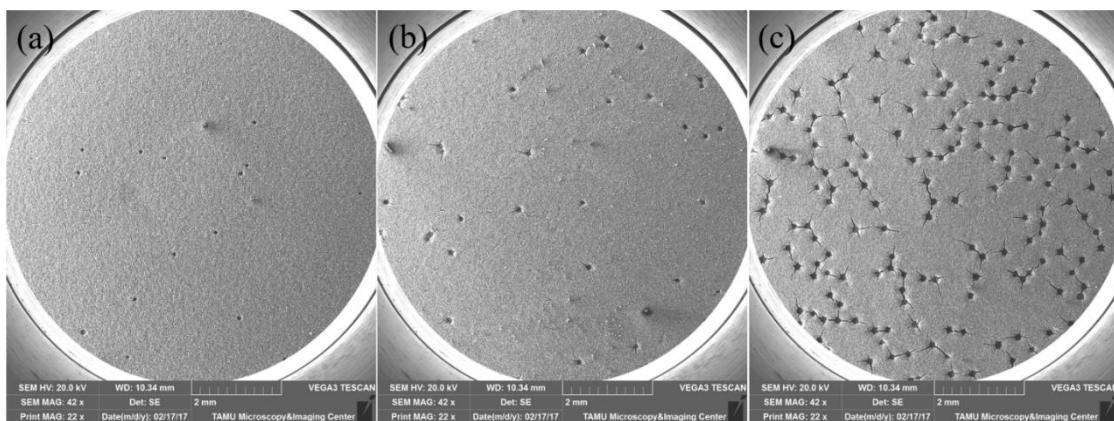
Figure 43: 25X SEM image of an electrode dried at 45 °C with areal mass loading *(a)* 11 mg/cm², *(b)* 15 mg/cm², and *(c)* 23 mg/cm². The scale bar in all images is 2 mm.
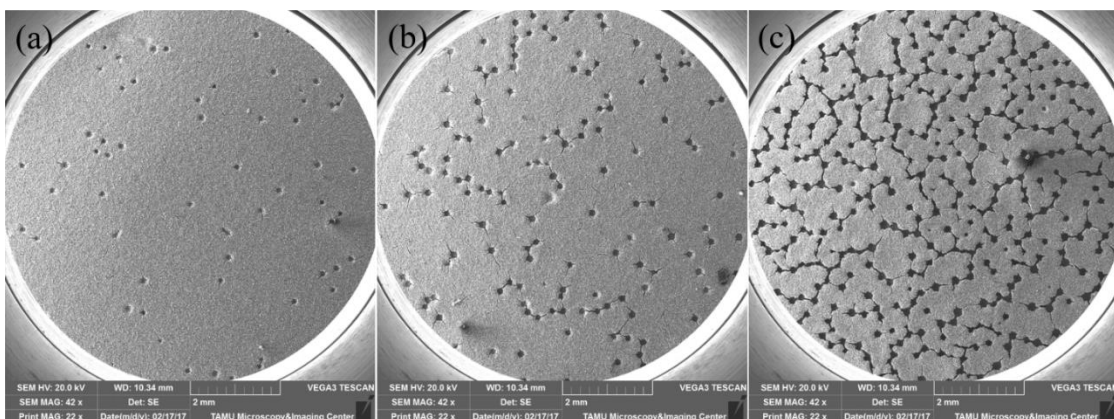
Figure 44: 25X SEM image of an electrode dried at 70 °C with areal mass loading *(a)* 11 mg/cm², *(b)* 15 mg/cm², and *(c)* 23 mg/cm². The scale bar in all images is 2 mm.

SEM images taken at a higher magnification are presented in Figure 45 through Figure 47. At this magnification, the detailed crack pattern is more easily observed. Hairline cracks can even be seen in the standard size electrode dried at 20 °C. This observation disagrees with the well-established understanding that aqueous processed electrodes of standard thickness are crack-free. [42, 58, 60, 64, 84, 128] Given that slurries in this research were prepared via magnetic stirrer rather than a reliable high shear mixer, minor

cracking seen in Figure 45 (a) was attributed to processing faults. As previously discussed, this phenomenon was taken into account in the image analysis procedure.
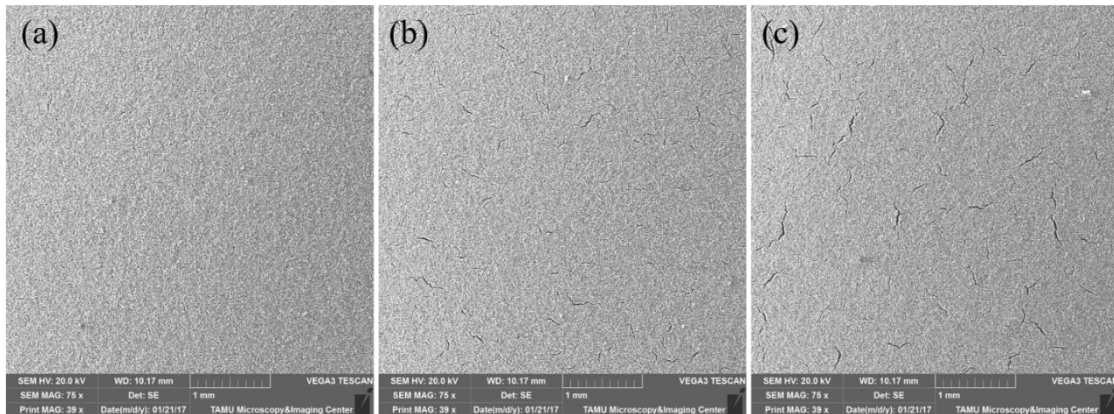
Figure 45: 75X SEM image of an electrode dried at 20 °C with areal mass loading *(a)* 11 mg/cm^2, *(b)* 15 mg/cm^2, and *(c)* 23 mg/cm^2. The scale bar in all images is 1 mm.
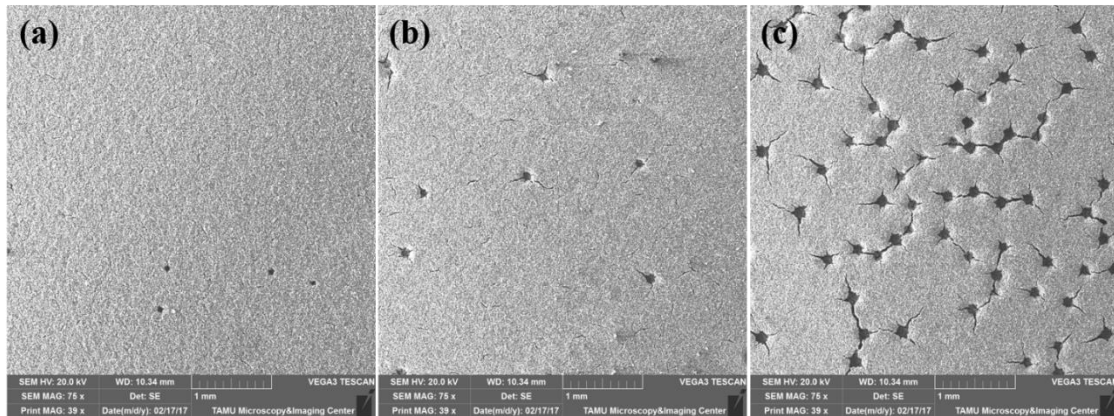
Figure 46: 75X SEM image of an electrode dried at 45 °C with areal mass loading *(a)* 11 mg/cm^2, *(b)* 15 mg/cm^2, and *(c)* 23 mg/cm^2. The scale bar in all images is 1 mm.
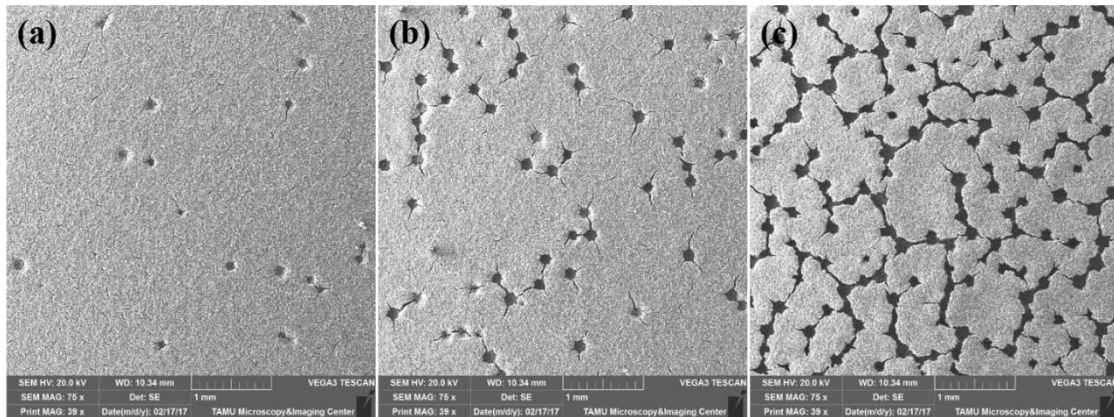
Figure 47: 75X SEM image of an electrode dried at 70 °C with areal mass loading *(a)* 11 mg/cm^2, *(b)* 15 mg/cm^2, and *(c)* 23 mg/cm^2. The scale bar in all images is 1 mm.

Image processing was performed on the SEM images in Figure 45 through Figure 47 to quantify cracking. Figure 48 through Figure 50 show the post-processing filtered binary images. For comparison, original gray scale images are also presented in Figure 48 through Figure 49. The boundary of cracks identified by the image analysis procedure are superimposed on to the respective gray scale images. Processing induced cracks in the standard thickness electrode dried at 20 °C have been filtered out so that Figure 48 (a) shows a crack-free, uniform electrode surface. In Figure 49 (e) agglomerates caused by slurry preparation difficulties were edited out of the original gray scale image as shadows surrounding the agglomerates resulted in them being misidentified as cracks during image processing. In general, SEM images were free from such processing defects and image processing proceeded without modifications to the original gray scale images.
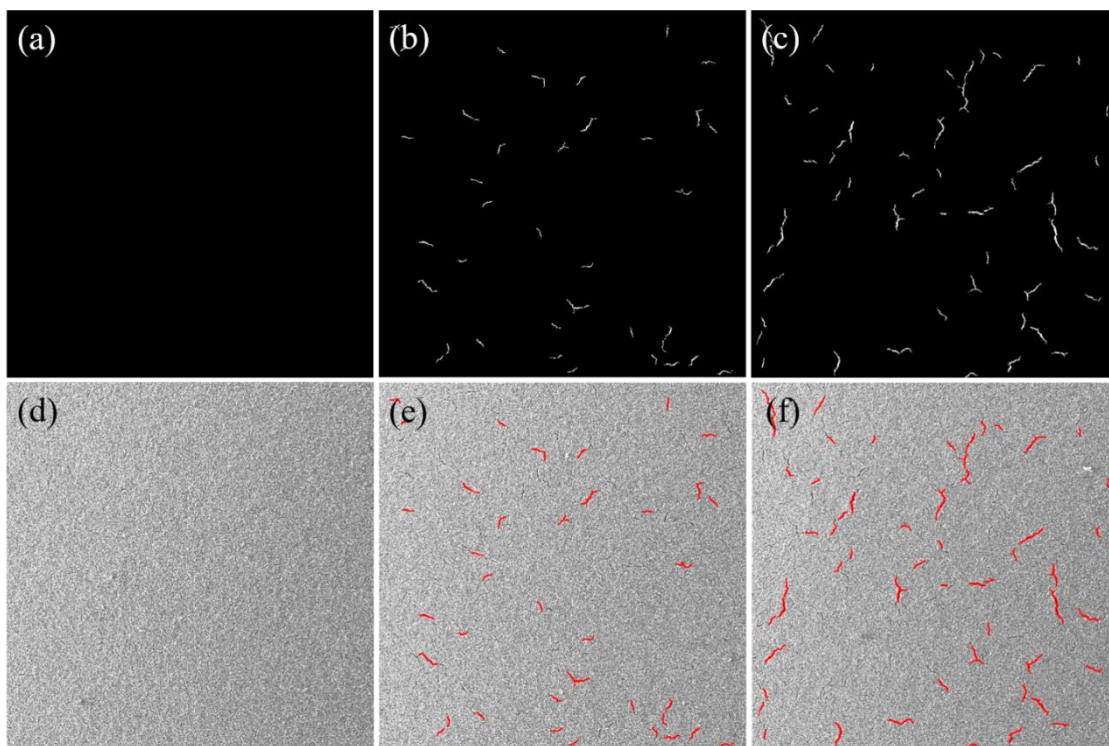
Figure 48: Binary image and original gray scale image of an electrode with mass loading *(a, d)* 11 mg/cm², *(b, e)* 15 mg/cm², and *(c, f)* 23 mg/cm². Boundaries of cracks present in the binary image are superimposed on the original gray scale image. All electrodes were dried at 20 °C.
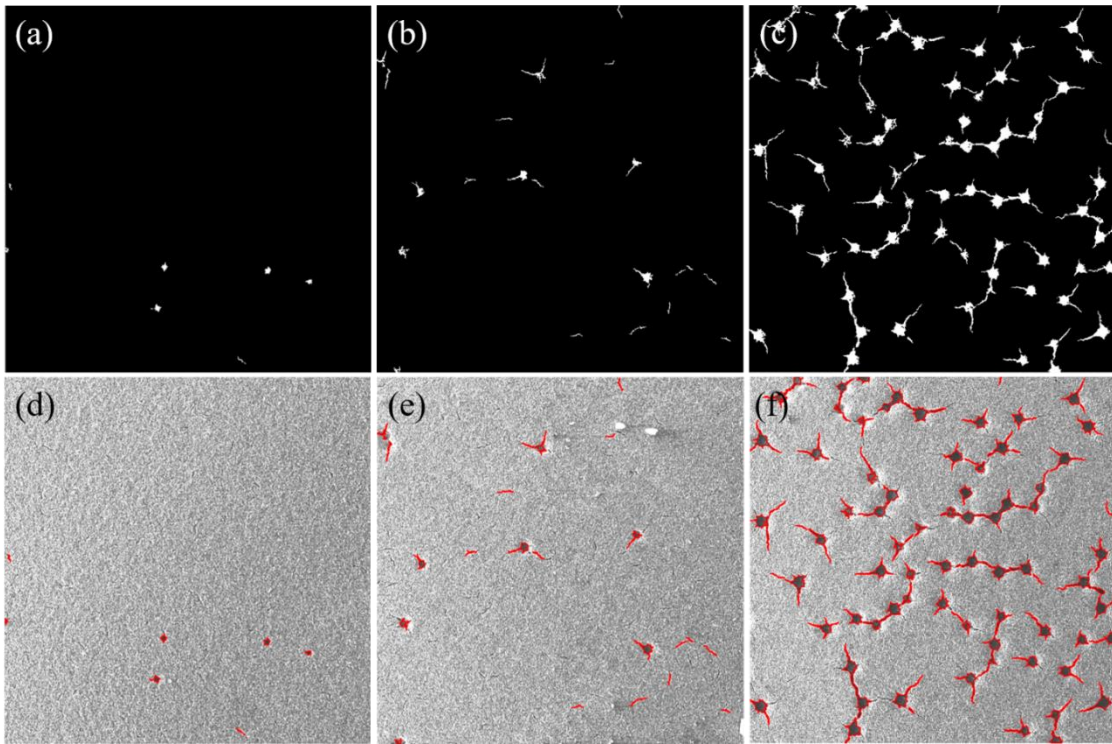
Figure 49: Binary image and original gray scale image of an electrode with mass loading *(a, d)* 11 mg/cm², *(b, e)* 15 mg/cm², and *(c, f)* 23 mg/cm². Boundaries of cracks present in the binary image are superimposed on the original gray scale image. All electrodes were dried at 45 °C.
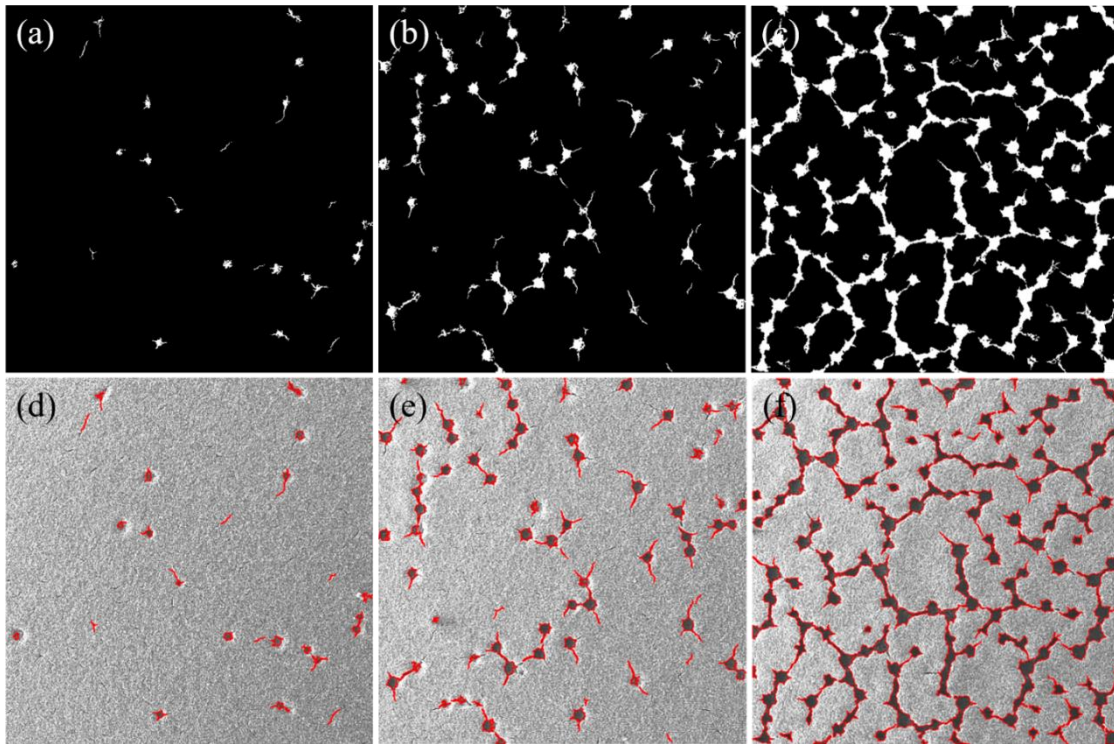
Figure 50: Binary image and original gray scale image of an electrode with mass loading *(a, d)* 11 mg/cm², *(b, e)* 15 mg/cm², and *(c, f)* 23 mg/cm². Boundaries of cracks present in the binary image are superimposed on the original gray scale image. All electrodes were dried at 70 °C.

Crack dimensions obtained from digitally processing SEM images of cracking are presented in Figure 51. With the exception of Figure 51 (b), the results reveal a higher drying temperature leads to longer and wider cracks. Moreover, the distribution of crack lengths and widths widens as the drying temperature increases. In the case of a 23 mg/cm² electrode dried at 70 °C (Figure 51 (e)) only a subtle peak is evident in the crack distribution. The distribution of crack length and width likely widens for higher drying temperatures as a result of the holes observed in these electrodes. Holes are absent from electrode coatings dried at 20 °C, thus the length and width of cracks are confined to a narrow distribution.
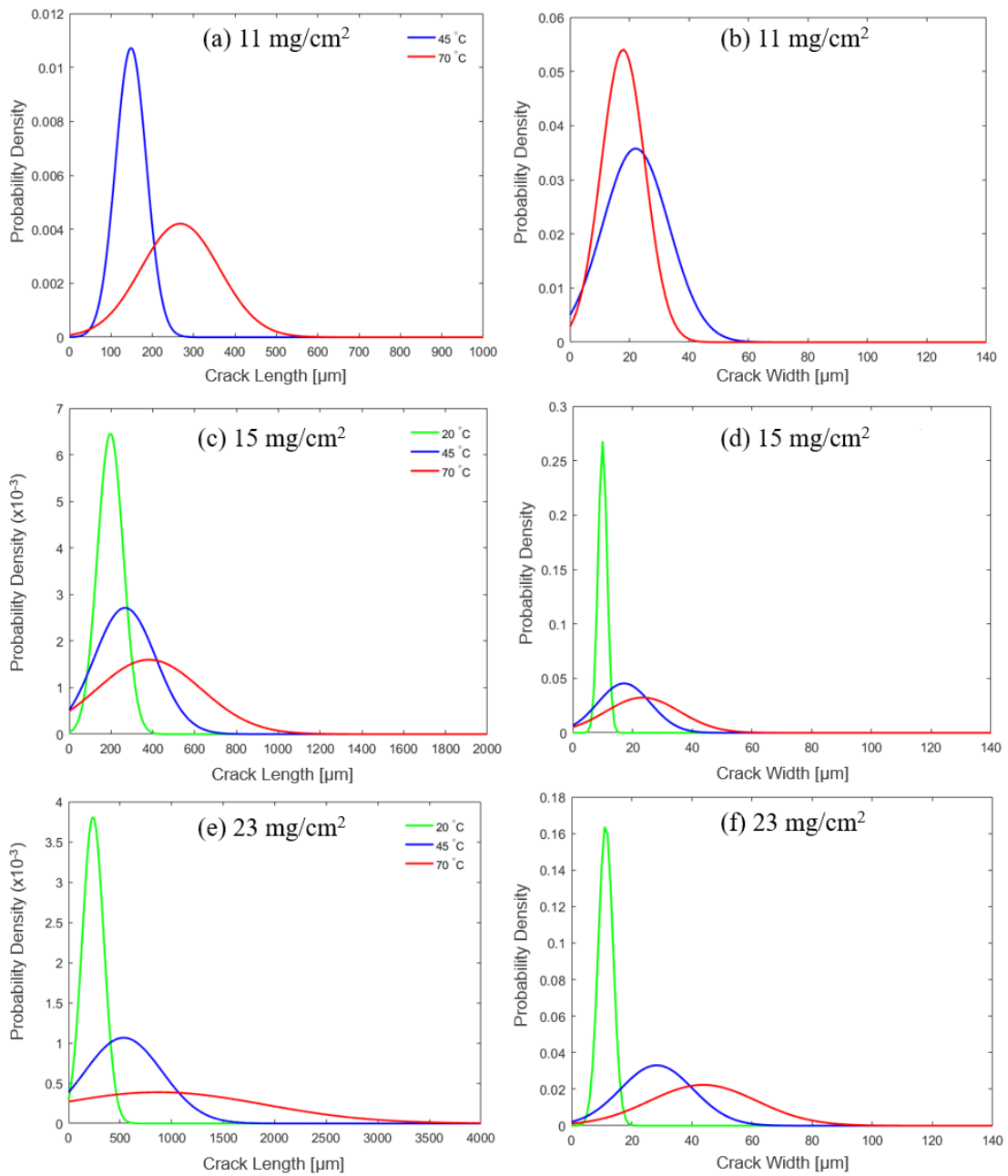
Figure 51: Distribution of crack lengths and widths observed in aqueous electrode coatings with areal mass loadings of *(a, b)* 11 mg/cm², *(c, d)* 15 mg/cm², and *(e, f)* 23 mg/cm² dried at 20, 45, and 70 °C.

The crack intensity factor (CIF) of each electrode is presented graphically in Figure 52. There is a modest increase in the percentage of surface area covered by cracks for electrodes with areal mass loadings of 11 and 15 mg/cm^2, increasing from 0% to 0.62% and 0.31% to 3.3%, respectively. However, the CIF of thick electrodes (23 mg/cm^2) dramatically rises with increasing drying temperature – from 0.682% when dried at room temperature to 15.1% when dried at 70 °C.
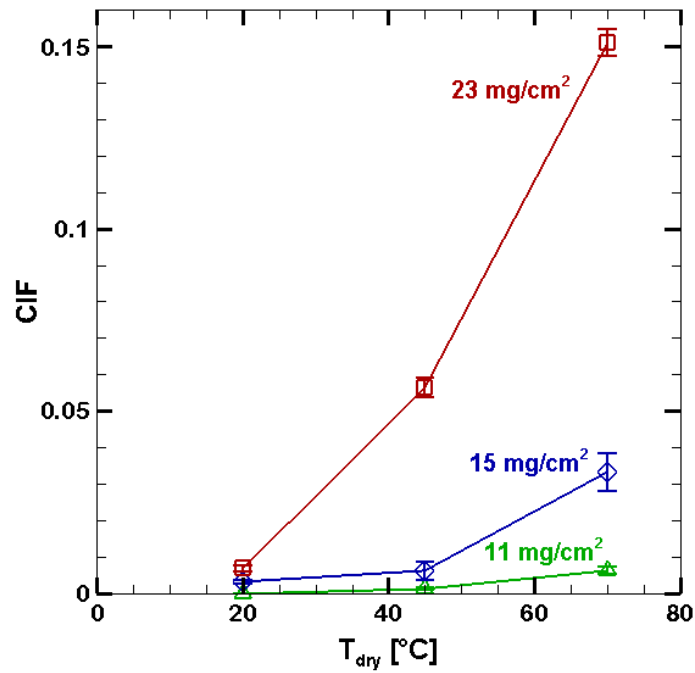
Figure 52: Crack intensity factor (CIF) for each electrode dried at various temperatures. CIF represents the fraction of total surface area that is covered in cracks.

The worsening crack severity with increasing drying temperature can be attributed to the formation of holes during drying at high temperatures. Flaws, such as holes, are known to promote cracking and serve as nucleation sites for cracks in a thin film. [110] The process of crack formation initializes at the moment mounting capillary pressure overcomes the adhesion strength between the air-liquid interface and surface particles, and air invades

the particle network. With air having penetrated the particle network, the film experiences in-plane capillary forces that propagate cracks. Adhesion strength between the air-liquid interface and surface particles is weakest at large pores, so cracks will nucleate at large pores first. Holes in the electrodes dried at elevated temperatures are extremely large pores relative to the close packed particle network, and thus serve as nucleation sites for cracking. Moreover, as the SEM images show (Figure 46 and Figure 47), the areal density of holes increases with increasing electrode thickness and drying temperature. As a result, holes promote severe crack formations that dominate the electrode surface area as cracks propagating from closely packed holes are more likely to intersect one another

IV.3.2 Evaporation Rate and Water Content Profiles of Drying Electrodes

The mass of each electrode taken at regular intervals throughout the drying process are presented in Figure 53 in the form of water content profiles, each of which has been normalized relative to the initial water mass of each electrode. The symbols in Figure 53 represent the actual measurements. It should be noted that measurements inherently include some error – electrodes dried at room temperature are subject to temperature and air flow fluctuations, whereas accurate mass data for electrodes dried at higher temperatures proved difficult owing to the rapidly changing coating mass. Moreover, electrodes dried at elevated temperatures had to be removed from the vacuum oven and transferred to ambient conditions to collect mass data every five minutes.
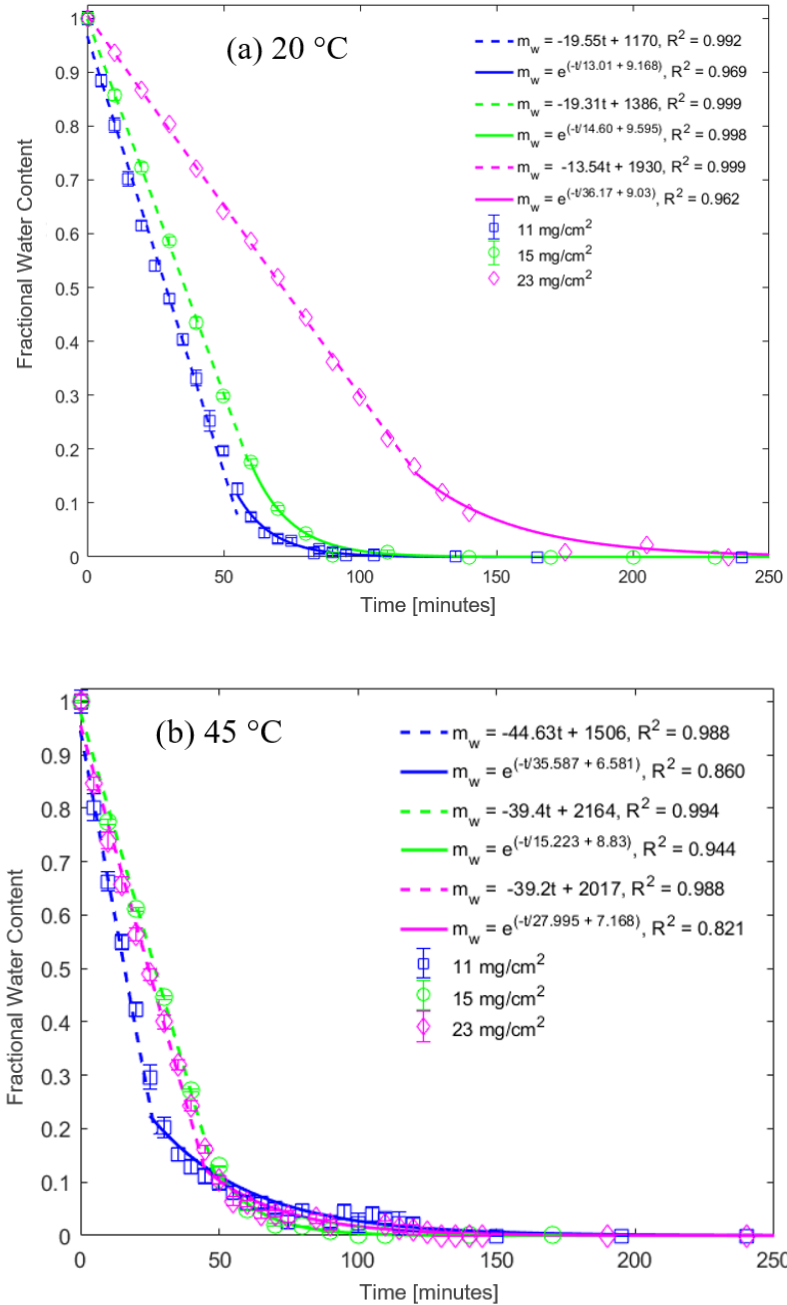
Figure 53: Water content profiles of drying electrodes of various thicknesses dried at *(a)* 20 °C, *(b)* 45 °C, and *(c)* 70 °C, normalized with each electrode's initial water mass. Linear functions have been fit to the first portion of each water content profile, while exponential functions have been fit to the last portion to describe the first and second drying phase, respectively.
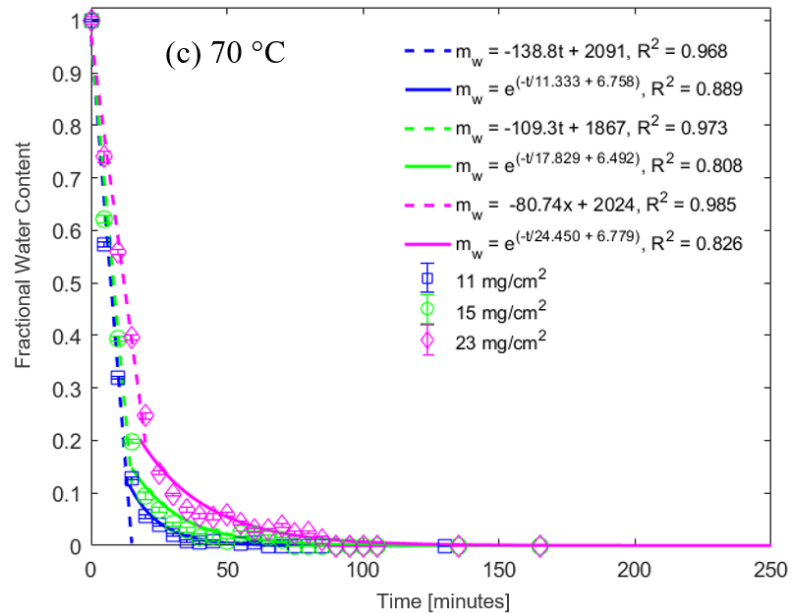
Figure 53: Continued.

Despite inherent errors in intermittent mass data collection, Figure 53 shows general trends expected for drying particulate dispersions. First, water content quickly declines for electrodes dried at higher temperatures, and the rate of water loss is slower for thicker electrodes. Also, the first and second drying phases can be observed in each water content profile. The first drying phase is marked by the linear reduction in water mass as a constant evaporation rate drives the air-liquid interface and particles towards the substrate until vertical consolidation is no longer possible. This phase is denoted by a dashed line in Figure 53. Linear curves were fit to this portion of the water content profiles corresponding to the first drying phase to determine the rate of evaporation. Evaporation rates (E), averaged from the three electrodes, are presented in Table 4 for each drying temperature. From the known initial and final film thicknesses, an estimation of the total time duration of the first drying phase (Δt_1) was calculated based on the evaporation rate obtained from curve fitting; results are also presented in Figure 54. The time duration of the first drying phase agrees well with the data in Figure 53. Moreover, electrode thickness and drying

87

time (during period of constant evaporation) strongly correlate; doubling electrode thickness from 11 mg/cm^2 to 23 mg/cm^2 causes drying time to also double in all cases.

Table 4: Evaporation rate obtained from the linear functions fit to water content profiles.

T_{dry} [°C]	E [µm/min]
20	1.99 $\pm$ 0.14
45	4.16 $\pm$ 0.80
70	10.49 $\pm$ 0.79
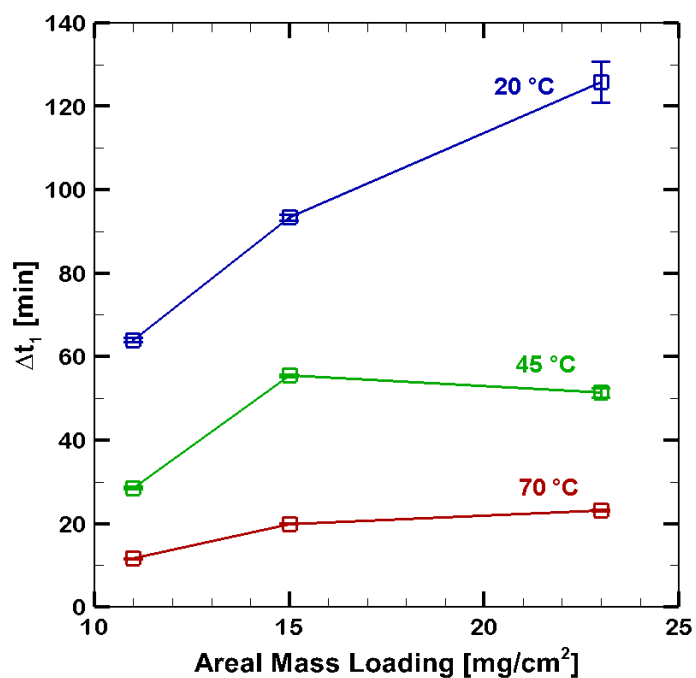
Figure 54: Total time duration of the first drying phase for electrodes of various thickness dried at 20, 45, and 70 °C.

The second drying phase is denoted by a solid line superimposed on the data in Figure 53. At this point in the drying process, mounting capillary pressures force the air-liquid interface to recede in the bulk of the particle network. Evaporation is then limited by the transport of water vapor through pores from the electrode bulk, and thus no longer constant. The portion of the water content profiles in Figure 53 corresponding to this phase of drying were fit to exponential curves. As displayed in each plot of Figure 53, R^2 values of exponential fits were good in all cases, indicating water content decreases exponentially in the second drying phase. The time constant of exponential decay is presented in Table 5. As expected, thicker electrodes have a greater time constant, though the time constant is less dependent on drying temperature.

Table 5: Time constant of exponential function fit to the portion of each water content profile corresponding to the second drying phase.

T_{dry} [°C]	Mass Loading [mg/cm^2]	τ [min]
20	11	13.014
	15	14.603
	23	36.166
45	11	35.587
	15	15.223
	23	27.995
70	11	11.333
	15	17.829
	23	24.450

IV.4. Conclusion

Thick, aqueous processed electrodes exhibit drying induced cracks at electrode thicknesses desirable for high energy density LIBs. In an effort to circumvent cracking

and enable aqueous processing for high energy density LIBs, the effect of evaporation rate on crack formation was studied, though very little literature exists which reports any relationship between evaporation rate and cracking in thin films.

LIB cathodes comprised of NMC333, conductive additive, CMC, and PSBR in the weight % ratio 90:5:1:4, respectively, were fabricated at thicknesses of 11, 15, and 23 mg/cm^2, and dried at room temperature (~20 °C), 45 °C, and 70 °C. The mass of each drying electrode sheet was collected at regular intervals to obtain the water content profile from which the evaporation rate could be calculated. It was found that cracking was significantly worse when electrodes were dried at 45 °C and 70 °C. Image analysis carried out on SEM images of each electrode quantitatively confirmed these observations. The crack intensity factor (CIF) of thick electrodes with and areal mass loading of 25 mg/cm^2 increased dramatically from 0.682% at room temperature to 15.1% when dried at 70 °C. Increased crack severity at high drying temperatures can be attributed to the unanticipated formation of holes in the electrodes during the rapid drying process. More experimental investigation is necessary to identify the cause of these holes.

CHAPTER V

CONCLUSION

V.1. Summary

Successful aqueous electrode processing for high energy density LIBs requires an understanding of drying induced cracks, and the processing parameters which influence their formation. In this work, the effect of two parameters on cracking in LIB cathodes was investigated in an attempt to one day enable aqueous electrode processing for high energy density LIBs. The parameters included solvent surface tension and electrode drying temperature. Solvent surface tension is a well-known driving force for drying induced cracking, with high surface tension solvents generating greater stress on a film and consequently leading to more cracks. However, less is known about the influence of evaporation rate on drying induced cracks in thin films such as LIB electrodes.

A composite aqueous solvent of DI water and isoproponal (IPA) was used in LIB cathode fabrication to understand the effect of solvent surface tension on cracking. The addition of IPA to DI water reduced the surface tension of the aqueous solvent. Various weight % compositions of IPA in water were tested, ranging from 0% IPA to 20% IPA. Thick electrodes fabricated with water/IPA composite solvents showed declining crack severity with increasing IPA content. An optical microscope was positioned to capture images of the drying electrodes at regular intervals. From these images, the process of crack nucleation and propagation was observed. It was found that cracks first nucleated at flaws in the coating.

Thick electrodes with a solvent composition of 10% IPA and 20% IPA were fabricated using an industrial slot die coater for the purpose of pouch cell assembly. The electrode fabricated with 10% IPA had minor cracking compared to a similar electrode prepared with only water as solvent. Small cracks in the 10% IPA electrode were later cured by the force of calendering. When coupled with a graphite anode in a single unit pouch cell, the 10% IPA electrode demonstrated satisfactory rate performance and cycle performance,

exhibit significant improvement from a thick electrode processed with only water as solvent. The electrode fabricated with 20% IPA proved even more successful. The electrode was completely crack free before calendering, and was comparable to a thick organically processed electrode in both rate performance and cycle performance. From this work it was concluded that the addition of 20% IPA to water produced an aqueous solvent with a surface tension low enough to avoid all cracking in thick electrodes of interest for high energy density applications.

A similar electrode composition was used to investigate the effect of evaporation rate on crack formation in thick aqueous processed electrodes, though only DI water was used as solvent. However, the hydrophilic binder in this case was different but functionally the same as that used in the solvent surface tension studies. Electrodes of three thicknesses were fabricated – standard thickness, intermediate thickness, and thick electrodes for high energy density LIBs. The electrodes were dried at room temperature (~20 °C), 45 °C, and 70 °C. The evolution of electrode water content was measured by weighing the electrode at regular intervals throughout the drying process. Two drying phases distinctive to drying particulate dispersions could be observed, namely the period of constant evaporation rate followed by an exponential decay in water mass during the period of non-constant evaporation.

From image analysis of SEM images taken of each electrode, it was found that crack length and average crack width increased with increasing drying temperature. Moreover, the crack intensity factory, or area of electrode surface covered in cracks, increased substantially for higher drying temperatures. SEM images of electrodes also revealed the presence of holes in electrodes dried at high temperatures. The number of holes increased with electrode thickness *and* drying temperature. Defects in thin films such as holes promote cracking, and thus holes in electrodes dried at temperatures above ambient were identified as the reason crack severity increased for higher drying temperatures.

Though holes in electrodes are the explanation for more severe cracking at higher drying temperatures, it remains to be determined why the holes are forming at all. Two theories

could explain the presence of holes in these electrodes. First, the electrode composition is not optimal. Targray [119] recommends using 1.5 wt.% PSBR in cathodes for LIBs. The electrode composition used in this study included 4 wt. % PSBR. Hydrophilic polymeric binders used in aqueous electrode processing adsorb to particle surfaces and function not only as a binding material by bridging particles, but also a dispersant. Unlike a surfactant which modifies particle surface chemistry to promote electrostatic repulsion, polymer dispersants introduce a new repulsive interparticle force – steric repulsion. [129] Electrode compositions are often optimized to include only the amount of binder needed to saturate the particle surface, thereby avoiding unwanted free polymer chains in the solvent and maximizing the amount of active material. [54, 118] When polymer chains fail to adsorb to particles they remain dissolved in the solvent, and thus accompany solvent evaporation from the free surface of the electrode and migrate upward. [118, 130] Under normal circumstances, the consequence of free binder migration with evaporating solvent is a non-uniform distribution of binder, with decreasing binder content from the top to bottom surface of the coating resulting in poor adhesion to the current collector. [54, 118] However, hydrophilic polymeric binders for aqueous processing are often in the form of an aqueous emulsion and thus function as an emulsifier (i.e. surfactant) in the cathode slurry. In the event that free emulsifier is present in sufficient amounts, a film of emulsifier can form at the surface of the coating. [130] If 4 wt. % PSBR is indeed excessive so a large amount of free polymer remains in the solvent, PSBR could be forming a film on the surface of the electrode coating that interacts with the physics of the drying process in a way that forms surface bubbles which eventually collapse, leaving holes in the electrode. Thicker electrodes will include more free PSBR per unit area, resulting in a thicker film of PSBR on the surface of the electrode during drying. This could explain why more holes appear as electrode thickness increases. However, it does not explain why more holes can be seen in electrodes dried at increasing temperatures. Rather, the observed temperature dependence on hole formation may be caused by an instability of the PSBR emulsion at high temperatures. Since PSBR acts as a surfactant in the emulsion, thermal instability

could be materialized in the manner of bubble generation within the material. Bubbles then rise to the surface of the electrode coating, forming holes in their wake.

In short, the observation of holes in electrodes dried at temperatures above ambient was entirely unexpected and the mechanism by which they form remains unknown. More experimental research needs to be conducted to elucidate the phenomenon.

V.2. Future Work

Continuing research related to this work is twofold. First, further experimental research is necessary to determine the origin of holes in electrodes dried at higher temperatures. In particular the effect of electrode composition on cracking, and therefore the formation of holes, needs to be investigated. Moreover, studies into the thermal stability of PSBR as an emulsifier in aqueous processed LIB electrodes would contribute to the understanding of hole formation in drying electrodes.

In addition to experimental research, the results presented in this work should be complimented with a computational model of the drying of an aqueous processed electrode, capable of simulating the development of stress inducing capillary pressures and the nucleation of cracks. No such model exists thus far but would be instrumental in the success of thick aqueous processed electrodes for high energy density lithium-ion batteries.

REFERENCES

[1]   (2016). *About EV Everywhere | Department of Energy*. Available: http://energy.gov/eere/eveverywhere/about-ev-everywhere

[2]   D. Howell, "Overview of the DOE Advanced Battery R&D Program," in *Vehicle Technology Office and Hydrogen and Fuel Cells Program Annual Merit Review and Peer Evaluation Meeting about Batteries*, 2014.

[3]   "Vehicle Technologies Office: Batteries | Department of Energy," 2016.

[4]   D. Howell, B. Cunningham, T. Duong, and P. Faguy, "Overview of the DOE VTO Advanced Battery R&D Program," in *Vehicle Technology Office and Hydrogen and Fuel Cells Program Annual Merit Review and Peer Evaluation Meeting about Batteries*, 2016.

[5]   E. J. Cairns and P. Albertus, "Batteries for electric and hybrid-electric vehicles," *Annu Rev Chem Biomol Eng,* vol. 1, pp. 299-320, 2010.

[6]   Y. Nishi, "Lithium ion secondary batteries; past 10 years and the future," *Journal of Power Sources,* vol. 100, pp. 101-106, 2001.

[7]   C. D. Rahn and C.-Y. Wang, *Battery systems engineering*: John Wiley & Sons, 2013.

[8]   M. Winter and R. J. Brodd, "What are batteries, fuel cells, and supercapacitors?," *Chemical Reviews,* vol. 104, pp. 4245-4270, 2004.

[9]   J. W. Fergus, "Recent developments in cathode materials for lithium ion batteries," *Journal of Power Sources,* vol. 195, pp. 939-954, 2010.

[10]   C. Daniel, D. Mohanty, J. Li, and D. L. Wood, "Cathode materials review," in *AIP Conference Proceedings*, 2014, pp. 26-43.

[11]   J. Li, C. Daniel, and D. Wood, "Materials processing for lithium-ion batteries," *Journal of Power Sources,* vol. 196, pp. 2452-2460, 2011.

[12]   B. Xu, D. Qian, Z. Wang, and Y. S. Meng, "Recent progress in cathode materials research for advanced lithium ion batteries," *Materials Science and Engineering: R: Reports,* vol. 73, pp. 51-65, 2012.

[13]   D. Linden, "Factors Affecting Battery Performance," *Handbook of Batteries,* 2001.

[14]   D. L. Wood, J. Li, and C. Daniel, "Prospects for reducing the processing cost of lithium ion batteries," *Journal of Power Sources,* vol. 275, pp. 234-242, 2015.

[15]   C. Fongy, P. Moreau, S. Chazelle, M. Bouvier, S. Jouanneau, D. Guyomard*, et al.*, "Toward the aqueous processing of Li4Ti5O12: A comparative study with LiFePO4," *Journal of the Electrochemical Society,* vol. 159, pp. A1083-A1090, 2012.

[16]   S.-L. Chou, J.-Z. Wang, H.-K. Liu, and S.-X. Dou, "Rapid synthesis of Li4Ti5O12 microspheres as anode materials and its binder effect for lithium-ion battery," *The Journal of Physical Chemistry C,* vol. 115, pp. 16220-16227, 2011.

[17]   J. Lin, Z. Peng, C. Xiang, G. Ruan, Z. Yan, D. Natelson*, et al.*, "Graphene nanoribbon and nanostructured SnO2 composite anodes for lithium ion batteries," *ACS nano,* vol. 7, pp. 6001-6006, 2013.

[18]   B. Li, X. Li, W. Li, Y. Wang, E. Uchaker, Y. Pei*, et al.*, "Mesoporous tungsten trioxide polyaniline nanocomposite as an anode material for high-performance lithium-ion batteries," *ChemNanoMat,* vol. 2, pp. 281-289, 2016.

[19]   Y. Zhao, X. Li, B. Yan, D. Li, S. Lawes, and X. Sun, "Significant impact of 2D graphene nanosheets on large volume change tin-based anodes in lithium-ion batteries: a review," *Journal of Power Sources,* vol. 274, pp. 869-884, 2015.

[20]   M. Obrovac and V. Chevrier, "Alloy negative electrodes for Li-ion batteries," *Chemical reviews,* vol. 114, pp. 11444-11502, 2014.

[21]   Y. Xu, Q. Liu, Y. Zhu, Y. Liu, A. Langrock, M. R. Zachariah*, et al.*, "Uniform nano-Sn/C composite anodes for lithium ion batteries," *Nano letters,* vol. 13, pp. 470-474, 2013.

[22]   Z. Cai, L. Xu, M. Yan, C. Han, L. He, K. M. Hercule*, et al.*, "Manganese oxide/carbon yolk–shell nanorod anodes for high capacity lithium batteries," *Nano letters,* vol. 15, pp. 738-744, 2014.

[23] Z. Du, R. A. Dunlap, and M. N. Obrovac, "High energy density calendered Si alloy/Graphite anodes," *Journal of the Electrochemical Society,* vol. 161, pp. A1698-A1705, 2014.

[24] Y. Chen, M. Xu, Y. Zhang, Y. Pan, B. L. Lucht, and A. Bose, "All-Aqueous Directed Assembly Strategy for Forming High-Capacity, Stable Silicon/Carbon Anodes for Lithium-Ion Batteries," *ACS Applied Materials & Interfaces,* vol. 7, pp. 21391-21397, 2015.

[25] X. Cao, X. Chuan, S. Li, D. Huang, and G. Cao, "Hollow silica spheres embedded in a porous carbon matrix and its superior performance as the anode for lithium-ion batteries," *Particle & Particle Systems Characterization,* 2015.

[26] J. Liu, K. Song, C. Zhu, C.-C. Chen, P. A. van Aken, J. Maier*, et al.*, "Ge/C nanowires as high-capacity and long-life anode materials for Li-ion batteries," *ACS nano,* vol. 8, pp. 7051-7059, 2014.

[27] D. Li, C. Feng, H. kun Liu, and Z. Guo, "Hollow carbon spheres with encapsulated germanium as an anode material for lithium ion batteries," *Journal of Materials Chemistry A,* vol. 3, pp. 978-981, 2015.

[28] N. Liu, Z. Lu, J. Zhao, M. T. McDowell, H.-W. Lee, W. Zhao*, et al.*, "A pomegranate-inspired nanoscale design for large-volume-change lithium battery anodes," *Nature Nanotechnology,* vol. 9, pp. 187-192, 2014.

[29] G. Mulder, N. Omar, S. Pauwels, M. Meeus, F. Leemans, B. Verbrugge*, et al.*, "Comparison of commercial battery cells in relation to material properties," *Electrochimica Acta,* vol. 87, pp. 473-488, 2013.

[30] K. Shaju, G. S. Rao, and B. Chowdari, "Performance of layered Li (Ni 1/3 Co 1/3 Mn 1/3) O 2 as cathode for Li-ion batteries," *Electrochimica Acta,* vol. 48, pp. 145-151, 2002.

[31] M. S. Whittingham, "Lithium batteries and cathode materials," *Chemical Reviews,* vol. 104, pp. 4271-4302, 2004.

[32]   A. K. Padhi, K. Nanjundaswamy, and J. Goodenough, "Phospho-olivines as positive-electrode materials for rechargeable lithium batteries," *Journal of the Electrochemical Society,* vol. 144, pp. 1188-1194, 1997.

[33]   N. Ravet, Y. Chouinard, J. Magnan, S. Besner, M. Gauthier, and M. Armand, "Electroactivity of natural and synthetic triphylite," *Journal of Power Sources,* vol. 97, pp. 503-507, 2001.

[34]   Z. Liu, A. Yu, and J. Y. Lee, "Synthesis and characterization of LiNi 1− x− y Co x Mn y O 2 as the cathode materials of secondary lithium batteries," *Journal of Power Sources,* vol. 81, pp. 416-419, 1999.

[35]   J.-M. Kim and H.-T. Chung, "The first cycle characteristics of Li[Ni1/3Co1/3Mn1/3]O2 charged up to 4.7 V," *Electrochimica Acta,* vol. 49, pp. 937-944, 2004.

[36]   H. Meng, B. Huang, J. Yin, X. Yao, and X. Xu, "Synthesis and electrochemical properties of LiNi1/3Co1/3Mn1/3O2 cathodes in lithium-ion and all-solid-state lithium batteries," *Ionics,* vol. 21, pp. 43-49, 2014.

[37]   T. Ohzuku and Y. Makimura, "Layered lithium insertion material of LiCo1/3Ni1/3Mn1/3O2 for lithium-ion batteries," *Chemistry Letters,* pp. 642-643, 2001.

[38]   I. Belharouak, Y. K. Sun, J. Liu, and K. Amine, "Li(Ni1/3Co1/3Mn1/3)O2 as a suitable cathode for high power applications," *Journal of Power Sources,* vol. 123, pp. 247-252, 2003.

[39]   N. Yabuuchi and T. Ohzuku, "Novel lithium insertion material of LiCo1/3Ni1/3Mn1/3O2 for advanced lithium-ion batteries," *Journal of Power Sources,* vol. 119-121, pp. 171-174, 2003.

[40]   J. Gainese and R. Cuenza, "Costs of Lithium-Ion-Batteries for Vehicles; Argonne National Laboratory: Argonne, IL, 2000," *There is no corresponding record for this reference*.

[41]   B. Nykvist and M. Nilsson, "Rapidly falling costs of battery packs for electric vehicles," *Nature Climate Change,* vol. 5, pp. 329-332, 2015.

[42] F. A. Cetinel and W. Bauer, "Processing of water-based LiNi1/3Mn1/3Co1/3O2 pastes for manufacturing lithium ion battery cathodes," *Bulletin of Materials Science,* vol. 37, pp. 1685-1690, 2014.

[43] C.-C. Li, Y.-H. Wang, and T.-Y. Yang, "Effects of surface-coated carbon on the chemical selectivity for water-soluble dispersants of LiFePO4," *Journal of The Electrochemical Society,* vol. 158, p. A828, 2011.

[44] "NMP (N-Methyl-2-Pyrrolidone) Safety Data Sheet," ed: Eastman Chemical Co., Revised 01-21-2016.

[45] U. Hass, S. P. Lund, and J. Elsner, "Effects of prenatal exposure to N-methylpyrrolidone on postnatal development and behavior in rats," *Neurotoxicology and teratology,* vol. 16, pp. 241-249, 1994.

[46] G. M. Solomon, E. P. Morse, M. J. Garbo, and D. K. Milton, "Stillbirth after occupational exposure to N-methyl-2-pyrrolidone: a case report and review of the literature," *Journal of Occupational and Environmental Medicine,* vol. 38, pp. 705- 713, 1996.

[47] H. Solomon, B. Burgess, G. Kennedy, and R. Staples, "1-Methyl-2-pyrrolidone (NMP): reproductive and developmental toxicity study by inhalation in the rat," *Drug and Chemical Toxicology,* vol. 18, pp. 271-293, 1995.

[48] P. J. Becci, M. J. Knickerbocker, E. L. Reagan, R. A. Parent, and L. W. Burnette, "Teratogenicity study of N-methylpyrrolidone after dermal application to Sprague-Dawley rats," *Toxicological Sciences,* vol. 2, pp. 73-76, 1982.

[49] S. A. Keener, R. Wrbitzky, and M. Bader, "Human volunteer study on the influence of exposure duration and dilution of dermally applied N-methyl-2-pyrrolidone (NMP) on the urinary elimination of NMP metabolites," *International Archives of Occupational and Environmental Health,* vol. 80, pp. 327-334, 2007.

[50] I. Midgley, A. Hood, L. Chasseaud, C. Brindley, S. Baughman, and G. Allan, "Percutaneous absorption of co-administered N-methyl-2-[14C] pyrrolidinone and 2-[14C] pyrrolidinone in the rat," *Food and Chemical Toxicology,* vol. 30, pp. 57- 64, 1992.

[51]   C. Ursin, C. M. Hansen, J. W. Van Dyk, P. O. Jensen, I. J. Christensen, and J. Ebbehoej, "Permeability of commercial solvents through living human skin," *American Industrial Hygiene Association,* vol. 56, pp. 651-660, 1995.

[52]   J. Li, B. L. Armstrong, J. Kiggans, C. Daniel, and D. L. Wood, "Lithium ion cell performance enhancement using aqueous LiFePO4 cathode dispersions and polyethyleneimine dispersant," *Journal of the Electrochemical Society,* vol. 160, pp. A201-A206, 2012.

[53]   M. Zackrisson, L. Avellán, and J. Orlenius, "Life cycle assessment of lithium-ion batteries for plug-in hybrid electric vehicles – Critical issues," *Journal of Cleaner Production,* vol. 18, pp. 1519-1529, 2010.

[54]   W. Porcher, B. Lestriez, S. Jouanneau, and D. Guyomard, "Design of aqueous processed thick LiFePO[sub 4] composite electrodes for high-energy lithium battery," *Journal of The Electrochemical Society,* vol. 156, p. A133, 2009.

[55]   Q. Wu, S. Ha, J. Prakash, D. W. Dees, and W. Lu, "Investigations on high energy lithium-ion batteries with aqueous binder," *Electrochimica Acta,* vol. 114, pp. 1-6, 2013.

[56]   H. Zhong, M. Sun, Y. Li, J. He, J. Yang, and L. Zhang, "The polyacrylic latex: an efficient water-soluble binder for LiNi1/3Co1/3Mn1/3O2 cathode in li-ion batteries," *Journal of Solid State Electrochemistry,* vol. 20, pp. 1-8, 2016.

[57]   N. Loeffler, J. von Zamory, N. Laszczynski, I. Doberdo, G.-T. Kim, and S. Passerini, "Performance of LiNi1/3Mn1/3Co1/3O2/graphite batteries based on aqueous binder," *Journal of Power Sources,* vol. 248, pp. 915-922, 2014.

[58]   J. Li, B. L. Armstrong, C. Daniel, J. Kiggans, and D. L. Wood, 3rd, "Optimization of multicomponent aqueous suspensions of lithium iron phosphate (LiFePO4) nanoparticles and carbon black for lithium-ion battery cathodes," *J Colloid Interface Sci,* vol. 405, pp. 118-24, Sep 1 2013.

[59]   J. Li, B. L. Armstrong, J. Kiggans, C. Daniel, and D. L. Wood, 3rd, "Optimization of LiFePO4 nanoparticle suspensions with polyethyleneimine for aqueous processing," *Langmuir,* vol. 28, pp. 3783-90, Feb 28 2012.

[60]   J. Li, C. Rulison, J. Kiggans, C. Daniel, and D. L. Wood, "Superior performance of LiFePO4 aqueous dispersions via Corona Treatment and surface energy optimization," *Journal of the Electrochemical Society,* vol. 159, pp. A1152-A1157, 2012.

[61]   A. Guerfi, M. Kaneko, M. Petitclerc, M. Mori, and K. Zaghib, "LiFePO4 water-soluble binder electrode for Li-ion batteries," *Journal of Power Sources,* vol. 163, pp. 1047-1052, 2007.

[62]   G. T. Kim, S. S. Jeong, M. Joost, E. Rocca, M. Winter, S. Passerini*, et al.*, "Use of natural binders and ionic liquid electrolytes for greener and safer lithium-ion batteries," *Journal of Power Sources,* vol. 196, pp. 2187-2194, 2011.

[63]   S. Lux, F. Schappacher, A. Balducci, S. Passerini, and M. Winter, "Low cost, environmentally benign binders for lithium-ion batteries," *Journal of the Electrochemical Society,* vol. 157, pp. A320-A325, 2010.

[64]   J. Chong, S. Xun, H. Zheng, X. Song, G. Liu, P. Ridgway*, et al.*, "A comparative study of polyacrylic acid and poly (vinylidene difluoride) binders for spherical natural graphite/LiFePO 4 electrodes and cells," *Journal of Power Sources,* vol. 196, pp. 7707-7714, 2011.

[65]   S. Komaba, K. Okushi, T. Ozeki, H. Yui, Y. Katayama, T. Miura*, et al.*, "Polyacrylate modifier for graphite anode of lithium-ion batteries," *Electrochemical and Solid-State Letters,* vol. 12, pp. A107-A110, 2009.

[66]   J. Li, D.-B. Le, P. Ferguson, and J. Dahn, "Lithium polyacrylate as a binder for tin–cobalt–carbon negative electrodes in lithium-ion batteries," *Electrochimica Acta,* vol. 55, pp. 2991-2995, 2010.

[67]   E. Pohjalainen, S. Räsänen, M. Jokinen, K. Yliniemi, D. A. Worsley, J. Kuusivaara*, et al.*, "Water soluble binder for fabrication of Li4Ti5O12 electrodes," *Journal of Power Sources,* vol. 226, pp. 134-139, 2013.

[68]   J. Xu, S.-L. Chou, Q.-f. Gu, H.-K. Liu, and S.-X. Dou, "The effect of different binders on electrochemical properties of LiNi1/3Mn1/3Co1/3O2 cathode material in lithium ion batteries," *Journal of Power Sources,* vol. 225, pp. 172-178, 2013.

[69] J. Li, R. Klöpsch, S. Nowak, M. Kunze, M. Winter, and S. Passerini, "Investigations on cellulose-based high voltage composite cathodes for lithium ion batteries," *Journal of Power Sources,* vol. 196, pp. 7687-7691, 2011.

[70] M. He, L.-X. Yuan, W.-X. Zhang, X.-L. Hu, and Y.-H. Huang, "Enhanced cyclability for sulfur cathode achieved by a water-soluble binder," *The Journal of Physical Chemistry C,* vol. 115, pp. 15703-15709, 2011.

[71] J.-H. Lee, U. Paik, V. A. Hackley, and Y.-M. Choi, "Effect of carboxymethyl cellulose on aqueous processing of natural graphite negative electrodes and their electrochemical performance for lithium batteries," *Journal of The Electrochemical Society,* vol. 152, pp. A1763-A1769, 2005.

[72] M. H. Lee, Y. J. Kang, S. T. Myung, and Y. K. Sun, "Synthetic optimization of Li[Ni1/3Co1/3Mn1/3]O2 via co-precipitation," *Electrochimica Acta,* vol. 50, pp. 939-948, 2004.

[73] A. Moretti, G.-T. Kim, D. Bresser, K. Renger, E. Paillard, R. Marassi*, et al.*, "Investigation of different binding agents for nanocrystalline anatase TiO2 anodes and its application in a novel, green lithium-ion battery," *Journal of Power Sources,* vol. 221, pp. 419-426, 2013.

[74] J. Jung, J. Jang, O. B. Chae, T. Yoon, J. H. Ryu, and S. M. Oh, "Reinforcement of an electrically conductive network with ethanol as a dispersing agent in the slurry preparation step," *Journal of Power Sources,* vol. 287, pp. 359-362, 2015.

[75] W. Porcher, B. Lestriez, S. Jouanneau, and D. Guyomard, "Optimizing the surfactant for the aqueous processing of LiFePO4 composite electrodes," *Journal of Power Sources,* vol. 195, pp. 2835-2843, 2010.

[76] H. Zheng, J. Li, X. Song, G. Liu, and V. S. Battaglia, "A comprehensive understanding of electrode thickness effects on the electrochemical performances of Li-ion battery cathodes," *Electrochimica Acta,* vol. 71, pp. 258-265, 2012.

[77] K. G. Gallagher, S. E. Trask, C. Bauer, T. Woehrle, S. F. Lux, M. Tschech*, et al.*, "Optimizing areal capacities through understanding the limitations of lithium-ion

electrodes," *Journal of The Electrochemical Society,* vol. 163, pp. A138-A149, 2016.

[78] H. Zheng, G. Liu, X. Song, P. Ridgway, S. Xun, and V. S. Battaglia, "Cathode performance as a function of inactive material and void fractions," *Journal of The Electrochemical Society,* vol. 157, pp. A1060-A1066, 2010.

[79] Y.-H. Chen, C.-W. Wang, X. Zhang, and A. M. Sastry, "Porous cathode optimization for lithium cells: Ionic and electronic conductivity, capacity, and selection of materials," *Journal of Power Sources,* vol. 195, pp. 2851-2862, 2010.

[80] G. Liu, H. Zheng, A. Simens, A. Minor, X. Song, and V. Battaglia, "Optimization of acetylene black conductive additive and PVDF composition for high-power rechargeable lithium-ion cells," *Journal of The Electrochemical Society,* vol. 154, pp. A1129-A1134, 2007.

[81] G. Liu, H. Zheng, S. Kim, Y. Deng, A. Minor, X. Song, *et al.*, "Effects of various conductive additive and polymeric binder contents on the performance of a lithium-ion composite cathode," *Journal of The Electrochemical Society,* vol. 155, pp. A887-A892, 2008.

[82] M. Singh, J. Kaiser, and H. Hahn, "Thick electrodes for high energy lithium ion batteries," *Journal of The Electrochemical Society,* vol. 162, pp. A1196-A1201, 2015.

[83] W. Lu, A. Jansen, D. Dees, P. Nelson, N. R. Veselka, and G. Henriksen, "High-energy electrode investigation for plug-in hybrid electric vehicles," *Journal of Power Sources,* vol. 196, pp. 1537-1540, 2011.

[84] Z. Du, K.M. Rollag, et al., "Enabling aqueous processing for high-energy-density Li-ion batteries, I. Challenges of aqueous processing for thick electrodes " *Submitted for Publication,* 2017.

[85] C. de Sa, F. Benboudjema, M. Thiery, and J. Sicard, "Analysis of microcracking induced by differential drying shrinkage," *Cement and Concrete Composites,* vol. 30, pp. 947-956, 2008.

[86] P. Lura, B. Pease, G. B. Mazzotta, F. Rajabipour, and J. Weiss, "Influence of shrinkage-reducing admixtures on development of plastic shrinkage cracks," *ACI Materials Journal,* vol. 104, p. 187, 2007.

[87] S. Kitsunezaki, "Fracture patterns induced by desiccation in a thin layer," *Physical Review E,* vol. 60, p. 6449, 1999.

[88] P. D. Hallett and T. A. Newson, "Describing soil crack formation using elastic-plastic fracture mechanics," *European Journal of Soil Science,* vol. 56, pp. 31-38, 2005.

[89] R. C. Chiu and M. J. Cima, "Drying of granular ceramic films: II, drying stress and saturation uniformity," *Journal of the American Ceramic Society,* vol. 76, pp. 2769-2777, 1993.

[90] R. C. Chiu, T. Garino, and M. Cima, "Drying of granular ceramic films: I, effect of processing variables on cracking behavior," *Journal of the American Ceramic Society,* vol. 76, pp. 2257-2264, 1993.

[91] A. F. Routh, "Drying of thin colloidal films," *Rep Prog Phys,* vol. 76, p. 046603, Apr 2013.

[92] R. Sengupta and M. S. Tirumkudulu, "Dynamics of cracking in drying colloidal sheets," *Soft Matter,* vol. 12, pp. 3149-55, Apr 7 2016.

[93] K. B. Singh, G. Deoghare, and M. S. Tirumkudulu, "Cracking in Soft− Hard Latex Blends: Theory and Experiments," *Langmuir,* vol. 25, pp. 751-760, 2008.

[94] M. S. Tirumkudulu and W. B. Russel, "Cracking in drying latex films," *Langmuir,* vol. 21, pp. 4938-4948, 2005.

[95] M. S. Tirumkudulu and W. B. Russel, "Role of capillary stresses in film formation," *Langmuir,* vol. 20, pp. 2947-2961, 2004.

[96] A. F. Routh and W. B. Russel, "Horizontal drying fronts during solvent evaporation from latex films," *AIChE Journal,* vol. 44, pp. 2088-2098, 1998.

[97] A. F. Routh and W. B. Russel, "A process model for latex film formation: limiting regimes for individual driving forces," *Langmuir,* vol. 15, pp. 7762-7773, 1999.

[98]   S. Lim, S. Kim, K. H. Ahn, and S. J. Lee, "Stress development of Li-Ion battery anode slurries during the drying process," *Industrial & Engineering Chemistry Research,* vol. 54, pp. 6146-6155, 2015.

[99]   P. Xu, A. S. Mujumdar, and B. Yu, "Drying-induced cracks in thin film fabricated from colloidal dispersions," *Drying Technology,* vol. 27, pp. 636-652, 2009.

[100]   A. A. Griffith, "The phenomena of rupture and flow in solids," *Philosophical transactions of the royal society of london. Series A, containing papers of a mathematical or physical character,* vol. 221, pp. 163-198, 1921.

[101]   K. B. Singh and M. S. Tirumkudulu, "Cracking in drying colloidal films," *Phys Rev Lett,* vol. 98, p. 218302, May 25 2007.

[102]   V. Slowik, M. Schmidt, and R. Fritzsch, "Capillary pressure in fresh cement-based materials and identification of the air entry value," *Cement and Concrete Composites,* vol. 30, pp. 557-565, 2008.

[103]   L. Goehring, W. J. Clegg, and A. F. Routh, "Plasticity and fracture in drying colloidal films," *Phys Rev Lett,* vol. 110, p. 024301, Jan 11 2013.

[104]   P. C. Kapur, P. J. Scales, D. V. Boger, and T. W. Healy, "Yield stress of suspensions loaded with size distributed particles," *AIChE Journal,* vol. 43, pp. 1171-1179, 1997.

[105]   V. Slowik, T. Hübner, M. Schmidt, and B. Villmann, "Simulation of capillary shrinkage cracking in cement-like materials," *Cement and Concrete Composites,* vol. 31, pp. 461-469, 2009.

[106]   H. Shin and J. C. Santamarina, "Desiccation cracks in saturated fine-grained soils: particle-level phenomena and effective-stress analysis," *Géotechnique,* vol. 61, pp. 961-972, 2011.

[107]   G. Vazquez, E. Alvarez, and J. M. Navaza, "Surface tension of alcohol water+ water from 20 to 50. degree. C," *Journal of Chemical and Engineering Data,* vol. 40, pp. 611-614, 1995.

[108] H. Ghahremani, A. Moradi, J. Abedini-Torghabeh, and S. Hassani, "Measuring surface tension of binary mixtures of water+ alcohols from the diffraction pattern of surface ripples," *Der Chem. Sin.,* vol. 2, pp. 212-221, 2012.

[109] K. A. Connors and J. L. Wright, "Dependence of surface tension on composition of binary aqueous-organic solutions," *Analytical Chemistry,* vol. 61, pp. 194-198, 1989.

[110] W. Man and W. B. Russel, "Direct measurements of critical stresses and cracking in thin films of colloid dispersions," *Physical Review Letters,* vol. 100, 2008.

[111] A. F. Routh and W. B. Zimmerman, "Distribution of particles during solvent evaporation from films," *Chemical Engineering Science,* vol. 59, pp. 2961-2968, 2004.

[112] R. E. Trueman, E. Lago Domingues, S. N. Emmett, M. W. Murray, J. L. Keddie, and A. F. Routh, "Autostratification in drying colloidal dispersions: experimental investigations," *Langmuir,* vol. 28, pp. 3420-8, Feb 21 2012.

[113] R. E. Trueman, E. Lago Domingues, S. N. Emmett, M. W. Murray, and A. F. Routh, "Auto-stratification in drying colloidal dispersions: a diffusive model," *J Colloid Interface Sci,* vol. 377, pp. 207-12, Jul 1 2012.

[114] C. M. Cardinal, Y. D. Jung, K. H. Ahn, and L. F. Francis, "Drying regime maps for particulate coatings," *AIChE Journal,* vol. 56, pp. 2769-2780, 2010.

[115] A.-C. Grillet, S. Brunel, Y. Chevalier, S. Usoni, V. Ansanay-Alex, and J. Allemand, "Control of the morphology of waterborne nanocomposite films," *Polymer International,* vol. 53, pp. 569-575, 2004.

[116] W. P. Lee and A. F. Routh, "Why do drying films crack?," *Langmuir,* vol. 20, pp. 9885-9888, 2004.

[117] J.-H. Lee, S. Lee, U. Paik, and Y.-M. Choi, "Aqueous processing of natural graphite particulates for lithium-ion battery anodes and their electrochemical performance," *Journal of Power Sources,* vol. 147, pp. 249-255, 2005.

[118] C.-C. Li and Y.-W. Wang, "Importance of binder compositions to the dispersion and electrochemical properties of water-based LiCoO2 cathodes," *Journal of Power Sources,* vol. 227, pp. 204-210, 2013.

[119] "Modified Styrene-Butadiene Copolymer Product Data Sheet," ed: Targray, 2012.

[120] Z. Wang, R. Winslow, D. Madan, P. K. Wright, J. W. Evans, M. Keif, *et al.*, "Development of MnO2 cathode inks for flexographically printed rechargeable zinc-based battery," *Journal of Power Sources,* vol. 268, pp. 246-254, 2014.

[121] M. J. Lacey, A. Yalamanchili, J. Maibach, C. Tengstedt, K. Edström, and D. Brandell, "The Li–S battery: an investigation of redox shuttle and self-discharge behaviour with LiNO 3-containing electrolytes," *RSC Advances,* vol. 6, pp. 3632-3641, 2016.

[122] Y. Khan, M. Garg, Q. Gui, M. Schadt, A. Gaikwad, D. Han, *et al.*, "Flexible Hybrid Electronics: Direct interfacing of soft and hard electronics for wearable health Monitoring," *Advanced Functional Materials,* vol. 26, pp. 8764-8775, 2016.

[123] A. E. Ostfeld, A. M. Gaikwad, Y. Khan, and A. C. Arias, "High-performance flexible energy storage and harvesting system for wearable electronics," *Scientific Reports,* vol. 6, 2016.

[124] R. Auvray, S. Rosin-Paumier, A. Abdallah, and F. Masrouri, "Quantification of soft soil cracking during suction cycles by image processing," *European Journal of Environmental and Civil Engineering,* vol. 18, pp. 11-32, 2013.

[125] C. J. Miller, H. Mi, and N. Yesiller, "Experimental analysis of desiccation crack propagation in clay liners," ed: Wiley Online Library, 1998.

[126] A. Atique and M. Sanchez, "Analysis of cracking behavior of drying soil," in *2nd International Conference on Environmental Science and Technology IPCBEE, Singapore*, 2011.

[127] I. Analyst, "Thresholding an Image," ed. MathWorks File Exchange, 2015.

[128] Z. Du, K.M. Rollag, et al., "Enabling aqueous processing for high-energy-density Li-ion batteries, II. Processing solutions for thick, aqueous crack-free lithium-ion electrodes," *Submitted for Publication,* 2017.

[129] R. Flatt, "Towards a prediction of superplasticized concrete rheology," *Materials and Structures,* vol. 37, pp. 289-300, 2004.

[130] A. D. Chesne, B. Gerharz, and G. Lieser, "The segregation of surfactant upon film formation of latex dispersions: an investigation by energy filtering transmission electron microscopy," *Polymer International,* vol. 43, pp. 187-196, 1997.